Effects of Crystalline Anisotropy on Solid-state Dewetting

by

Maxwell A. L'Etoile

A.B., Physics, Harvard University, 2017

Submitted to the Department of Materials Science and Engineering
in partial fulfillment of the requirements for the degree of

Doctor of Philosophy

at the

MASSACHUSETTS INSTITUTE OF TECHNOLOGY

May 2022

Author . . . .
Department of Materials Science and Engineering
April 27, 2022

Certified by. . . . .
Carl V. Thompson
Stavros Salapatas Professor of Materials Science and Engineering
Thesis Supervisor

Certified by. . . . .
W. Craig Carter
Stavros V. and Matoula S. Salapatas Professor of Materials Science
Thesis Supervisor

Accepted by . . . .
Frances M. Ross
Ellen Swallow Richards Professor in Materials Science and Engineering
Chair, Department Committee on Graduate Studies

Effects of Crystalline Anisotropy on Solid-state Dewetting

by

Maxwell A. L'Etoile

Submitted to the Department of Materials Science and Engineering
on April 27, 2022, in partial fulfillment of the
requirements for the degree of
Doctor of Philosophy

Abstract

Solid-state dewetting is the process by which micro– and nano–scale films, wires, and other fabricated structures on a substrate evolve toward geometries which reduce the overall surface free energy of the system. This process, also sometimes referred to as agglomeration, occurs at elevated temperatures and is mediated by surface self-diffusion. Regardless of initial conditions, dewetting eventually leads to the formation of one or more particles whose morphology is determined by the orientational dependence of the constituent material's surface free energy density.

Subtle differences in initial conditions can determine whether a system dewets into a single particle or many and whether this evolution occurs over the course of minutes, hours, days, or years. Furthermore, the intermediate stages of dewetting behavior can exhibit profound complexity, and many materials systems are prone to a host of morphological instabilities. Although decades of research have steadily increased the extent of our knowledge about solid-state dewetting, a generalizable, predictive understanding of dewetting behavior has remained elusive, in large part because of the difficulty of modeling systems with strong crystalline anisotropy.

The work in this thesis focuses on advancing our understanding of the dewetting behavior of single-crystal materials and consists chiefly of two parallel thrusts: the development of a powerful new method for simulating solid-state dewetting and the use of lithographic patterning to experimentally study dewetting in systems with precisely controlled geometries. We apply these two synergistic approaches to understanding the morphological stability of ruthenium nanowires, the effects of ambient conditions on dewetting nickel (110) films, and the dendritic morphologies which arise at the corners of holes in dewetting films.

Thesis Supervisor: Carl V. Thompson
Title: Stavros Salapatas Professor of Materials Science and Engineering

Thesis Supervisor: W. Craig Carter
Title: Stavros V. and Matoula S. Salapatas Professor of Materials Science

Acknowledgments

The completion of this thesis marks the culmination of an incredible period of my life. Since packing a few duffel bags and moving to Cambridge in 2013, I've gained caring and knowledgeable mentors, made the strongest and most meaningful friendships of my life, and met the woman I will soon marry. I've studied physics, math, engineering, history, literature, and more under the instruction and guidance of truly brilliant thinkers and scholars. I've been exposed to new ideas, new cultures, and new approaches to gaining understanding about our world. Though they were not always easy, I will always be grateful for the nine years I spent living along Massachusetts Avenue, the people I met during this time, and those that helped me get here.

To start, I must express my sincere gratitude to my advisors, Carl and Craig. Carl's enthusiasm for his work is infectious, and his dedication to producing quality science in an environment that often rewards bold claims over scrupulousness is truly admirable. He has a vast wealth of materials science knowledge and seems to know the details of every experiment conducted in every field with even slightly overlaps his own. His expectations are high but fair, and I have become a better scientist and more critical thinker in striving to meet them. He has been consistently supportive of both my research and my life outside of it, and his guidance will shape my thinking and writing for the rest of my career. Craig's curiosity-driven approach to science, blending theory and computation to reduce complex problems into their most tractable form, was a joy to learn and take part in. He always seemed to know which textbook, paper, or concept held they key to unlocking our next insight, and he wasn't afraid to point me in the right direction and let me struggle for a while. I once asked Craig which classes I should take to improve my computational and theoretical skills, and he replied that I should take whatever sounded most fun. Insights often arise from ideas that initially seem playful, and I am still unpacking the full wisdom of this advice. His trust in my abilities helped me to develop my own skills and confidence.

I also want to thank Profs. Caroline Ross, Frances Ross, and Antoine Allanore

for their help and guidance during this process. Caroline and Frances provided ample support as members of my committee, and their genuine interest in my research was fantastic encouragement. I am especially grateful to Frances for the opportunities she gave me to present to her research group and undergraduate class and for the help she provided with my post-graduation job hunt. Antoine helped me learn to take ownership of my research through a few conversations that I had with him early in my PhD process, and I am tremendously grateful for the time and advice he gave me.

I am also immensely grateful to Cécile Chazot and Jessica Sandland for co-founding and operating the MICRO program with me, and I'm tremendously proud of what we accomplished. Jessica is one of the kindest, most patient people I've ever worked with, and I doubt I would have tried to push MICRO from idea to reality if I hadn't known her. Her dedication to the program and deep expertise in online learning were and will continue to be critical drivers of the program's success. Cecile was a truly tireless force for progress with a relentlessly sunny demeanor. She deserves all the success she has achieved, and I wish her the best at Northwestern. I'll be keeping an eye out for her future accomplishments.

The pursuit of a PhD requires long stretches of time spent working alone, and I will always be grateful to the friends I made at MIT for brightening all the other hours. The members of the aspirationally named "gainzzz" chat deserve a special shout-out for being perhaps the most scientifically-accomplished collective to ever choose a bicep emoji as their standard. In particular I owe thanks to Elad and Sachin for being excellent pandemic roommates, Parker for helping me shamelessly copy all of his well-researched technology purchases, George for making several extremely helpful research suggestions, Jackie for being a steadfastly loyal friend and working outside with me when social distancing was chewing away at my sanity, Philipp for sharing my love of artful whinging and for not getting that upset when I convinced many of his friends to start calling him Grandpapa after his thirtieth birthday, Kate for sharing my interest in topics that are "a bit niche", Jasper for lending me his guest bed when my apartment suffered a catastrophic plumbing failure, and Katherine for so memorably getting hit TWICE in the batting cages at Northwestern's visiting

weekend and nucleating the friendship among those of us who decided to come to MIT (she's also an amazing friend who's done countless thoughtful things for me, but this story is funnier). Aside from these specific contributions, I am most grateful to these wonderful people for simply being being themselves and allowing me to be in the vicinity.

I also need to thank my labmates Yoon Ah, Baoming, Lin, and Misong for being a fantastic group of people to do science with. Yoon Ah was an excellent mentor when I was starting in the group, and Baoming's FIB and TEM skills are truly legendary among those that have worked with him. Lars, our building's safety guru, consistently kept us from harming ourselves, and provided far more help than he was required to. Andrew, Kadir, Katy, Kevin, and Quintin were fantastic collaborators on the Ru nanowire project.

My research career began as an undergraduate, and I am immensely grateful to Profs. Frans Spaepen and Shmuel Rubinstein for their support during this time. Frans is the reason I took up materials science, and ES-190, under his instruction, was the most challenging and rewarding class I've ever taken. His generosity in giving me my own research project as an undergraduate, with full support to build experimental apparatuses, rig electronics I'd built to microscopes that cost as much as houses, and take up group meeting time with my findings and difficulties constitutes one of the most impactful gifts anyone has ever given me. Shmuel welcomed me into his group meetings and provided a critical eye for my grad school applications. Zsolt Terdik, the graduate student who supervised my research, went far above and beyond what was required of him, integrating me into a community of scientists and engineers from whom I tried to absorb as much knowledge as possible. I learned more from afternoon coffee breaks with them than I did from most of my classes. Additionally, anyone who finds my penchant for fancy coffee a tad ridiculous can blame Zsolt for sending me down that rabbit hole.

I'd also like to thank the 2016-2017 residents of 20A Prescott—those on the first and second floors for being a truly incredible group of people whom I am honored to call my friends, those on the third and fourth floors for being excellent IM crew

boatmates and for actually keeping the noise down when asked (the true measure of an upstairs neighbor), and the lone resident of the fifth floor, Gregg Peeples, for being an incredible resident dean and friend. The joyful chaos Alex, Ajay, Aman, Curren, Dhruv, and Kait injected into my life is difficult to capture in words, and I still can't believe I had the opportunity to spend four years arguing over almost every meal with these supremely talented fools. Another Prescott alum, Katherine Phillips, made a direct contribution to this thesis work by suggesting that I try using carbon monoxide as a reducing gas. Defying labels as usual, Eesha and Kausalya also deserve thanks for being fantastic undergraduate friends who took the PhD plunge in Cambridge and brightened two degrees worth of days.

Of course, of all the people I met during college, I am most grateful for Christine, my soon-to-be wife. Her kindness, patience, and unwavering support are responsible for so much of the growth I've experienced over the last nine years. As a medical student during a global pandemic, she could still find the capacity, after a day of witnessing illness and death, to ask me about my comparably insignificant struggles with photolithography and parallel computing. Being separated from her for five years was by far the hardest part of grad school, and I cannot wait to spend the rest of my life with her. I am also exceptionally grateful to Christine's family for taking me in while MIT's campus was closed. I am beyond fortunate to have spent four wonderful months with them when so many others were suffering.

From my time before Cambridge, I owe special thanks to Pete Hawkins, Jim Moehl, Reno Holler, Christie McCormick, Pete Horsch, and Greg Ketner, six teachers without whom my life trajectory would likely be much different. Pete Hawkins' one-man physics program produced more scientists and engineers than a random high school in the middle of Oregon has any right to, and his continued friendship has been a true blessing.

I truly cannot thank my mother, Tracy, enough for all the love, guidance, time, support, and understanding she has given me. My strengths have been shaped and cultivated by her, and I'm certain that my weaknesses persist only insofar as I have failed to grasp her teachings. Her joyous approach to life is inspiring, and I can only

aspire to match her kindness, work-ethic, and efficiency. Through a chaotic military childhood, characterized by cross-country moves and long deployments, she provided stability, normalcy, and a sense of home. I know it wasn't easy, and I certainly didn't appreciate it enough at the time, so I'm taking this opportunity and every subsequent one to express my profound gratitude.

My sister, Megan, has been by my side for nearly as long as I can remember, and she still calls me almost every day on her way home from work (I'm really sorry I don't always pick up, and I plan on sending a lot fewer "sorry, in lab" texts from now on). Her passion for all things artistic has broadened my horizons, and her masterful taunts and insults—usually deserved, always creative—have kept my ego at least somewhat in check. I treasure her loyalty, support, and humor, and I'm ecstatic that we no longer have to be 3,000 miles apart.

My father, Joe, has been a constant example of what is possible through the application of grit, confidence, and consistency. Growing up around the physically imposing Marine officer who ran ultra–marathons, read poetry, and joyfully conversed with our otherwise reserved neighbors in their native Spanish taught me that there is tremendous value in confounding the one-dimensional expectations that others place on you. His unwavering belief in me and support of my endeavors have been instrumental in shaping me as a person. He has always cared more about how I handle failure than the degree of my success, and his perspective has helped me to be grateful for the amazing life I've been blessed with.

Terminology

1. WMC: Weighted mean curvature, also denoted as κ^γ. The anisotropic analog of curvature, see chapter 1.2.1 (pg. 30).

2. LSM: Level-set Method(s). An Eularian approach (meaning the surface is tracked implicitly rather than parameterized explicitly) which models the evolution of a surface by tracking the distance from that surface to other points in space. See chapter 2 for a detailed discussion.

3. (HR)SEM: (High Resolution) Scanning Electron Microscopy. A relatively non-destructive characterization tool with resolutions up to nanometer scale. See chapter 1.9.1 (pg. 47).

4. TEM: Transmission Electron Microscopy. An extremely high resolution characterization technique with more constraints and sample-prep requirements than SEM. See chapter 1.9.2 (pg. 47).

5. FIB: Focused Ion Beam. A type of microscopy which is often used in sample preparation and small-batch micro-/nano-fabrication. See chapter 1.9.3 (pg. 48).

6. AFM: Atomic Force Microscopy. A physical characterization technique in which a vertically oscillating probe is scanned across the surface of a sample to provide nanometer-scale resolution of surface topography. See chapter 1.10 (pg. 49).

7. (Microscopic) Solvability: An idea originally developed through the study of solidification. It posits that the steady–state morphologies of dendrite tips

are stable attractors in configuration space. Crystalline anisotropy can endow systems with solvability. See chapter 5 for a detailed discussion and relevant references.

Contents

List of Figures

List of Tables

Supplemental Materials

Videos Accompanying Chapter 2

1. hole_1.mp4 : Simulated growth of an initially circular hole in an Ni (100) film with assumed isotropic surface self–diffusivity. See figure 2-10.

2. hole_2.mp4 : Simulated growth of an initially circular hole in an Ni (100) film with anisotropic surface self–diffusivity. See figure 2-11.

3. hole_3.mp4 : Simulated growth of an initially circular hole in a film with isotropic surface energy but anisotropic surface self–diffusivity. See figure 2-12.

Videos Accompanying Chapter 4

1. wire_0_degree.mp4 : Simulated annealing of a Ru nanowire aligned along the stable $< 11\bar{2}0 >$ direction. See figure 4-7 a).

2. wire_5_degree.mp4 : Simulated annealing of a Ru nanowire offset from $< 11\bar{2}0 >$ by 5° . See figure 4-9.

3. wire_10_degree.mp4 : Simulated annealing of a Ru nanowire offset from $< 11\bar{2}0 >$ by 10° . See figure 4-10.

4. wire_20_degree.mp4 : Simulated annealing of a Ru nanowire offset from $< 11\bar{2}0 >$ by 20° . See figure 4-11.

5. wire_30_degree.mp4 : Simulated annealing of a Ru nanowire offset from $<11\bar{2}0>$ by $30°$. See figure 4-7 b).

Chapter 1

Introduction

Thin crystalline films, and the micro-and-nano-devices which are patterned from them, are crucial to our modern world. At such length scales measured in nanometers, surface area to volume ratios are immense, and surface free energy can be a dominant component of the overall free energy of micro-and-nano-scale systems. As manufactured, most of these devices are far from surface free energy minimizing geometries and thus experience large driving forces for morphological evolution. At normal operating temperatures, however, such evolution is sufficiently slow as to be insignificant. In contrast, at elevated temperatures, the diffusion of surface atoms in many metals and semiconductors becomes sufficiently rapid to allow for significant morphological change over the course of minutes or hours. This diffusive flow of surface atoms from areas of higher surface free energy density to areas of lower surface free energy density can give rise to shockingly complex behaviors and morphologies. Collectively, these behaviors are known as solid-state dewetting, in reference to the fact that, for most systems, such morphological evolution entails decreasing contact, or wetting, between the film and the substrate.

There is a large body of work exploring, cataloging, and modeling these behaviors in different materials systems, motivated by three primary goals: improving our understanding of basic materials physics, learning how to design more resilient nanostructures, and designing self-assembly nano-scale patterning techniques to achieve
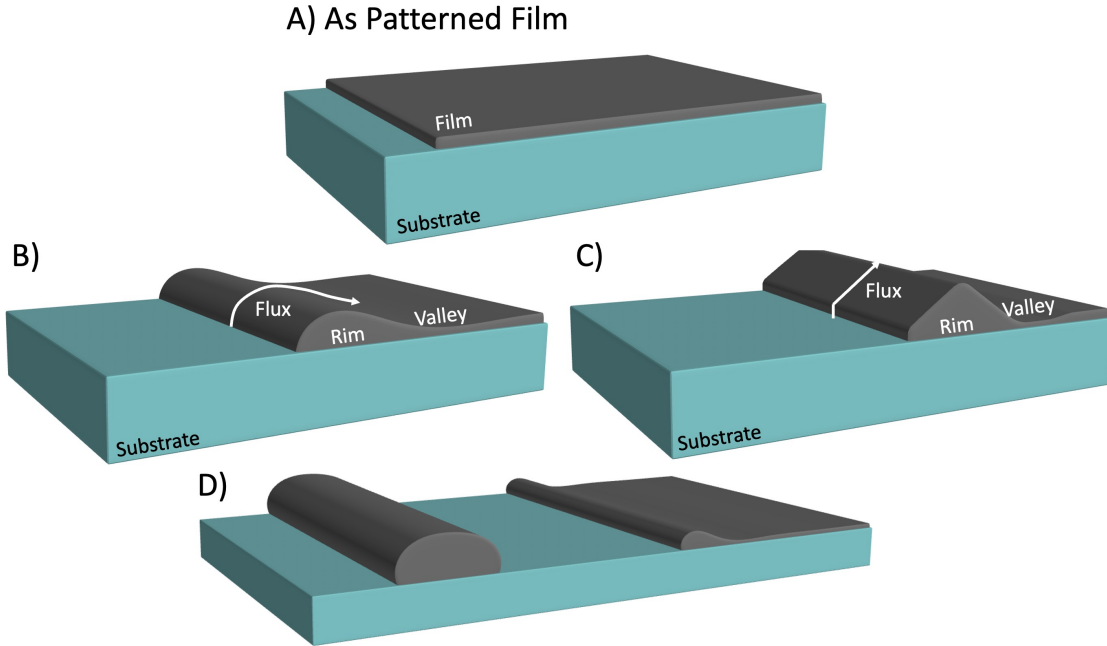
Figure 1-1: An illustration of edge retraction, the simplest dewetting phenomenon. A) shows a section of a semi-infinite film with a straight edge, prior to dewetting. B) shows a later stage for a film with isotropic materials properties (see section 1.1 for a discussion of (an)isotropy), while C) shows the intermediate morphology for a model crystalline film. D) shows the isotropic film from B) after pinch-off has occurred and edge retraction has started again, see section 1.7.1

sub-lithographic resolution. Much past work has focused on polycrystalline films (see Refs. [1, 2], for example) because they are cheaper and easier to manufacture, but the high degree of randomness introduced by grain boundaries means that the degree of control which can be exerted over such systems is relatively low. By contrast, the behavior exhibited in single-crystal systems has been shown to be extremely reproducible [3, 4], suggesting that a predictive understanding of such systems is possible. The most advanced studies of dewetting phenomena have made use of lithographic patterning of single-crystal films to instantiate specific initial morphologies carefully designed to probe specific dewetting behaviors [5–8]. Phenomenological models and heuristics derived from these experiments have demonstrated a great deal of explanatory value and can be predictive within the confines of the experimental regimes for which they were developed. Likewise, computational models, numerical analyses, and simulations have provided a great deal of qualitative insight into dewetting behaviors,

but none of these techniques have demonstrated significant predictive power across a wide range of materials systems and phenomena. From the outset, the goal of this thesis work was to advance the state of our understanding of dewetting phenomena from explanatory to predictive and to study interesting new phenomena along the way. This thesis aims to present the fruits of those labors as cleanly and accessibly as possible, and the rest of this introduction is dedicated to laying out the science, mathematics, tools, and techniques necessary to understand subsequent chapters.

1.1 Crystalline Anisotropy

As stated above, the work in this thesis focuses on single-crystal materials, meaning that, ignoring unavoidable defects, all the atoms in a sample are neatly arranged into a single, well-defined lattice. The physical properties of single-crystal materials can be strongly orientationally dependent. Properties with such orientational dependence are described as anisotropic, and the orientation dependence itself is called anisotropy. Properties without such dependence are labeled isotropic. For solid-state dewetting, we are particularly concerned with the anisotropy of surface properties, such as surface free energy and diffusivity. Figure 1-2 illustrates how the orientation of a surface, relative to the crystalline lattice from which it is cut, can have a dramatic effect on the atomic structure of that surface. The details of how such structural differences manifest in surface properties are discussed below. In nature, most crystalline materials are polycrystalline, being composed of many small crystalline grains which meet at so-called grain boundaries. Each of these grains is single-crystalline, but may, depending on the growth and processing history of the material, have entirely random orientations. Surfaces in polycrystalline materials, therefore, have properties which can vary even along flat surfaces, as illustrated in figure 1-2. Thus, even if one had perfect knowledge of all the relevant materials properties and physics, without detailed knowledge about the sizes, shapes, and orientations of these grains, one cannot make detailed predictions about phenomena occurring at length-scales similar to the sizes of these grains, such as dewetting. Single-crystal materials, in contrast, present
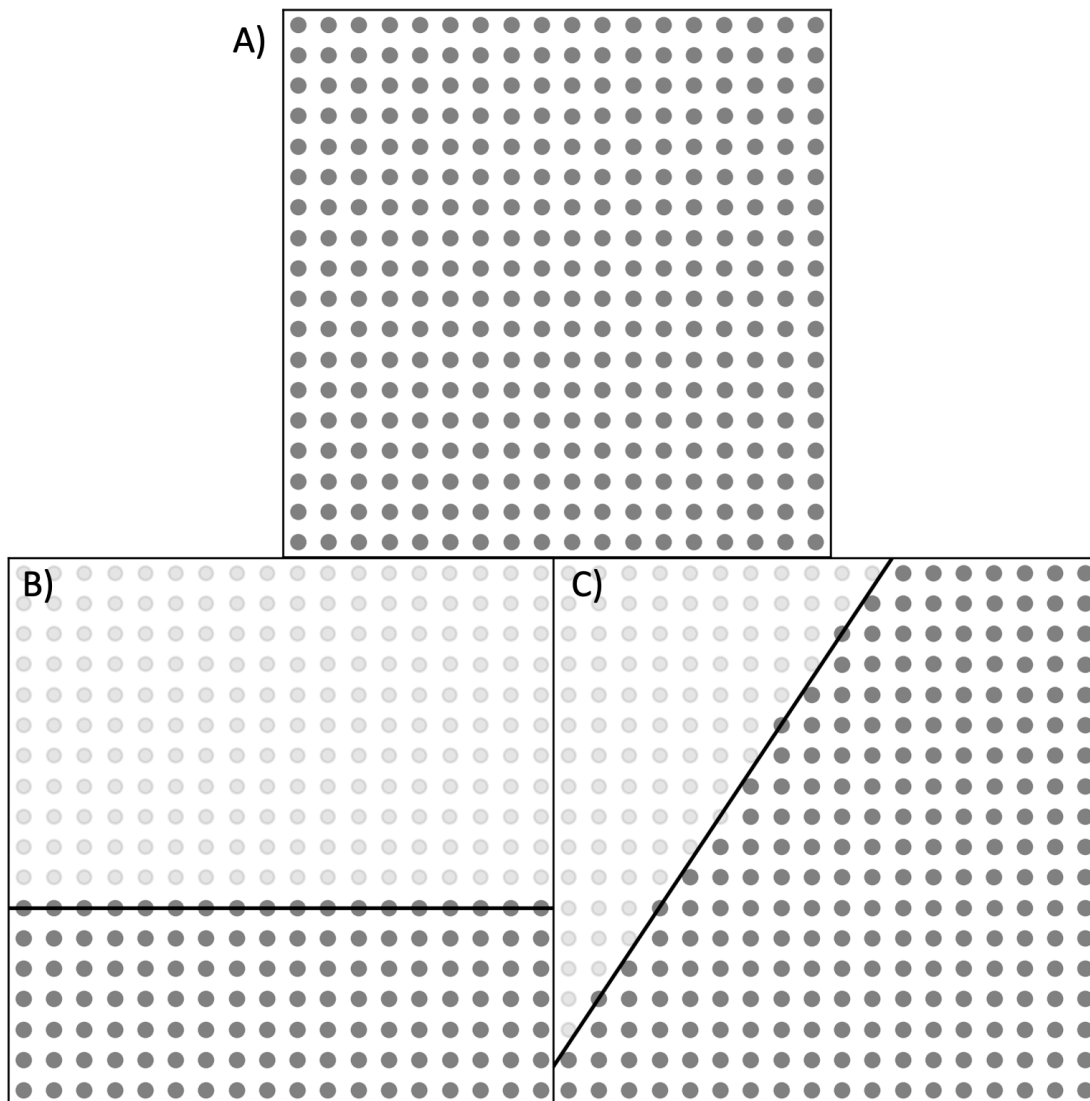
Figure 1-2: A figure illustrating, in two-dimensions, how cutting a single-crystal material along different orientations can yield surfaces with dramatically different structures. A) A simple square lattice with each gray circle representing an atom. B) A horizontal cut across crystal yields a simple flat surface. C) Cutting this lattice along a different line exposes a fundamentally different surface with a stepped structure.

a more controlled system for developing and testing our understanding of dewetting physics.
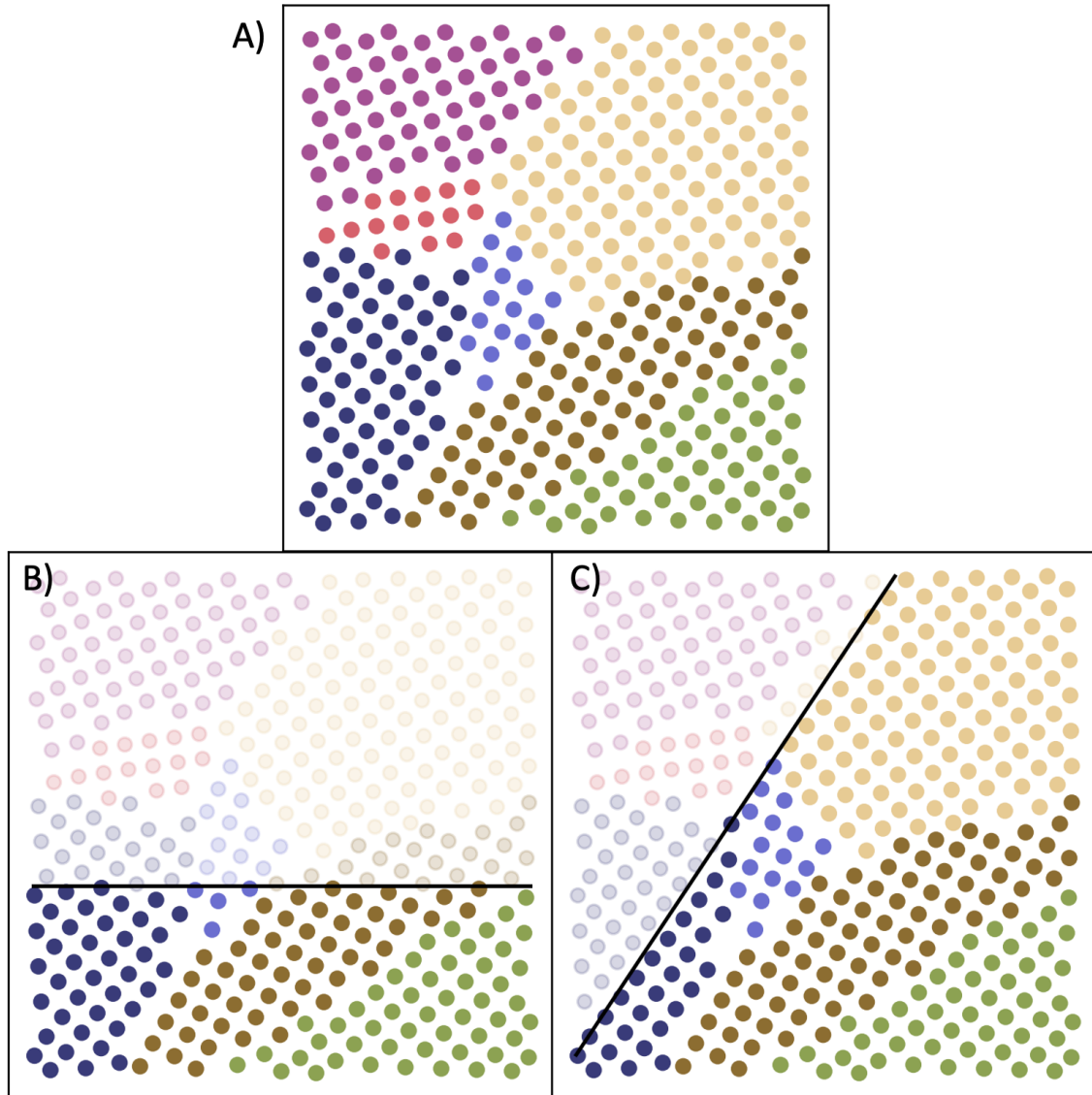
Figure 1-3: Repeating the construction from figure 1-2 for a polycrystalline material. Atoms belonging to the same grain have the same color, and the surfaces exposed in both B) and C) contain atoms from multiple grains, giving the surface irregular structure.

1.2   Diffusion

In general, diffusion is the stochastic motion of a chemical species which results in a net movement of the species along gradients of chemical potential, such that the flux of the species J is given by

$$J = -B\nabla\mu, \tag{1.1}$$

29

where B encodes information about how responsive the motion of the diffusing species is to gradients in chemical potential. In general, B is tensor-valued, and in certain contexts and conventions, this tensor is simply called the diffusivity, D, but in other contexts, D is defined such that B is the product of D and other material properties [9]. In ideal systems, in which chemical potential is simply proportional to concentration, equation 1.1 simply states that the random thermal movements of the particles will eventually tend to spatially homogenize the concentration over time. More generally, the chemical potential of a species is the partial derivative of the Gibbs free energy of the relevant system with respect to the quantity of that species and can be a function of factors such as concentration and position. Equation 1.1 embodies the fact that random movements from areas of high chemical potential to areas of low chemical potential will occur more frequently than those in the reverse direction. Thus, the free energy of the system will tend to decrease over time, until equilibrium is reached.

In crystalline systems, these random movements can occur within the bulk material if mediated by the presence of grain boundaries, vacancies, or other defects. These movements can also occur along the surface of the material, where no mediation is necessary. Particularly in single-crystal systems, in which grain boundaries are absent, diffusion along a material's surface can be orders of magnitude faster than volumetric diffusion. Solid-state dewetting tends to occur under such conditions, and surface diffusion will therefore be the primary focus of the remaining discussion below. Below, the terms of equation 1.1 are broken down in the context of surface diffusion.

1.2.1 Chemical Potential and Weighted Mean Curvature

For isotropic materials, the chemical potential at the surface is given by [10]

$$\mu = \gamma \kappa \Omega, \tag{1.2}$$

where γ is the surface free energy density of the material, i.e. the excess free energy associated with a surface of unit area, κ is the mean curvature of the surface, and Ω is the molar volume. This equation can be explained in many, fundamentally equivalent ways, but the following geometric explanation is most useful for the discussion here. Mean curvature is defined as divergence of a surface's normal vectors, taken along that same surface.
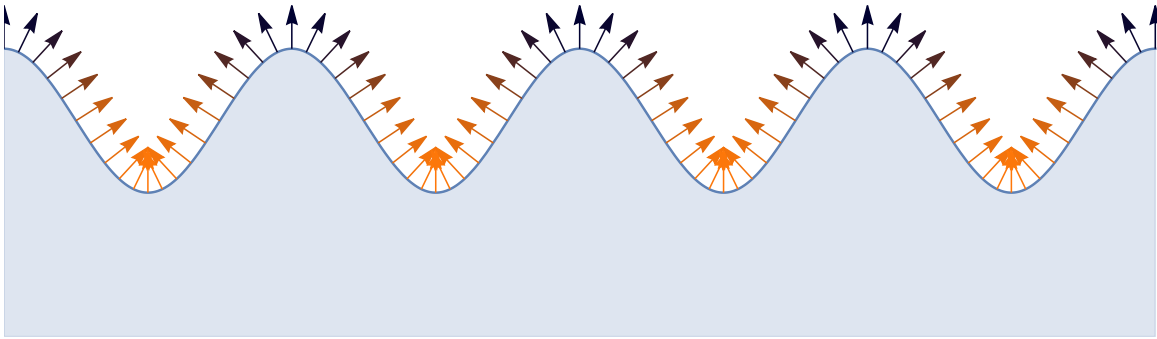
Figure 1-4: An illustration giving the intuition for why curvature can be defined as the divergence of $\hat{n}$. Normal vectors are plotted along an oscillating surface with converging vectors (indicating negative curvature) colored orange and diverging vectors (indicating positive curvature) colored black.

An alternative convention sometimes used in the literature defines mean curvature as half this quantity, such that it is the arithmetic mean of the two principle curvatures of a surface, however the convention used here is equivalent to rate at which new surface is created (or if curvature is negative, the rate at which existing surface is consumed) as volume is changed by the movement of this surface along it's normal direction. Stated more succinctly, though perhaps not entirely rigorously,

$$\frac{dG}{dn} = \frac{dG}{dA}\frac{dA}{dV}\frac{dV}{dn}$$
$$= \gamma\kappa\Omega$$

For crystalline materials, the chemical potential at the surface, and the diffusion driven by it, is more complicated, as the surface free energy density tends to be strongly anisotropic. This can be at least intuitively, if not somewhat simplistically, understood by returning to figure 1-2. In figure 1-2 A), each atom is bonded to its four nearest neighbors. If we imagine that the surfaces in B) and C) are created by cutting the lattice along the lines illustrated, we see that both surfaces have a characteristic number of broken bonds per unit length of surface. Surfaces with more broken bonds per unite length (or area in three spatial dimensions) tend to have higher surface free energy densities. In reality, entropic effects complicate this picture, as does the tendency of surface atoms to locally reconfigure themselves into surface reconstructions which reduce the number of unsatisfied bonds. At sufficiently high temperatures, entropic effects can dominate energetic effects and lead $\gamma(\hat{n})$ to become more isotropic, a condition known as thermodynamic roughening. Despite these additional complexities, counting broken bonds is a useful heuristic and tends to be at least directionally correct, with low index surfaces (those that leave few bonds unsatisfied) usually having low surface free energy densities. In any case, the function which describes the surface free energy density as a function of orientation is usually denoted as $\gamma(\hat{n})$. The orientational dependence of γ means that our simple equation for chemical potential (eq. 1.2) is no longer valid. However, we can derive an anisotropic analog to this equation by following the logic of its derivation. In the isotropic case, $\gamma\kappa$ gives the rate at which surface energy is increased with increasing volume for a surface with curvature κ. This equation is saying that $\mu = \frac{\partial G}{\partial N} = \frac{\partial G}{\partial V}\frac{\partial V}{\partial N}$. In this context, $\frac{\partial G}{\partial V}$ is known as the weighted mean curvature and is commonly denoted as κ^γ. For isotropic systems,$\kappa^\gamma$is further separable into $\frac{\partial G}{\partial A}\frac{\partial A}{\partial V} = \gamma\kappa$, but for anisotropic systems, such a separation is not valid. Instead, $\kappa^\gamma$is defined as the surface divergence of the Cahn-Hoffman vector, $\vec{\xi}(\hat{n})$ [11, 12]. The Cahn-Hoffman vector is defined as the gradient of the homogeneously extended surface free energy function $\gamma(A\hat{n}) = A\gamma(\hat{n})$, which gives the total surface free energy, rather than the surface free energy density, for a surface with normal vector $\hat{n}$ and surface area A. This construction is illustrated, in two dimensions, in figure 1-5. In the same way that the divergence of the normal
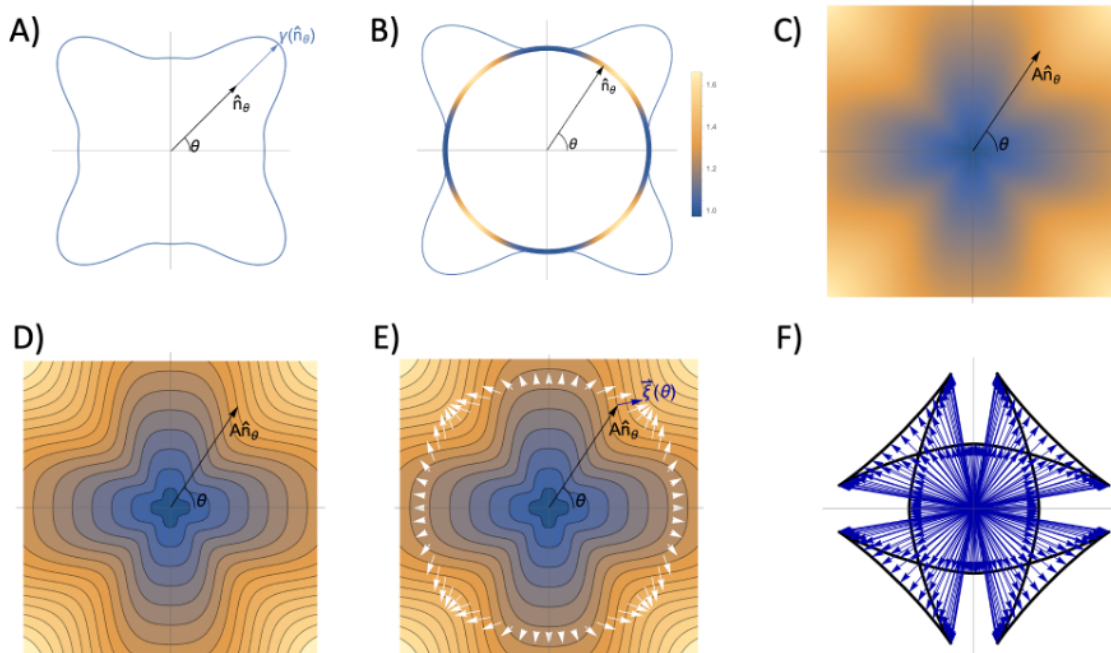
Figure 1-5: Figure 2: From left to right, top to bottom: a) Start with surface energy function $\gamma(\hat{n})$ shown as a polar plot, b) this can also be represented as a scalar function on the unit circle, c) extend this function over all of space such that $\gamma(A\hat{n}) = A\gamma(\hat{n})$, d) plotting isocontours of this function makes it easier to see where γ is changing most rapidly, e) $\vec{\xi}(\vec{n})$ is the gradient of this function— only $\vec{\xi}(\hat{n})$ for $\hat{n}$ of magnitude 1 is shown here for clarity, f) plotting just these highlighted $\vec{\xi}(\hat{n})$ with their tails at the origin yields the traditional ξ-vector construction, the convex hull of which is gives the equilibrium shape.

vector $\hat{n}$ is equivalent to the rate at which new surface is created as volume is swept out by a surface moving along it's normal, the divergence of $\vec{\xi}(\hat{n})$ gives the rate at which new surface free energy is created. Thus, $\kappa^{\gamma} = \nabla \cdot \vec{\xi}(\hat{n})$, implying that for an isotropic system, $\vec{\xi}(\hat{n}) = \gamma\hat{n}$.

1.2.2 Diffusivity

As discussed in section 1.2, diffusivity, D, is a property of the system which contains information about the kinetics of the system. As stated above, diffusive transport is the net result of many stochastic particle movements. Roughly speaking, the gradient of the chemical potential tells us the directional bias of these movements while the

diffusivity combines the rate at which these random events take place and the raw contribution of a single jump to the net flux. In an isotropic system, diffusivity is a scalar-valued function of the temperature of the system. In crystalline systems, surface atoms diffuse via discrete hops to neighboring, unoccupied surface lattice sites. These lattice sites are local energy minima, so the atoms must overcome relatively large energy barriers in order to hop from one site to another. At a given temperature, a surface atom is more likely to hop over a lower barrier than a higher one. This, combined with the possibility that hops in certain directions can span different physical distances, means that surface self-diffusivity can be highly anisotropic, depending on the symmetry of the underlying lattice. Complicating things further, this in-plane anisotropy is also a function of the surface's normal vector $\hat{n}$. Mathematically, there is nothing particularly special about this tensor, and it can certainly be described using traditional notation. However, in many parts of this thesis, I have chosen instead to express diffusivity as a function $D_{\mathrm{natural}}(\hat{n})$ which returns three-dimensional diagonal matrices of which the third diagonal value, corresponding to the out of plane direction, is 0. This $D_{\mathrm{natural}}(\hat{n})$ is thus paired with a transformation matrix used to convert chemical potential gradients and fluxes to the correct basis, such that

$$D\left(\hat{n}\right) = R^{T}(\hat{n}) D_{\mathrm{natural}}(\hat{n}) R(\hat{n}) \tag{1.3}$$

for D_{natural} of the form

$$D_{\mathrm{natural}} = \begin{matrix} d_1 & 0 & 0 \\ 0 & d_2 & 0 \\ 0 & 0 & 0 \end{matrix}$$

for an orthonormal basis $\{\hat{v}_1, \ \hat{v}_2, \hat{n}\}$

1.3 The Mullins Equation

The Mullins equation describes the evolution of a surface which is evolving toward equilibrium via the diffusion of the surface's constituent atoms along the surface itself, a process called surface self–diffusion. The equation expresses the fact that diffusive fluxes which cause a net accumulation of atoms at a given piece of surface will cause that piece of surface to grow outward along its normal [13]. Likewise, fluxes which cause net a net depletion of atoms in a given area will cause that area to recede. In isotropic systems, this can be simply expressed as

$$v_n = \frac{D\nu\Omega^2}{k_bT}\nabla^2\gamma\kappa \tag{1.4}$$

Where ν is the surface concentration of atoms, Ω is the atomic volume, k_b is Boltzmann's constant, and T is the temperature of the system. More generally, the velocity of a surface along its normal is given by

$$v_n = -\Omega\nabla \cdot J \tag{1.5}$$

for diffusive flux

$$J = -\frac{D\nu\Omega}{k_bT}\nabla\kappa^\gamma \tag{1.6}$$

In a crystalline system, ν also has an orientational dependence, so it is convenient to gather all the materials properties into one term $B(\hat{n})$, a tensor of the same form as $D(\hat{n})$ discussed above, such that

$$v_n = B(\hat{n})\nabla^2\kappa^\gamma \tag{1.7}$$

For certain initial geometries, studying the long-time behavior of the isotropic Mullins equation is analytically tractable, and a great deal of our understanding of dewetting behavior comes from early theoretical work on isotropic systems. However, in anisotropic systems, the Mullins equation generally becomes analytically unsolvable, leaving numerical and computational approaches as the only viable options for mod-

eling the behavior of physically realistic systems.

1.4 Equilibrium Shapes

1.4.1 Isotropic Materials

We have shown above that the flow of surface atoms is driven by gradients in κ^γ, which implies that the system reaches local equilibrium when κ^γ is constant across the entire surface of the object. This is equivalent to stating that the total surface free energy of the system is a local minimum. For a free-floating (i.e. not in contact with a substrate) object with isotropic surface energy, the shape which minimized surface free energy is simply the shape which minimizes overall surface area for a given volume, a sphere. For an isotropic material in contact with a substrate (also assumed to be isotropic), the equilibrium shape is a fraction of a sphere resting on the substrate. The angle formed by the surface of the sphere and the substrate along their line of contact—called the triple line in reference to the particle, substrate, and surrounding vapor all making contact along this line—is called the contact angle and is given by the Young-Dupre equation [14]

$$\gamma_{PV}\cos(\theta_c) + \gamma_{PS} - \gamma_{VS} = 0. \tag{1.8}$$

Where γ_{PV} is the particle-vapor surface free energy density, γ_{PS} is the particle-substrate interfacial free energy density, and γ_{VS} is the surface free energy density of the bare substrate in contact with the vapor. See figure 1-6 C) for an illustration of how these quantities determine the contact angle.
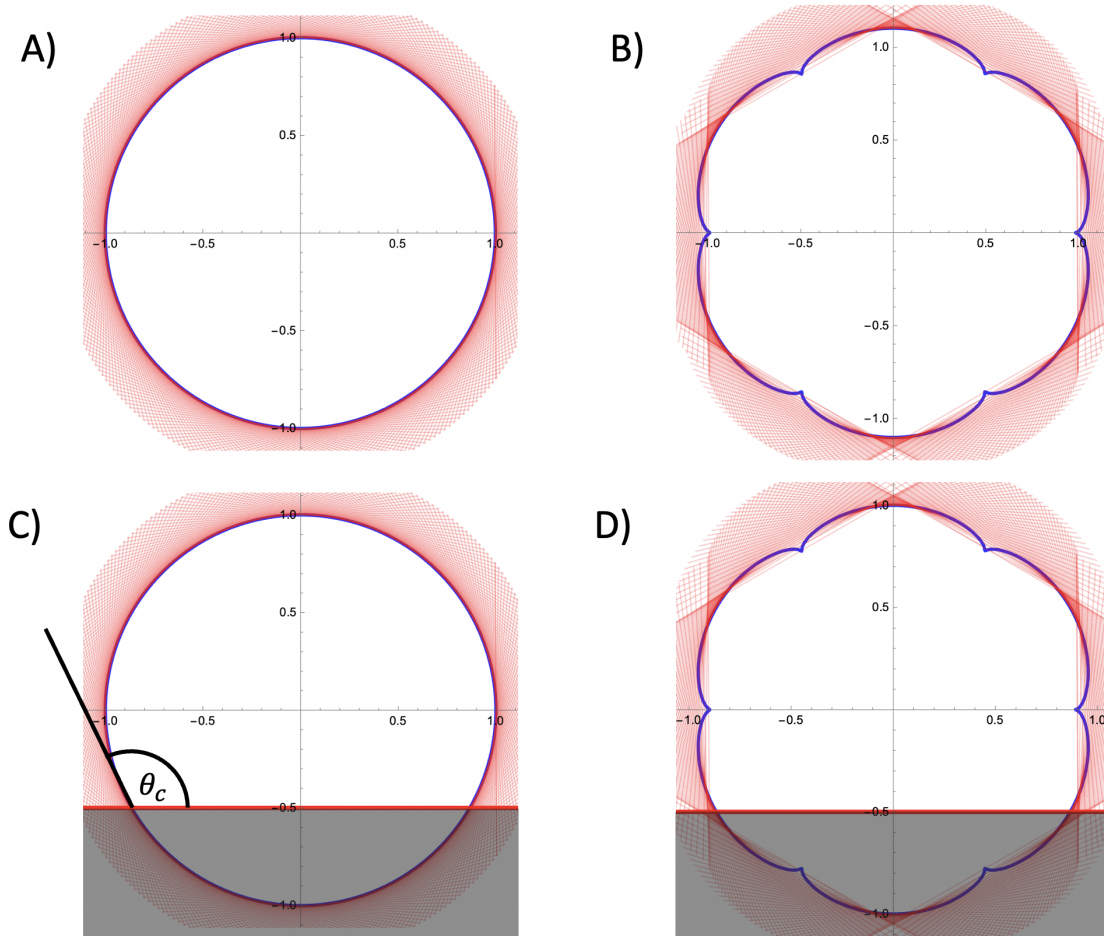
Figure 1-6: Examples of the Wulff and Winterbottom constructions for isotropic and anisotropic materials. A) Isotropic Wulff construction; B) Wulff construction for material with hard anisotropy; C) Winterbottom construction for isotropic material for $\sigma = \frac{\gamma_{VS} - \gamma_{PS}}{\gamma_{PV}} = -0.5$; D) Winterbottom construction for an anisotropic material with the same σ as C) Note that the contact angle in C), $\theta_c = 135°$, matches that predicted by Young-Dupre. The material in D) is said to have effective contact angle of 135°. In general, anisotropic materials can have facets with different energies, unlike the simple example shown here.

1.4.2 Anisotropic Materials: The Wulff and Winterbottom Constructions

For an anisotropic material, the shape which has uniform κ^γ, and thus minimizes surface free energy, is not a sphere but can be found through simple geometric constructions. The method most often used in the literature is called the Wulff construction [15, 16], and it entails taking the inner envelope of lines perpendicular to

$\hat{n}$ with distance $\gamma(\hat{n})$ from the origin. The Winterbottom construction [16], used for materials in contact with substrates, is exactly the same as the Wulff construction, except $\gamma(\hat{n})$ is replaced with $\gamma_{PS} - \gamma_{VS}$ for $\hat{n}$ corresponding to the particle-substrate interface, see figure 1-6. For anisotropic materials, γ_{PS} and γ_{VS} are taken to be those corresponding to the orientation of the particle–substrate interface. The quantity $\frac{\gamma_{VS} - \gamma_{PS}}{\gamma_{PV}}$ is often denoted by σ, such that $\arccos(\sigma)$ gives what is called the effective contact angle, in reference to equation 1.8. It is also true that that the equilibrium shape of a material is given by the convex portion of $\vec{\xi}(\hat{n})$, while the non-convex parts correspond to metastable and unstable orientations.

1.5 Thin Single Crystal Films

As stated above, experiments designed to explore the details of how crystalline anisotropy impacts dewetting behavior require micro- and nano-scale features fabricated from single-crystal materials. The first step in fabricating such experimental structures is the deposition of large-area single-crystal thin films. Unless otherwise stated, the information in this section is all adapted from Prof. Carl Thompson's course, "Materials Processing for Micro and Nano-Systems" [17]. Other good resources are "Silicon VLSI Technology" by Plummer, Deal, and Griffin [18] as well as "Materials Science of Thin Films" by Ohring [19]. In general, metal and semiconductor films can be deposited through either physical or chemical vapor deposition (PVD or CVD). In PVD processes, a relatively large source of the material to be deposited is energized—through either direct heating or bombardment with some form of energy—causing it to eject material. Depending on the geometry and other details of the deposition system, some fraction of the ejected atoms impinge upon and stick to the substrate onto which material is being deposited. If deposition is continued long enough, these atoms will cover the entire surface of the substrate, constituting a film. Deposition is generally conducted under conditions at which the mobility of deposited atoms is low relative to the deposition flux, leading to films which are metastable as deposited. These films can be annealed at higher temperatures post deposition to achieve a lower

38

energy state. By contrast, CVD processes generally flow precursor gases over the substrate. These gases either decompose on the substrate to leave behind material and, if multiple gases are being used, undergo surface-catalyzed chemical reactions which also leave behind material of the desired composition. The work in this thesis focuses on materials which tend to be grown through PVD processes (e–beam evaporation for our Ni films and sputtering for our Ru films), so CVD processes will be ignored for the rest of this discussion.

In principle, PVD can make use of single-crystal, polycrystalline, or amorphous substrates, and the details of the substrate surface can have large effects on the character of the deposited film. For example, FCC metals are often deposited on oxidized silicon substrates, the top surface of which is amorphous. The resulting films are invariably polycrystalline, though the individual grains often have a (111) texture, meaning that disproportionately many grains have (111) top surfaces because of that surface's low energy. In order to obtain single-crystal films, a single-crystal substrate is required. If a film can be grown on a single-crystal substrate such that two lattices align in an energetically favorable way, that film is said to be epitaxial. However, an epitaxial relationship between substrate and film is no guarantee of a single-crystal film, as other factors such as contamination, background deposition pressure, and high deposition flux can confound the formation of a single-crystal film. To obtain single-crystal films, one generally wants to achieve Frank-Van der Merwe (FvM) growth, in which the film grows roughly one atomic layer at a time, across the entire surface of the substrate. FvM growth is enabled by high atomic mobility, relative to the incoming flux of atoms, as well as low interface coherency strain between the film and the substrate. It is also possible to grow single-crystal films through the Volmer-Weber (VW) growth mode in which atoms first form isolated clusters on the substrate surface which coalesce as they grow. This growth mode tends to occur when mobility is lower and the bonds between film atoms are much stronger than those between the those atoms and the substrate. This description matches the conditions under which both our Ni and Ru films were depositied, and it is very likely that these films grew by the VW mechanism. The Stranski-Krastanov growth mode is intermediate between

39

these two, with a thin layer coating the entire substrate before clusters begin to form at larger thicknesses. In practice, developing a protocol for obtaining large area single-crystal films can be quite difficult, requiring tight control over variables such as temperature, deposition rate, and background pressure. To deposit our single-crystal Ni films, we use our own Balzers UMS500 electron beam system which, without the time constraints of shared equipment, we are able to pump down to and maintain a pressure in the mid 10^{-7} Torr range. Our system is also very clean because of the limited selection of materials we deposit in it. We deposit films at a rate of 0.5Å/s and are consistently able to achieve single crystal films of uniform thickness across our 1 cm^2 MgO substrates. Preparation for a deposition involves a prolonged bake of the chamber and the substrate while under vacuum to drive off contaminants. Our Ru films are deposited by collaborators at the University of Central Florida, using DC magnetron sputtering, as discussed in chapter 4.

1.6 Patterning

There are several ways of patterning thin films into useful micro- and nano- structures, but lithographic patterning and lift-off processes will be the only two discussed here. As in the above section, the course notes for "Materials Processing for Micro and Nano-Systems" [17] provide the most comprehensive overview of this topic that I am aware of. Plummer et al. [18] is also a good reference for this topic.

1.6.1 Lithographic Patterning

Lithographic patterning usually involves placing a patterned protective coating over the top of a film and then etching away all of the film which is not covered by the protective coating. In photolithography, special polymers called photoresists are uniformly applied to the surface of the film to be patterned. The photoresist is then selectively exposed to light, either through the use of a shadow mask which is placed between the film and the light source to cast an engineered shadow over the resist or

by direct write systems which scan a laser across the surface of the resist to draw the desired pattern. The sample is then baked for a short period of time to aid in curing the photoresist. Resists which cure in the regions without light exposure are called positive resists, and those which cure in the lighted regions are called negative resists. The uncured resist is then chemically removed and the unprotected areas of the film are etched away by either chemical etching or by physical etching, such as exposure to an ion beam. Finally, the cured resist is dissolved in a solvent such as acetone, and a patterned film is left behind. Past work in our group using photolithography has achieved resolutions down to about 2μm; for resolutions below this, electron beam (e–beam) lithography is necessary. Electron beam lithography is similar to direct write photolithography in principle but uses a focused beam of electrons, rather than a laser, to expose the resist. Our Ni work makes use of photolithography while our Ru work requires much smaller feature sizes and thus makes use of e–beam lithography. As straightforward as it may seem, lithographic patterning involves a massive parameter space, including choice of chemicals, temperatures, intensity and duration of exposure, and much more. Developing protocols that reliably achieve high resolution is an entire discipline on its own.

1.6.2 Lift-off Patterning

Although lift-off patterning makes use of lithographic processes, it is distinct from lithographic patterning in its fundamental approach to patterning the film. The process described above is called subtractive patterning while lift-off patterning is an example of additive patterning. In lift-off patterning, a pattern is laid down on a bare substrate before deposition. This pattern, called the sacrificial layer, is the inverse of the desired final features and is usually made lithographically. A film of the desired material is then deposited over the entire area of the sample, with the sacrificial layer protecting those areas of the substrate which are intended to remain bare. The sacrificial layer is then chemically dissolved, washing away the material deposited on top of it as well and leaving behind a patterned film on the substrate.

1.7 Observed Phenomenology

Experiments conducted in patterned single-crystal films have yielded myriad fascinating behaviors, a brief overview of which will be provided here.

1.7.1 Edge Retraction

The simplest dewetting phenomenon is the retraction of a film's edge, which has been extensively modeled and studied experimentally—Refs. [6, 20–25] are all canonical examples. As illustrated in figure 1-1, in an isotropic system, the material rejected from triple-line accumulates in a growing rim which propagates along with the triple-line; figure 1-1 is a good graphical reference for this entire subsection. After an initial transient, the total retraction distance of the edge scales as $t^{2/5}$. Ahead of the rim, the height of the film develops oscillations which decay in amplitude with distance from the rim. The first film height minimum is often referred to as the valley, and it grows monotonically deeper as the film edge retracts. Eventually, the valley makes contact with the substrate, turning the rim into an isolated wire and starting the process of edge retraction over again, see figure 1-1. In strongly anisotropic systems, this behavior is more complicated, as the presence of facets can profoundly impact the behavior of the valley. In fully faceted systems, modeling work using the crystalline method found that films with a stable top facet were entirely impervious to valley formation [26]. More anisotropic complexity can arise if the in-plane orientation of the film's edge is itself unstable. In some materials, such as ruthenium, such a situation leads to chaotic dewetting, while in other materials, such as Ni, such edges can undergo the fingering instability, in which the dewetting front develops parallel protuberances, called fingers, of characteristic size and spacing [8]. These fingers propagate with constant velocity, greatly increasing the rate of dewetting.
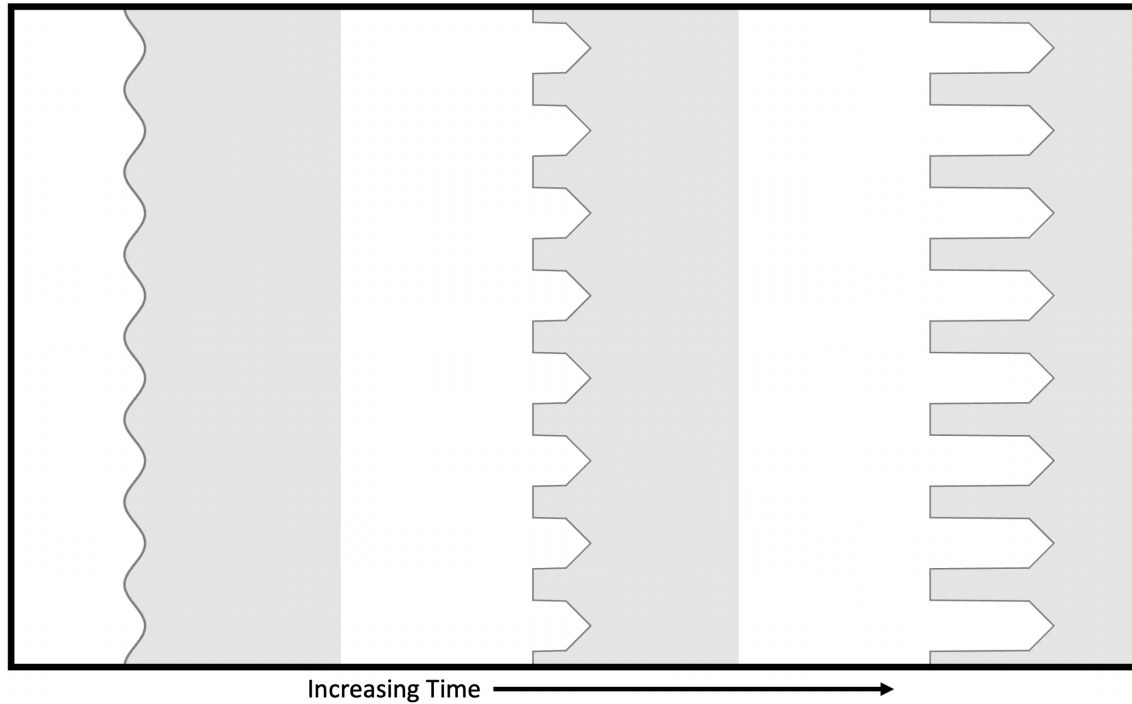
Figure 1-7: A schematic of a perturbed retracting film edge, viewed from above, developing the fingering instability
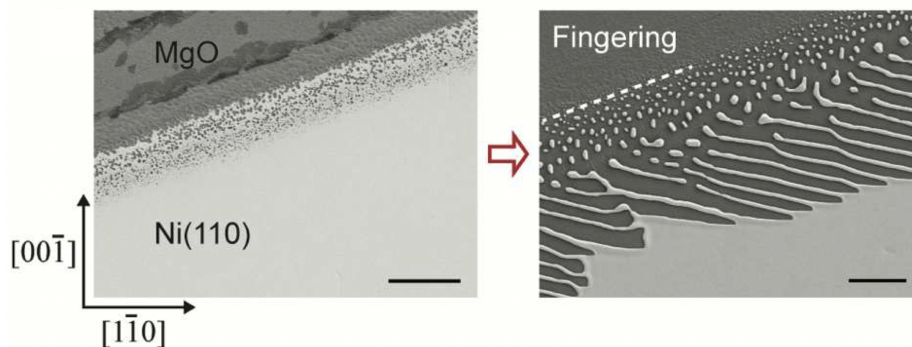
Figure 1-8: A 120 nm–thick Ni (110) film with an intentionally rough edge developing the fingering instability [8].

1.7.2   Hole Growth

Holes are edges which close on themselves, and as such, they exhibit much of the same dewetting behavior as simple edges. As will be discussed in detail in chapter 5, the feature which distinguishes the phenomenology of holes from that of straight edges is that the growth of a hole implies the elongation of it's associated triple-line. The implications of this are one area of focus of this thesis. The rim surrounding a hole can

43
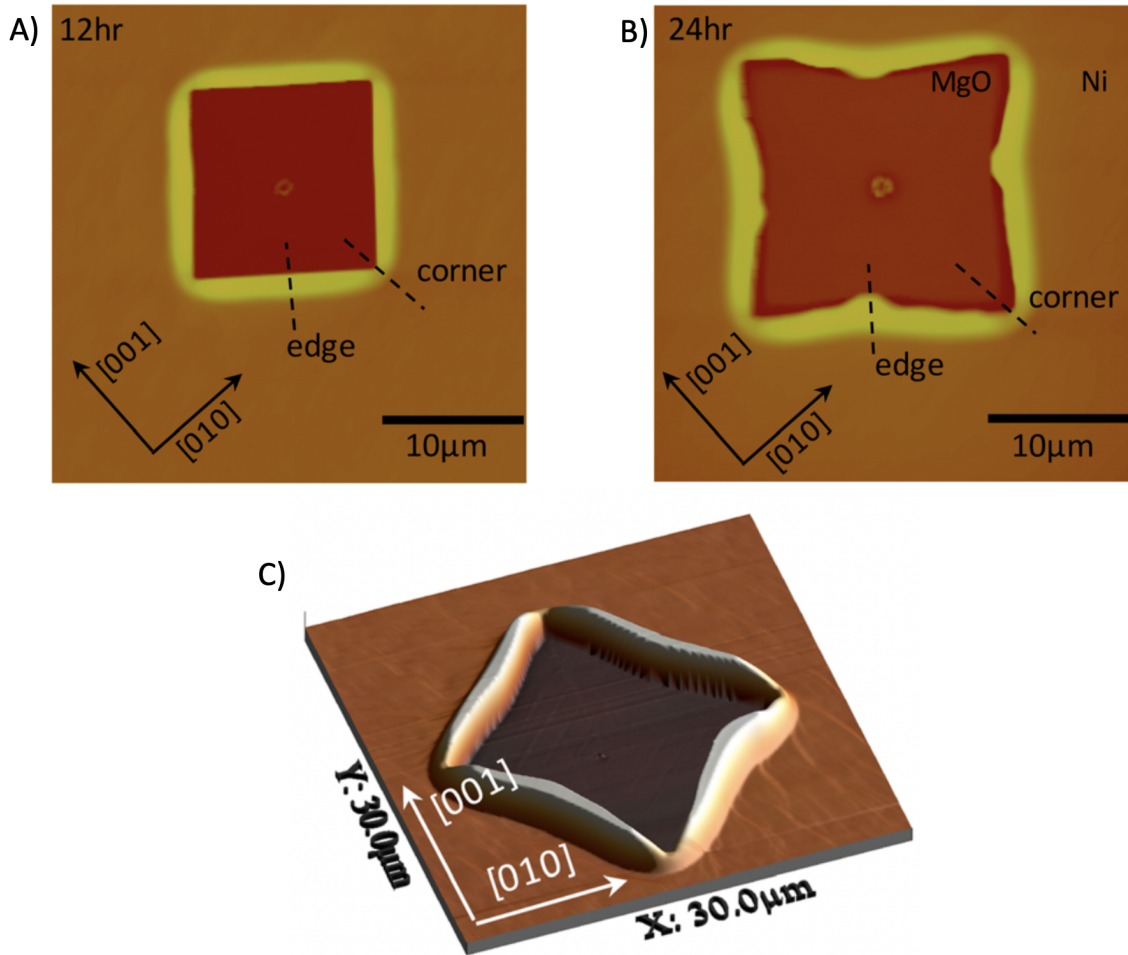
Figure 1-9: AFM images of the corner instability in 130 nm–thick Ni (100) films [7]. A) shows a hole which has reached its kinetic Wulff shape but has not yet undergone the corner instability. B) shows a hole which has undergone the corner instability. C) highlights how much lower the rim height can be at the corner of a hole. Later stages of this type of behavior are shown in figure 1-10 A) below.

touch down to the substrate and cause pinch-off, or the corners of a hole can become unstable and exhibit behavior analogous to the fingering instability [7], see figures 1-9 and 1-10 A). These unstable corners can develop secondary instabilities along their length, yielding behavior evocative of dendritic solidification. Alternatively, as in (0001) Ru films, holes can nucleate far more complex behavior, such as the formation of channels and rings, see figure 1-10 B).
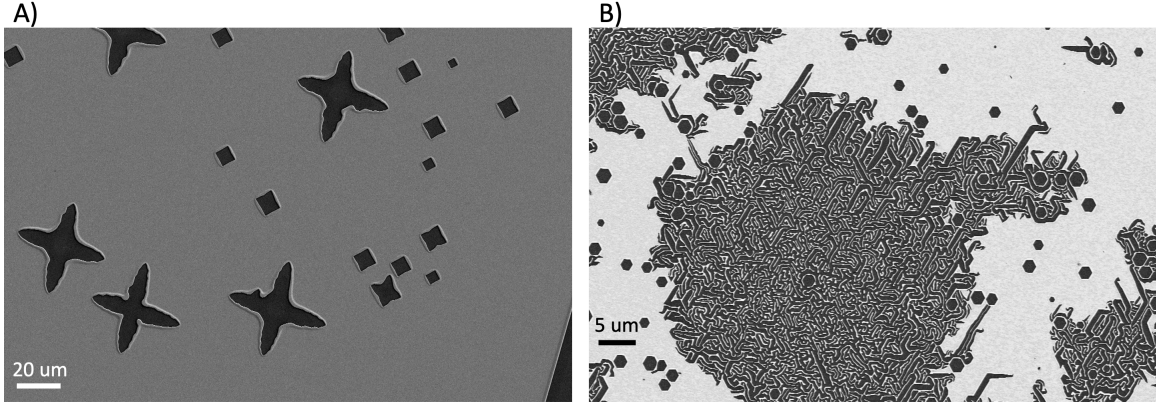
Figure 1-10: A) Holes in an $85\,\text{nm}$–thick film including early stage holes (small squares), holes beginning to undergo the corner instability (see chapters 2.2.2 and 5), and holes with fully dendritic corners; B) Hole growth and other subsequent instabilities in a 10nm-thick (0001) Ru film.

1.7.3 Wire Stability

Although planar films are often used to study dewetting, the behavior of wires and high aspect ratio geometries is at least as important from a technological standpoint. Studies of wire-like geometries subject to capillary forces date back to the 19th century, when Rayleigh and Plateau studied the breakup of liquid jets (i.e. cylindrical streams of free-flowing liquid) into discrete droplets [27–29]. Rayleigh determined that cylinders evolving under capillary forces, regardless of the mechanism of mass transport, are unstable to perturbations of their radius with wavelength greater than $\lambda > 2\pi R_0$, for unperturbed cylinder radius R_0 [27, 28]. This instability has come to be known as the Rayleigh instability. Later, Nichols and Mullins extended this analysis to the specific case of diffusive mass transport along the surface of the cylinder and found that the fastest growing perturbations have wavelength $2\sqrt{2}\pi R_0$ [30]. Nichols also showed that unperturbed, finite-length cylinders will break up in a process analogous to edge retraction and pinch-off called ovulation [31]. In anisotropic materials, the stability of long wires can be extremely orientationally dependent, with wires oriented such that they are bound by equilibrium orientations exhibiting strong resistance to the Rayleigh instability [5, 32]. We examine the effects of this anisotropy in detail in chapter 4.

45

1.8   Annealing Conditions

1.8.1   Temperature

As discussed above, solid-state dewetting only occurs over relevant time-scales at elevated temperatures. This is because diffusivity has an Arrhenius dependence on temperature, meaning that $D \propto \exp(-E/k_b T)$ for some characteristic energy E [33]. The temperature at which dewetting behavior becomes significant—how exactly significance is defined is application dependent—is termed the dewetting temperature [34]. This temperature is also strongly dependent on the thickness of the film [35], as thinner films will have initially higher curvatures driving dewetting. Thinner films also form holes more readily and have smaller diffusion distances over which dewetting occurs, reducing observed dewetting temperatures. Holding geometry constant, a good rule of thumb is that similar materials (e.g. FCC metals) will have similar homologous $\left(\frac{T}{T_{\mathrm{melt}}}\right)$ dewetting temperatures [34]. In anisotropic systems the diffusivity and surface free energies of different orientations will have different temperature dependencies, meaning that almost every term in equation 1.7 will have complicated temperature dependence.

1.8.2   Ambient

As a surface phenomenon, dewetting behavior can be extremely sensitive to ambient conditions. For example, our group has shown that the partial pressure of O_2 has a profound effect on the dewetting behavior of Ni films. At relatively high partial pressures of O_2, Ni films will be coated in NiO. At lower partial pressures, this oxide begins to disappear, leading to different dewetting behavior. A detailed overview of the effect of ambient conditions on the surface reconstruction and dewetting behavior of Ni films is given in reference [36]. Most of the work presented in this thesis was conducted using flowing 5% H_2, 95% N_2, intended to fully remove the native oxide of Ni and Ru films. For example, for our Ru films, we used an Ellingham diagram [37] to

determine that we would need to bring the oxygen partial pressure in our furnace well below 7×10^{-11} atm to be sure that the native oxide is removed. Using this reducing gas flowing at 2300sccm, we measured $P_{O_2} = 2.7 \times 10^{-22}$ atm, while annealing an Ru sample. Beyond considerations of a film's native oxide, different ambient conditions can lead to different surface reconstructions, meaning that surface atoms move to locations other than those defined by the bulk crystalline lattice, which can lead to significantly different Winterbottom shapes. The effects of such changes are examined in chapter 3.

1.9 Electron Microscopy

1.9.1 SEM

After annealing our films, it is necessary to determine the morphological changes which have occurred during the anneal. Our go-to method for this is scanning electron microscopy, as it allows us to examine the films over a wide range of magnifications while doing minimal damage to the sample. Imaging our samples is relatively straightforward, though we do have to be cognizant of the insulating nature of our substrates. To mitigate charging effects, good electrical contact must be made between the top surface of the sample and the sample holder, and a low accelerating voltage must be used. SEMs like the Zeiss Merlin in CMSE and the Zeiss Ultras and Supra at Harvard CNS can achieve quality images of our samples using an accelerating voltage as low as 2kV. Under these conditions, we tend to obtain the best images using the Everhart-Thornley secondary electron detector, called SE2 on Zeiss microscopes.

1.9.2 TEM

The SEM is an excellent tool for for studying morphologies down to ~ 10nm—higher resolutions are possible in more conductive samples that can tolerate higher accel-

erating voltages—in a non-destructive manner. However, when higher resolution is needed, or when a cross-sectional perspective is more informative than a top-down view of surface topography, transmission electron microscopy is needed. As their name suggests, TEMs transmit a focused beam of electrons through the sample being imaged, with the image being constructed from the transmitted beam. If the sample is aligned such that columns of atoms run parallel to this beam, atomic-scale resolution is possible. However, this imaging power comes with important caveats, the most significant of which is that the sample must be sufficiently thin for the electron beam to pass through it, on the order of tens of nanometers for the types of samples we image. Additionally, the electron beam is extremely power dense, with accelerating voltages in the hundreds of kV up to low MV being typical. This means that the beam itself can heat or otherwise damage the sample as it is being imaged.

1.9.3 FIB

As stated above, TEM samples must be extremely thin to maximize resolution. For samples like the ones studied in this thesis, this means that cross-sectional slices must be cut out of the sample. The tool used create cuts at the nanometer scale is the focused ion beam. Typically paired with an SEM in what is referred to a dual beam system, an FIB operates on a similar principle to SEMs, except that it scans a beam of ions across the sample, rather than a beam of electrons. This beam can be used to image a sample, but it's primary purpose is to use the beam much like a nanoscale water jet cutter and cut the sample in an act referred to as milling. Traditionally, FIBs made use of gallium ions for this purpose, although systems exist which use other ions. Early proof of concept work for our work on Ru nanowires, see chapter 4, used a xenon plasma FIB to fabricate nanowires at high resolution without implanting gallium into the sample. When the FIB is used to cut cross-sections for TEM imaging, these cross sections can be lifted out of the sample using a piezo-electrically controlled probe which tapers down to a nano-scale tip.

1.9.4 EBSD

Electron backscatter diffraction is a common technique available in many SEMs which provides detailed information about crystallographic orientation at small scales. The sample is tilted at a large angle, relative to it's typical orientation normal to the incoming electron beam. The initially focused electron beam is diffusely scattered as it travels through the sample, leading to a broadened distribution of electron directions, peaked at the initial direction. These electrons then Bragg diffract, yielding cones rather than spots because of the initial diffuse scattering [38]. The resulting patterns can be interpreted using software, allowing users to easily map the crystallographic orientation of sample features including, in our case, the edges of hexagonal rings in dewetted Ru films. EBSD can also be used as an additional check on whether or films are truly single crystal.

1.10 Atomic Force Microscopy (AFM)

Atomic force microscopes make use of a vertically oscillating probe, often made of silicon, which tapers to a very fine tip—the Bruker RTESP-300 AFM probes we use in our lab have a nominal tip radius of 8nm. In tapping mode, this AFM tip is scanned across a sample's surface, as it oscillated up and down, building up a topographical image of the sample's surface. Image resolution in the plane of the surface is dependent on the choice of probe, scan rate, and other variables, but vertical resolution is consistently on the order of a nanometer.

1.11 Data Analysis

After a series of experiments, there are often measurements, such as hole size and finger spacing, that need to be extracted from the SEM images which were taken. A single experiment can generate dozens or even hundreds of images, and analyzing these images can take a great deal of time. Additionally, even using software

tools like ImageJ, such analysis requires significant human input which can introduce unnecessary error. For these reasons, I have developed a Python package which automates these measurements. It is able to read in images, acquire the physical size of a pixel using Tesseract optical character recognition, locate natural holes within the image, and measure the holes' area, perimeter, and diameter. Measuring finger spacings is similarly easy, though the user still has to define the cross-section along which the spacing should be measured. The package is well-documented and also includes commands for analyzing whole batches of data.

1.12 The Work in this Thesis

Building on the concepts and techniques outlined above, the work presented in the rest of this thesis seeks to explore and better understand the rich behavior arising in single-crystal films undergoing dewetting. In chapter 2, a new technique for simulating surface self-diffusion and solid-state dewetting in strongly anistotropic systems is demonstrated. In the next chapter, this technique is applied to the dewetting of Ni (110) films in both H_2– and CO–based ambients, highlighting the importance of ambient conditions and showcasing our simulation technique's ability to reproduce experimental results. Chapter 4 looks at the stability of of single-crystal Ru nanowires, and its striking dependence on orientation, using both experiments and simulations. Chapter 5 explores the corner instability and dendritic dewetting through a new theoretical lens, drawing an analogy to dendritic solidification and viscous fingering. Finally, in chapter 6, the key findings of this work are summarized and potential areas of future work are discussed. For the interested reader, a discussion on constructing anisotropic $\gamma(\hat{n})$ and $\vec{\xi}(\hat{n})$ is presented in appendix A.

Chapter 2

A Level-set Method for Simulating Dewetting in Systems with Strong Crystalline Anisotropy

As outlined in the introduction, solid-state dewetting, and capillary-driven surface self-diffusion more generally, can give rise to a host of complex phenomena. Accurately modeling the full continuum of dewetting behaviors, especially in systems with strong anisotropy, is an open problem in materials science. In isotropic systems, the behavior of dewetting systems is described by the Mullins equation [40], see chapter 1.3. As with other 4th order partial differential equations, traditional numerical methods for solving the Mullins equation require very small time steps to prevent numerical instability [41]. For crystalline films, anisotropy necessitates a reformulation of the Mullin's equation. In addition to facets, corners, and edges being non-differentiable, the chemical potential is not directly related to the geometric mean curvature [12]. Furthermore, anisotropic surface diffusivities require that the scalar surface diffusivity be replaced with a surface diffusivity tensor. Experimental observations of dewetting wires and films also show behaviors which include topological changes that are troublesome for Lagrangian, front-tracking numerical methods.

A deeper understanding of the effects of crystalline anisotropy on solid state dewetting is important because of both the striking behaviors to which it gives rise and the impact these behaviors have on the use of dewetting to create intermediate structures of use in fabricating devices [34, 42, 43]. In anisotropic systems, retracting rims develop faceted profiles (see figure 2-1 C)), and small deviations in the alignment of patterned features relative to a film's crystalline axes can yield profoundly different behavior [5, 8, 36]. While this rich and complex behavior is of interest to both experimentalists and modelers, improved numerical methods are required to predict and understand these phenomena.
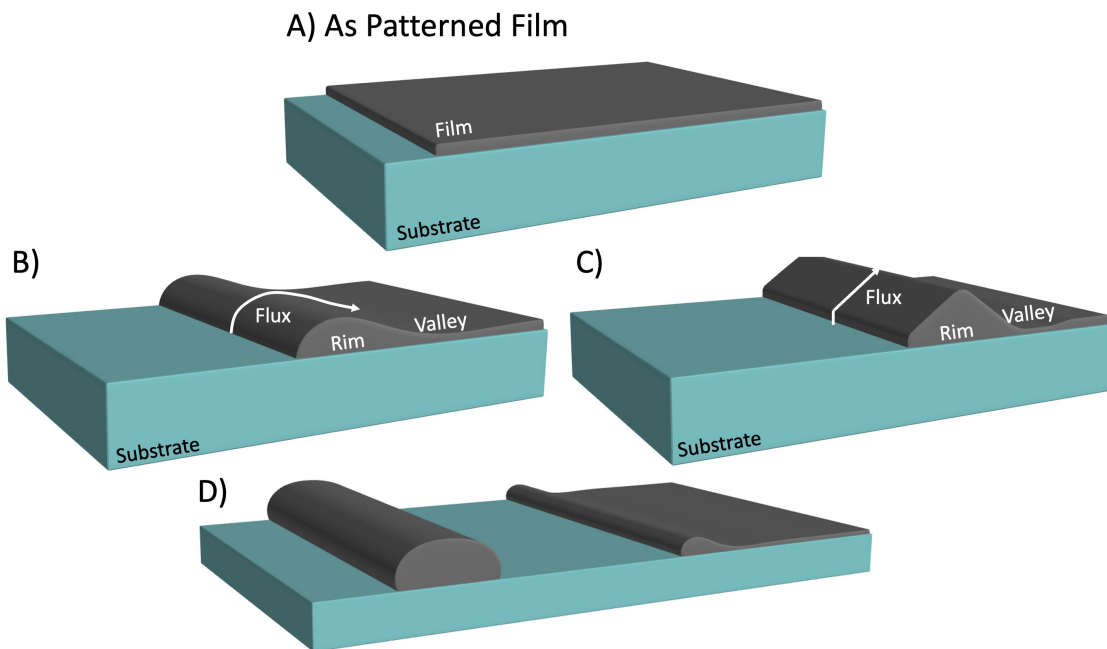
Figure 2-1: Schematic illustration of retraction of a film edge in isotropic and strongly anisotropic films. Material dewetted from the substrate accumulates in a rim which propagates into the film. A) shows the as-patterned film, B) shows an intermediate dewetting morphology for an isotropic system, C) shows the same for a simple anisotropic system, D) shows an isotropic system which has dewetted to the point of pinch-off. In isotropic systems, a valley always forms behind the rim while the extent of valley formation in anisotropic systems is determined by material properties. This will be discussed at greater length below.

To this end, we present a level-set numerical approach for simulating the morphological evolution of anisotropic materials undergoing dewetting and surface diffusion

mediated evolution driven by capillarity more generally. The method includes the effects of anisotropic surface energy and an anisotropic surface diffusion coefficient tensor. Our method reproduces experimental observations, including faceting and topological transitions. We have also tested our method in the absence of anisotropy and show that we can reproduce previous analytical, numerical, and computational results.

For isotropic systems, there are many examples of modeling behavior governed by the Mullins equation. This equation was initially applied to grain boundary grooving [13] and the evolution of surfaces of revolution [30, 44], including Rayleigh instabilities [27], which have since been modeled in more complex systems such as material contact with a substrate [45] and material constituting an intragranular phase [46]. Brandon and Bradshaw [20] conducted early work on solid-state dewetting, in which they developed a simple analytical model in which a straight dewetting edge's retraction distance scales with $t^{2/5}$. Computational [21, 24, 26] and experimental [25, 47] work reproduced approximate $t^{2/5}$ scaling at sufficiently long times. Nichols later showed that finite cylinders are also prone to ovulation [31]—the repeated pinching off and spheroidization of a cylinder's ends—in addition to the Rayleigh instability. Smereka developed a level-set method to model evolution mediated by surface self-diffusion in isotropic systems, but did not model interactions with substrates [41]. Jiang et al. also conducted phase-field simulations of several isotropic solid-state dewetting phenomena [48].

Other approaches that go beyond the direct application of the Mullins equation are needed for anisotropic surface energies. The "crystalline method" enables modeling evolution through the movement, creation, and annihilation of facets in fully-faceted systems [49–51]. It has been used to study edge retraction in fully faceted systems, including the effects of assigning different diffusivities to different facets [26]. Dornel et al. constructed an anisotropic extension to the method in Ref. [21] and explored edge retraction behavior in Si films [23]. Burger et al. utilized anisotropy in level-set method simulations [52]. Jiang et al. simulated anisotropic dewetting using a

finite-element method [53, 54] and Pierre-Louise et al. used a Kinetic Monte Carlo (KMC) method to simulate dewetting [55–57]. Kim and Thompson used KMC to study the orientational dependence of single-crystal nanowire stability [5]. The $\vec{\xi}(\hat{n})$-construction (described below) was used in reference [52] which took a variational level-set approach to modeling both mean curvature flow and surface diffusion (though not dewetting, as there was no substrate in their systems) and in [53, 54], which use finite-element methods to model anisotropic dewetting. Both methods demonstrated simulations with regularized hard surface energy anisotropy, though neither placed emphasis on using $\gamma(\hat{n})$ derived from real physical systems. However references [53, 54] provide many examples using technologically relevant geometries, including long wires and edges.

In the absence of other potentials, surface self-diffusion is driven by gradients in weighted mean curvature (κ^γ), and the Mullins equation becomes

$$v_n = \nabla_s \cdot \left(D(\hat{n}) \frac{\nu \Omega^2}{k_B T} \nabla_s \kappa^\gamma \right)$$

, where $D(\hat{n}) = R^T(\hat{n}) D(\hat{n})_{\text{natural}} R(\hat{n})$ for D_{natural} of the form

$$\begin{matrix} d_1 & 0 & 0 \\ 0 & d_2 & 0 \\ 0 & 0 & 0 \end{matrix}$$

for an orthonormal basis $\{\hat{v}_1, \hat{v}_2, \hat{n}\}$ and appropriated change of basis matrix $R(\hat{n})$. In practice, we lump all the materials properties together and use an equation of the form $v_n = B(\hat{n}) \nabla_s^2 \kappa^\gamma$, where $B(\hat{n})$ incorporates anisotropic diffusivity. Taylor [12] defines κ^γ as "the rate of decrease of surface free energy with respect to volume swept out by the motion of the surface." There are several formulations of κ^γ; Taylor [12] gives an exhaustive review, and this topic is also discussed in more detail in chapter 1.2.1 (pg. 30). As a quick overview, the most straightforward method for obtaining

$\kappa^\gamma$is via the divergence of the Cahn-Hoffman vector, $\vec{\xi}(\hat{n})$ [11]. For isotropic system,

$$\kappa^\gamma = \nabla \cdot \vec{\xi}(\hat{n}) = \gamma \nabla \cdot \hat{n} = \gamma \cdot \kappa$$

. The Cahn-Hoffman vector, commonly denoted as $\vec{\xi}(\hat{n})$, is the gradient of the homogeneous extension of the surface energy function $\Gamma(A\hat{n}) = A\gamma(\hat{n})$ (see figure 1-5 for a graphical explanation and Ref. [58] for analogies to the chemical potential of binary alloys). For a given $\gamma(\hat{n})$, the curve $\vec{\xi}(\hat{n})$ plotted for all surface orientations $\hat{n}$, contains the Wulff shape with the addition of "ears" or "swallowtails" for the unstable orientations if there are any (i.e., the case of no edges on the Wulff shape), see figure 1-5 F). These ears are the orientation-space analog of a miscibility gap in alloys [58].

In simulations of systems with such unstable orientations, we use a Willmore regularization term [59] $-\varepsilon^2 \left(\kappa_{ss} + \frac{1}{2}\kappa^3\right)$. This regularization appears to have first been proposed in this context in Ref. [60] and is used in many studies of anisotropic surface evolution including Refs. [52–54]. Refs. [53], [61] provide particularly clear explanations of this regularization. The regularization is the analog to the square-gradient term in diffuse-interface theories (e.g., Cahn-Hilliard [62] and Allen-Cahn [63] functionals). Without regularization, surfaces with unstable orientations would develop facets or pyramids of arbitrary—and possibly infinitesimal—length scale (i.e., varifolds [64]). We find that the magnitude of the regularization coefficient sets the length scale of the faceting instability in our simulations, as expected. In many of our simulations, we construct the convex portion of $\vec{\xi}(\hat{n})$ from an observed Wulff shape, and we find that the exact functional form of the non-convex parts of $\vec{\xi}(\hat{n})$ (i.e., the "ears") plays a very negligible role in the results.

Our simulations are based on the level-set method, an Eulerian approach for simulating the evolution of surfaces, developed by Osher and Sethian [65]. In the level-set method, the surface being simulated is the zero iso-contour, or level-set, of a function $\phi(\vec{x})$ (usually chosen to be a signed distance function). Numerically, surface evolution is implemented by incrementally updating $\phi(\vec{x})$ by computing $\phi_t + \vec{v} \cdot \nabla\phi = 0$ for small time-steps (see figure 2-2). Level set methods are useful for studying morphological

evolution, particularly when topological changes occur, as the implicit representation of the evolving surface naturally handles such changes without special treatment. Another benefit is that geometric quantities, such as the normal vector and curvature are naturally defined in terms of derivatives of $\phi(\vec{x})$. Naïve implementations of LSM are plagued by issues of stability and volume conservation arising from distortions to $\phi(\vec{x})$, which cause it to locally deviate from a signed distance function. Redistancing methods, which are used in our simulations and discussed in detail below, combat this problem by approximately restoring $\phi(\vec{x})$ to a signed distance function without moving the zero level-set. A complimentary approach described by Zhao et al. [66] and first implemented by Smereka [41] removes the distortionary components of calculated quantities, by solving $\frac{\partial g}{\partial t} + \text{sign}(\phi)\frac{\nabla\phi}{|\nabla\phi|}\cdot\nabla g$, where g can be any calculated quantity such as interface velocity or κ^γ.

2.1   Methods

For an LSM simulation of surface self-diffusion driven by the gradient of weighted mean curvature, the governing equation for the time-evolution of $\phi(\vec{x},t)$ is $\phi_t = -(B(\hat{n})\nabla^2_s\kappa^\gamma)\nabla\phi$. As discussed above, $B(\hat{n})$ incorporates the effect of anisotropic diffusivity, while κ^γ incorporates the effect of anisotropic surface energy. However, simply numerically integrating this equation forward in time quickly leads to numerical instabilities and poor volume conservation caused by unphysical distortions to $\phi(\vec{x})$. These distortions arise from erroneous values for physical quantities calculated away from the interface. For example, only the calculated values of κ^γ on the $\phi(\vec{x}) = 0$ level-set have physical meaning, and the $\phi(\vec{x}) = 5$ level-set will tend to have much different values of κ^γ. If the differing values of κ^γ on other level-sets, $\phi(\vec{x},t) \neq 0$, are not corrected, these level-sets won't move in sync with the zero-level-set, and $\phi(\vec{x},t)$ will become distorted, negatively impacting the accuracy of the simulation. We utilize the correction method developed by Smereka [41] and Zhao et al. [66]. This approach replaces non-interfacial values of both κ^γ and surface velocity with values obtained by extending the physically meaningful interfacial values out into a band of points
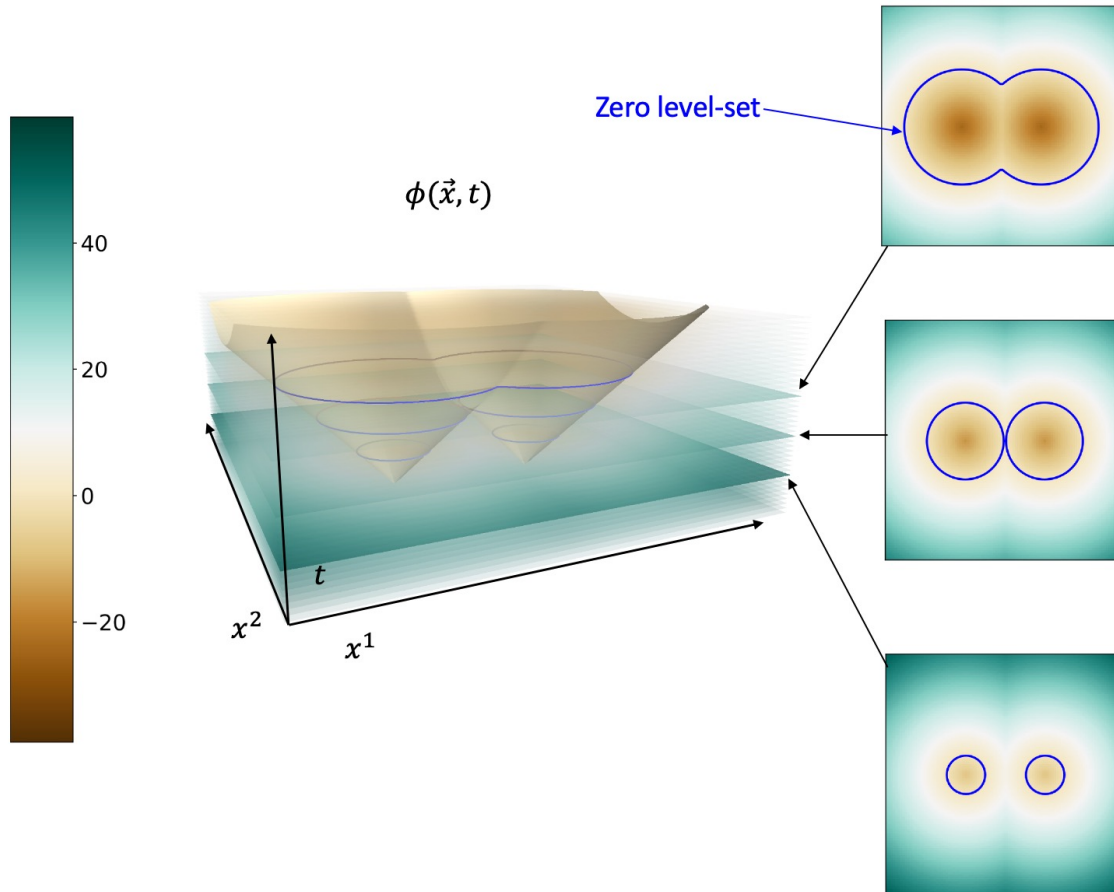
Figure 2-2: The level-set method implicitly encodes the location of interfaces (indicated by the blue outlines) in the values of a signed distance function, $\phi(\vec{x}, t)$. The magnitude of ϕ gives the distance from $\vec{x}$ to the closest interfacial point and the sign indicates whether $(\vec{x}, t)$ is inside ($\phi(\vec{x}, t) < 0$) or outside ($\phi(\vec{x}, t) > 0$) an interface. Here, two neighboring circles grow and merge (right, bottom to top). The evolution of ϕ is shown in the center of the figure, with the time axis oriented vertically. Three Individual time steps are highlighted for clarity.

encapsulating the interface. Smereka proposes a specific algorithm for performing this extension, but in our testing, we obtained better results using Adalsteinsson and Sethian's extension algorithm [67] based on the Fast Marching Method (FMM) [68]. In all of the work presented here, we used the implementation of Adalsteinsson and Sethian's algorithm found in the scikit-fmm Python package [69]. While these extension steps reduce unphysical distortions to $\phi(\vec{x})$, we also periodically redistance $\phi(\vec{x})$ to reset it to a signed distance function. In our testing, we have found that Sussman's redistancing method [70] usually yields the best results, as opposed to fast marching

based redistancing, and the results presented here are all from simulations making use of Sussman's method.

Numerically, we combine second order spatial derivatives with first order time stepping. Unfortunately, the central difference stencils used to compute $\nabla \phi (\vec{x})$, and thus $\hat{n}(\vec{x})$, yield the same normal vector for a flat surface and for a sawtooth surface with the same average orientation. During development, this led to non-physical oscillations developing on thermodynamically stable surfaces in some strongly anisotropic simulations. To combat this, we add a small term that goes as $\nabla^2 \phi(\vec{x})$ to κ^γ, calculated using 2nd order central differences. This term is similar to the curvature of the surface, so setting it too large will cause non-physical smoothing in anisotropic systems. We still found this smoothing operator to yield superior results to that used in Ref. [41], which is non-local in nature and thus introduced clearly non-physical distortions in our testing; Ref. [41] acknowledges the problems posed by these distortions. To increase computational performance, the size of the time step taken for each iteration is adaptively determined by $\Delta t = \alpha \Delta x / |S|_{max}$, where Δx is the grid spacing, $|S|_{\max}$ is the maximum of the absolute value the interface velocity, and α is a scaling factor less than 1. In practice, good results are often obtained with $\alpha \approx 0.01$. In 3D simulations, we found the performance cost of redistancing after every iteration was outweighed by the larger α it allowed us to use, while in two dimensions, such frequent redistancing was not always necessary. We found that α having too large a value led to volume drifting upward while setting it too small led to downward volume drift. Therefore, in most simulations, we adjust α after each time step by a very small amount, negatively proportional to the preceding time step's change in volume as a percentage of the initial volume. We find that α tends to trend downward during periods of topological change, such as pinch-off or ovulation, and then rebound when evolution is less extreme. If α climbs to too high a value, the simulation can become unstable, and if it becomes too low, the simulation takes too long to run, so we also set upper and lower bounds on α. In simulations in which α was made adaptive in this way, changes in volume over the course of the simulation were often less than a percent, and no simulations presented here had volume changes greater than a few

percent. For all volume measurements in this paper, we follow Sussman's use of a smoothed Heavyside function [70] to define the volume of a body characterized by a signed distance function.

As discussed above, surface energy anisotropy is incorporated into the simulations through the Cahn-Hoffman vector $\vec{\xi}(\hat{n})$. For crystalline systems, calculating $\vec{\xi}(\hat{n})$ can be computationally expensive, so values of $\vec{\xi}(\hat{n})$ for such systems were precomputed and accessed via a lookup table. For 3D simulations, these lookup tables were generated using the method proposed in Smith et al. [71]. In 2D, we found that lookup tables with 10^3 to 10^5 points were sufficiently dense while in 3D, we used lookup tables with up to about 3×10^6 points for materials for which very small facets needed to be resolved. In 2D simulations, $\vec{\xi}(\hat{n})$ could also be interpolated between lookup values by fitting a spline to the whole lookup table. For simulations which sought to match the behavior of a specific material, an initial $\gamma(\hat{n})$ was created using DFT-calculated surface energies from Tran, et al. [72]. Non-equilibrium orientations could be treated in a variety of ways to tune the hardness of the anisotropy. In each case, the final $\gamma(\hat{n})$ was then extended and numerically differentiated to yield $\vec{\xi}(\hat{n})$, as detailed in the background section. In other cases, arbitrary $\vec{\xi}(\hat{n})$ were created to explore how surface energy anisotropy affects dewetting-like processes more generally. For example, we conducted early simulations in a fictional simple cubic system with very high surface energy for all but {100} surfaces (i.e., the Wulff shape was a cube). For simulations of true dewetting (i.e. simulations in which the evolving material is in contact with a substrate), we initialize the simulation such that the zero level-set of $\phi(\vec{x})$ intersects the bounding box of the simulation domain along the $x = x_{\max}$ plane. This means that the contact patch between the film and the substrate is implicitly represented by the triple-line. An additional plane of ghost values is maintained below the physically meaningful simulation domain, which helps more accurately maintain the zero-flux boundary condition at the substrate. In the vicinity of the triple-line, these ghost values are set such that

$$\phi(x = x_{\max} + 1) = \phi(x = x_{\max}) + \frac{\partial \phi}{\partial x}|_{x=x_{\max}}.$$

This approach is similar to that used in Ref. [73] but is distinct in that we do not force the system to have a specific contact angle. To correctly model the evolution of the triple-line, we set

$$\kappa_\gamma = \nabla \cdot \vec{\xi}(\hat{n}) + (\hat{c}_\Gamma^\gamma \cdot \hat{n}_\Gamma + \gamma_{FS} - \gamma_{VS}) \frac{\sqrt{n_y^2 + n_z^2}}{\Delta x \sqrt{1 + n_x^2}}$$

for points in the $x = x_{\max}$-plane in the vicinity of the triple-line, where

$$\hat{c}_\Gamma^\gamma = \left(\vec{\xi}(\hat{n}) \cdot \hat{n}\right) \hat{c}_\Gamma - \left(\vec{\xi}(\hat{n}) \cdot \hat{c}_\Gamma\right) \hat{n},$$

$\hat{n}_\Gamma$ is the in-plane normal vector of the triple-line, and $\hat{c}_\Gamma$ is the unit vector defined to be tangent to the evolving surface and orthogonal to the triple-line while being oriented such that it points toward the substrate. This is similar to Ref. [54] which derives that $\hat{c}_\Gamma^\gamma \cdot \hat{n}_\Gamma + \gamma_{FS} - \gamma_{VS}$ is the first variation of total free energy of the system with respect to displacement of the triple-line. In our level-set formulation, however, the triple-line is represented implicitly, so we incorporate this quantity into κ^γ, rather than treating the evolution of the triple-line separately, as is done in Ref. [54]. The geometric factor $\frac{\sqrt{n_y^2 + n_z^2}}{\Delta x \sqrt{1 + n_x^2}}$ relates the variation of the triple-line to the variation of the surface element directly above the triple-line. We apply zero-flux boundary conditions at the triple-line and, in 3D simulations, also prohibit flux along the triple-line.

2.2 Results

2.2.1 Isotropic Systems

To benchmark our technique, we simulated edge retraction and the Rayleigh instability in isotropic systems and compared our results to both theory and previous simulations. For the retraction of an isotropic, semi-infinite film, the retracting rim should develop a smooth profile composed of a "hump" containing most of the dewetted material followed by oscillations in film height of decaying amplitude; the first

minimum is often referred to as the valley [23, 74] (figure 2-3). Eventually this valley touches down to contact the substrate, separating the rim from the rest of the film in a behavior called pinch-off . Starting with an edge like the one shown fig. 1a, the edge retraction distance initially increases rapidly but then is expected to evolve to approximately scale as $t^{2/5}$ [24, 74],. This behavior in isotropic systems, as well as the effect of contact angle, is explored in depth in [74] and our simulation results match theirs (figures 2-3 and 2-4). We also report scaling relations for the valley depth and rim height which were not explicitly discussed in Refs. [23, 74].
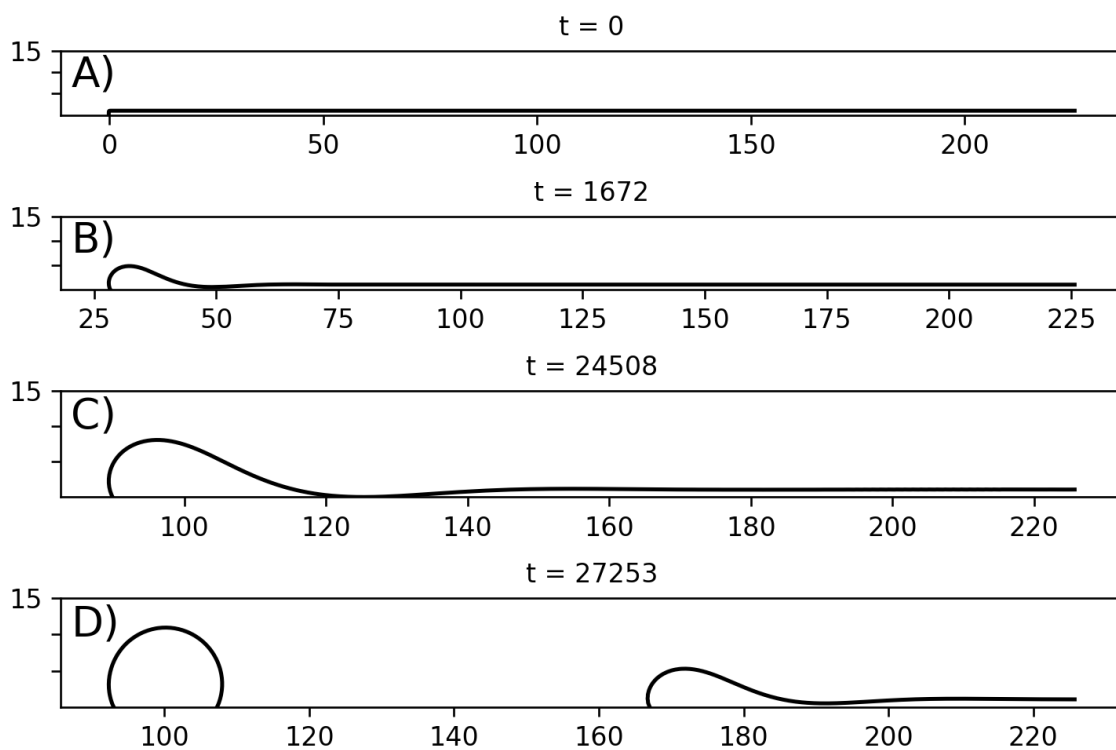
Figure 2-3: Rim profile for an isotropic film with 120° contact angle as it evolves toward and through pinch-off. C) closely matches the corresponding figure 4 c) in Wong et al. [21]. Their simulations used a point-tracking method with adaptive resolution and dimensionless units such that their film had an initial thickness of 1. The simulation shown in this figure was run with resolution such that the initial film thickness was 3.5. For comparison to [21], the spatial dimensions in this figure have been divided by 3.5 and the time values have been divided by 3.5^4 (following the same non-dimensionalization of [21]).

As a second test, we simulated Rayleigh-like instabilities [27] on free-standing cylinders with isotropic surface energy evolving by surface diffusion. It is well–
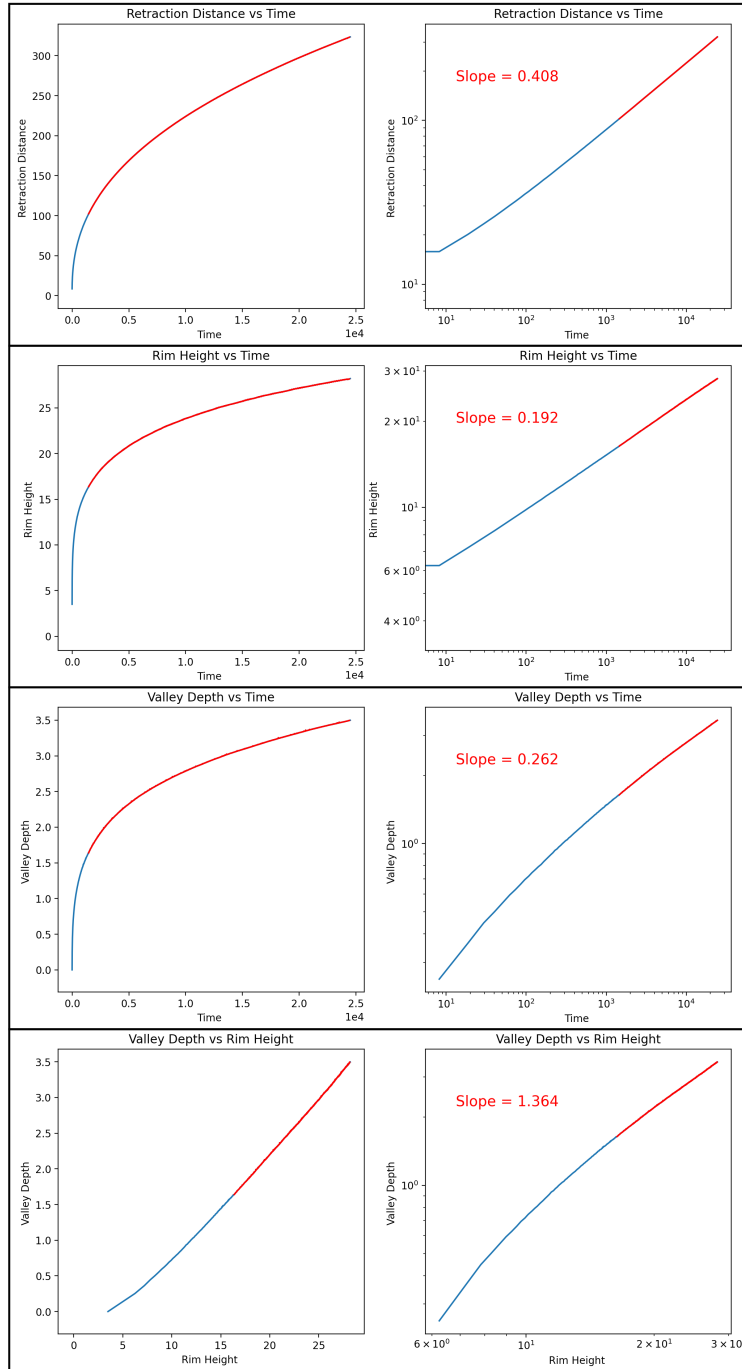
Figure 2-4: Selected scaling relations for an isotropic edge retraction simulation with 90° equilibrium contact angle (Units scaled to match [21]). Data are plotted from the beginning of the simulation until just before the first pinch-off event. Log-log plots are included to show how the behavior asymptotically approaches power law scaling. The annotated least-squares-fit slope on the log-log plots corresponds to the regions highlighted in red.

established that perturbations with wavelengths greater than the circumference of the wire will grow, eventually breaking the cylinder into spheres [30]. Our simulation technique reproduced the correct behavior, with small wavelength ($\lambda < 2\pi R_0$) perturbations on infinite cylinders (modeled as finite segments with periodic boundary conditions) decaying to zero amplitude and perturbations with supercritical wavelengths ($\lambda > 2\pi R_0$) growing and breaking up the wire, see figure 2-5 A) and 2-5 B). Perturbations close to $\lambda = 2\sqrt{2}\pi R_0$ grew the fastest, in correspondence to theory [30]. In figure 2-5 C), a long, finite wire was given an unstable perturbation. The ends of the wire began to retract and pinch off in the ovulatory manner predicted by Nichols [31], but the middle of the wire still decomposed in a Rayleigh-like fashion.
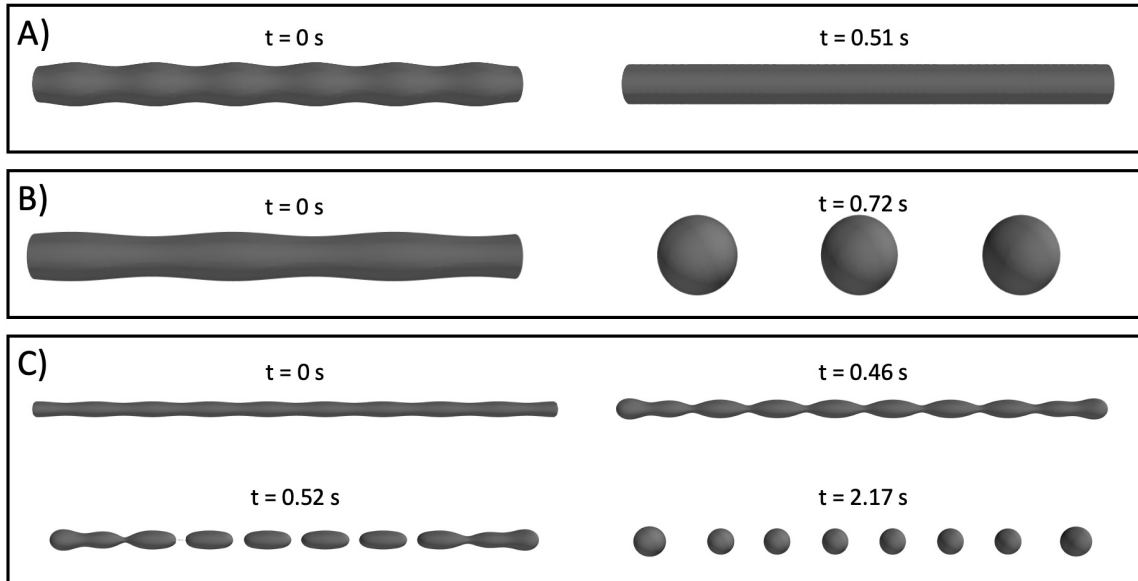
Figure 2-5: Recreating the isotropic Rayleigh-like instability. A) An infinite wire with an initial perturbation of large amplitude but subcritical wavelength which decays. B) An infinite wire with an initial perturbation of the same amplitude but supercritical wavelength. This wire breaks up into spherical particles through the Rayleigh-like instability. C) A long finite wire with a perturbation of super-critical wavelength. The ends of the wire retract while the body of the wire undergoes the Rayleigh-like instability. Initial wire diameter was set to 100 nm with $B = 6.2^{-21}$ m^5/J s.

As another demonstration of our technique, we simulated the growth of holes in isotropic films. As expected, these holes maintained their initially circular shape and developed a rim with a valley behind it, as in [22]. This behavior will be contrasted

with that of anisotropic films in the next section. It is worth noting that, in some simulations of very thin films, a numerical artifact, which we believe to be similar to that described in appendix B, caused the shapes of isotropic holes to become distorted at long times, highlighting that further work is still needed on developing smoothing operators.
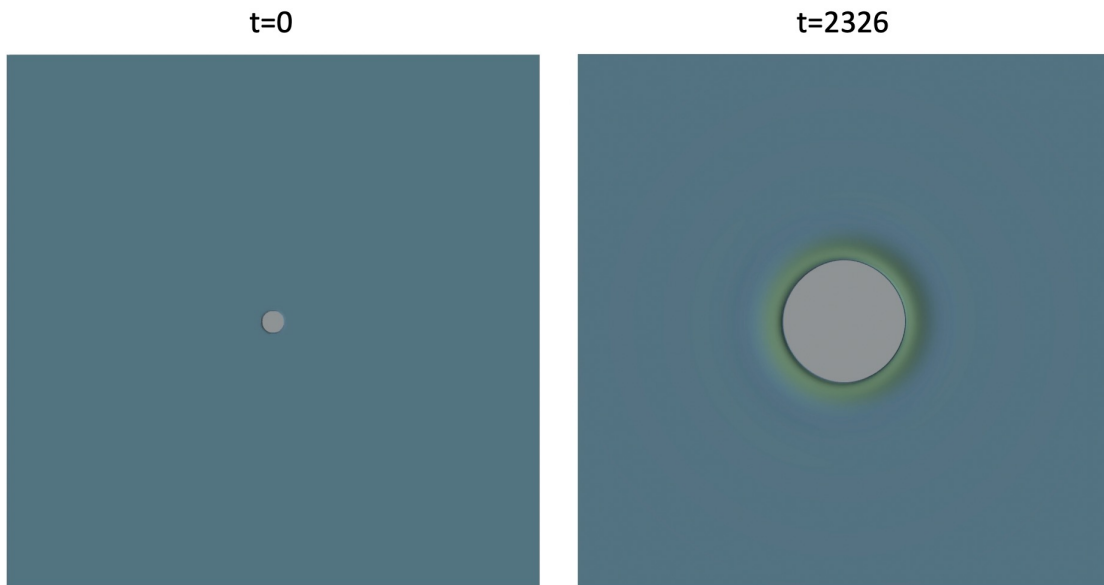
Figure 2-6: An initially circular hole in an isotropic film with $\gamma_{FS} - \gamma_{VS} = 0.6$ and $\gamma_{FV} = 1$. Coloration shows variation in height.

2.2.2 Effects of Anisotropy

We applied our algorithm to anisotropic systems with facets, starting with simulations of single-crystal Ni, for which there is a large body of experimental data. Such films can be lithographically patterned with extremely long, straight edges such that in some cases these experiments can be modeled in two spatial dimensions (e.g., ignoring the dimension that runs along the edge of the film). Of particular interest is the experimental observation that for Ni films on MgO, the edge orientations that retract most slowly are those for which the rim is bound by equilibrium facets along its length. These orientations are termed kinetically stable, because edges of other orientations

will eventually facet to become composed of such edges [25]. In Ni (100) films on MgO, retracting edges with kinetically stable orientations do not exhibit the formation of a valley [75], while retracting edges with kinetically stable orientations in (110) Ni films do exhibit valley formation and pinch-off [76]. This disparity exists despite both systems having equilibrium, low-index top facets, a criterion which past simulation work suggests should be sufficient to suppress valley formation [26]. To determine if our simulation technique captures the physical behavior of this system, we first created a surface energy function based on DFT-calculated values of the surface energy of Ni [72]. For low-index orientations, this function returned the DFT-calculated value and returned a linear combination of these energies for intermediate orientations, ignoring additional energy terms for corners and edges. The cusps corresponding to equilibrium orientations were very slightly rounded to prevent $\vec{\xi}(\hat{n})$ from being ill-defined at these orientations, similar to the smoothing proposed in Bonzel and Preuss [77]. The surface energy of the (110) facet was also reduced by less than 1%, from $2.29\,\mathrm{J/m^2}$ to $2.28\,\mathrm{J/m^2}$ (though these quantities are effectively non-dimensional, as units are not used internally in the simulation), to ensure that this very small facet wasn't washed out by the rounding of the cusps. Viewed along the appropriate cross-section, this function is shown in figure 2-7, which shows that despite the absence of an evident (011) cusp in $\gamma(\hat{n})$, $\vec{\xi}(\hat{n})$ still has an obvious facet. The ability of our simulation method to accommodate more complex surface anisotropy such as this is one of its core strengths. Following the lead of Jiang et al. [78], we introduced a Willmore regularization term [59], $-\varepsilon^2\left(\kappa_{ss} + \frac{1}{2}\kappa^3\right)$, to our chemical potential to give the faceting instability finite wavelength, as discussed above. In this case, ε was simply set to 1.

We then used this $\gamma(\hat{n})$ to conduct 2D edge-retraction simulations in 2D free-standing wires, to isolate the effects of surface energy and diffusivity from any confounding effects of triple-line dynamics. Figure 2-8 shows the results of several such simulations, with the wires cut along their long axis of symmetry for visual clarity. To test our algorithm for anisotropic diffusivity, we assigned a diffusivity value to each facet. For non-equilibrium orientations, we treated the surface as being micro-faceted

65
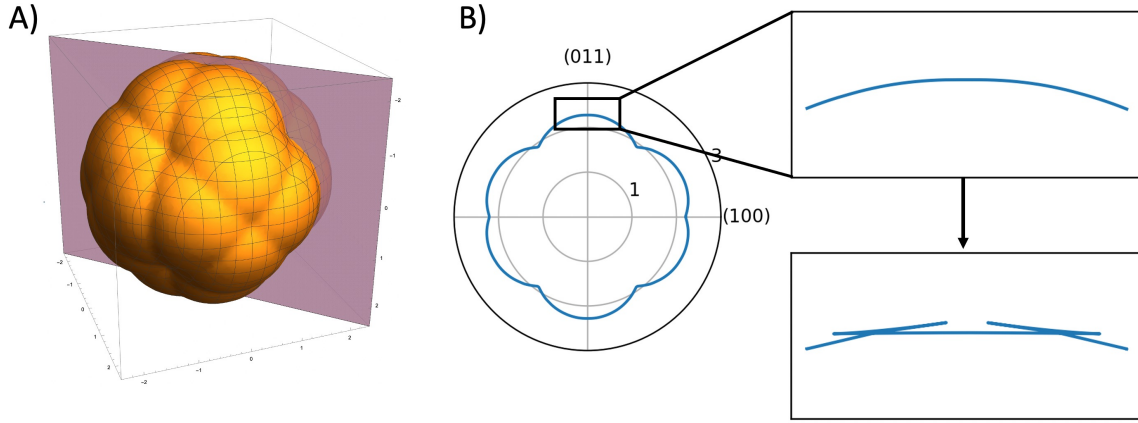
Figure 2-7: A) The full surface energy function $\gamma(\hat{n})$ derived from DFT values and B) the cross-section of this function used to simulate Ni edge retraction. The insets to the right are a close-up of $\gamma(\hat{n})$ and $\vec{\xi}(\hat{n})$ in the vicinity of the (011) facet. Values are in units of J/m^2.

and found the diffusivity through a weighted inverse sum, analogous to adding conductance in series. As in experiments, valley formation occurs in the simulations of (110) films and not in those of (100) films, even when diffusivity is isotropic. However, by manipulating the diffusivity across the (110) facet, we found that it is a key parameter for controlling the relative size of the valley that forms in (110) films. When the diffusivity across this facet is large, a deep, faceted valley develops. When this diffusivity is low, valley formation is suppressed. Figure 2-8 A-B) contrasts these two scenarios. Experimentally, valley formation is not observed in Ni (100) films [25], and it is also absent in our simulations. We attribute this to the much deeper cusp in $\gamma(\hat{n})$ associated with the (100) facets, in comparison with the (110) facets. Figures 2-8 A) and 2-8 D) demonstrate that the experimentally observed behavior of both (110) and (100) films can be accurately simulated using a single set of surface energy and diffusivity functions.

In three dimensions, the range of phenomenology to explore is even richer, and the impact of anisotropy is even more profound. As a simple example, a simulation of an unperturbed Ni wire undergoing repeated ovulation demonstrates that our 3D code retains the ability to handle topological changes naturally, see figure 2-9. $\vec{\xi}(\hat{n})$ was
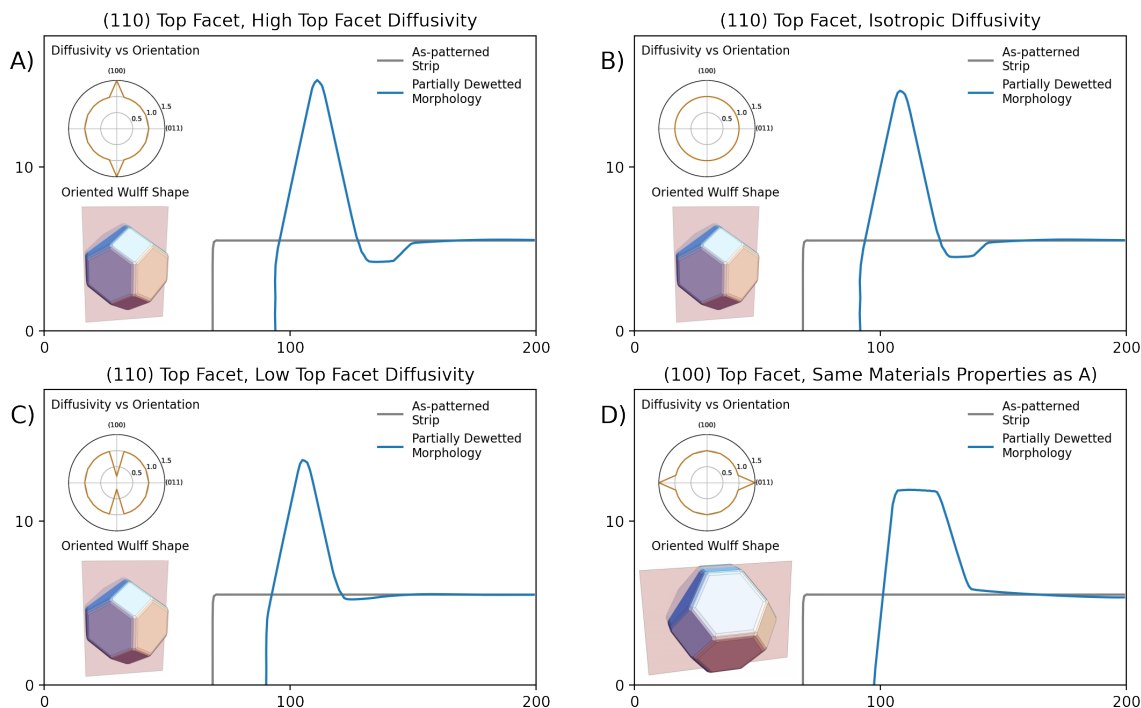
Figure 2-8: 2D simulations of retracting film edges. Note very different x and y scales. Full wires were 360 units long to start and 11 units tall (only the top half of the wires is shown because the simulation is symmetric in this direction). A) Most closely matches experiments (see 3), and D) shows that experimental behavior (suppressed valley formation) in (100) films can be reproduced using the same parameters as A). The upper-left corner of each subplot shows the diffusivity function used in the simulation, while the lower-left corner shows how the orientation of the strip corresponds to the equilibrium Wulff-shape (based on the function shown in Fig. 6 A-C)).

again based on the same DFT values as above, although only the three lowest energy families of facets—(001), (011), and (111)—were used and they were configured to have small spinodes at all corners and edges.

Simulating hole growth in a material with Ni–like surface energy anisotropy yields profoundly different behavior compared to that seen in isotropic films. In figure 2-10, a film with a (100) top surface is initialized with a circular hole. However, this hole quickly grows to its kinetic Wulff shape [6, 79] which in this case is bound by long edges with [110] in-plane normals and truncated corners with [100] in-plane normals. As the hole continues to grow, a corner instability develops [7], yielding behavior with striking resemblance to experimental observations. To reduce the size

67

of the simulation domain, only one quadrant of the film was simulated, and mirror boundary conditions were used. This simulation was conducted using the same $\vec{\xi}(\hat{n})$ as the simulation in figure 2-9, with mirror boundary conditions used on the right side of the wire. The film-substrate interfacial energy was set to $0.6\,\mathrm{J/m^2}$, to roughly correspond to the partially non-wetting behavior seen in past studies of Ni (100) films on MgO. This simulation was repeated with anisotropic diffusivity, see figure 2-11, which scaled as the exponential of surface energy for low–index planes and was calculated using a weighted inverse sum for other orientations, as described above. This simulation shows qualitatively similar behavior, to the simulation with isotropic diffusivity, though anisotropic diffusivity is clearly sharpening the tip of the dendrite. Finally, we simulated the growth of a hole with isotropic surface energy and the same anisotropic diffusivity as above, see figure 2-12. This simulation was carried out using a larger grid with no mirror boundary through the center of the hole to eliminate any directional biasing introduced by the boundary conditions. Still, the resulting behavior seems nearly dendritic in character, and simulations of this behavior on larger domains would be very interesting.
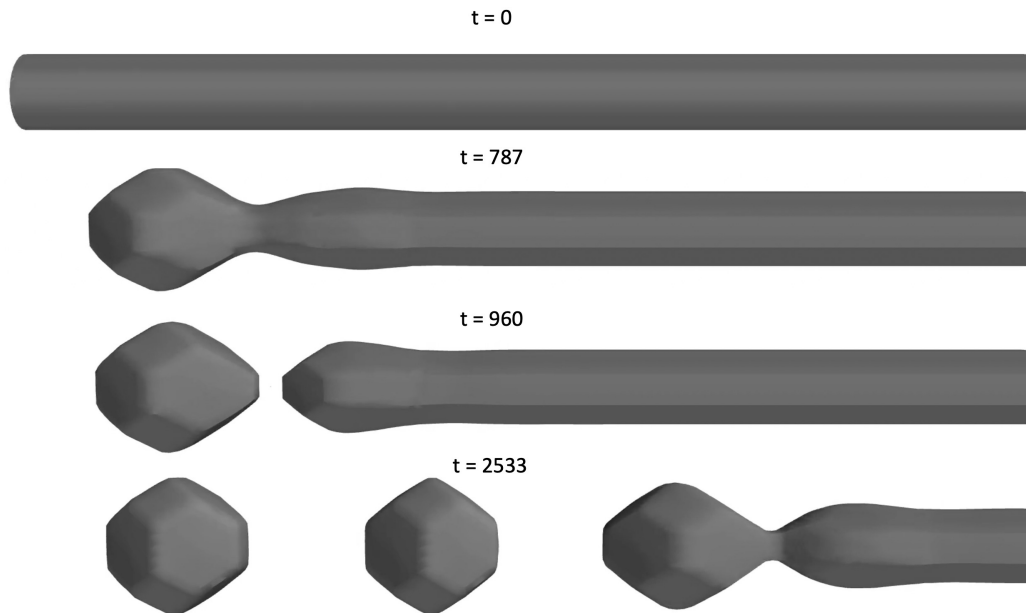
Figure 2-9: Repeated ovulation of an Ni wire bound by (100) and (110) facets along its length.
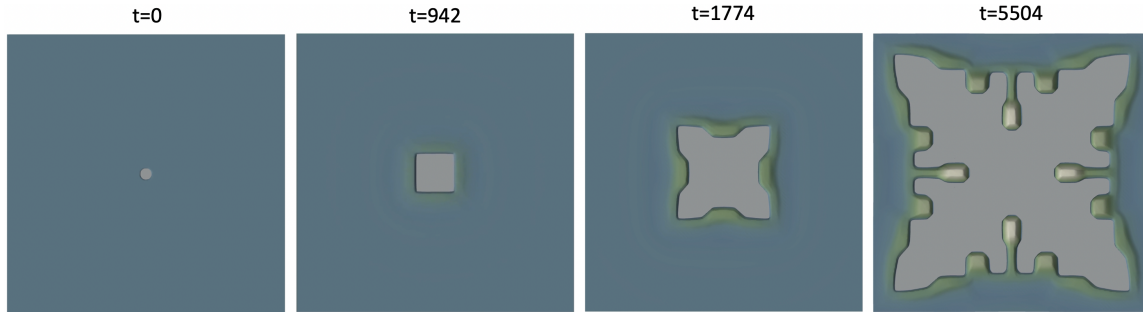
Figure 2-10: An initially circular hole in a simulated Ni film with anisotropic $\gamma(\hat{n})$ and isotropic diffusivity. The corners of the hole begin to show dendritic morphology. Coloration shows variation in height. Mirror boundary conditions were used with reflections occurring through the middle of the hole. The full video is available in Supplemental Materials (hole_1.mp4).
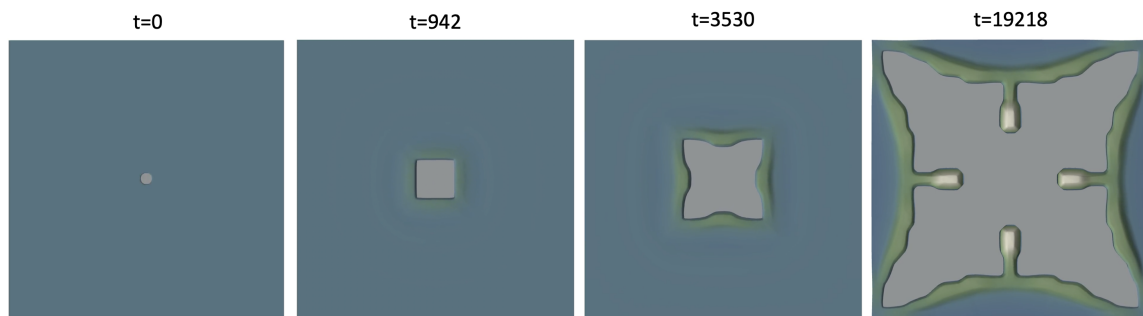
Figure 2-11: An initially circular hole in a simulated Ni film with anisotropic $\gamma(\hat{n})$ and diffusivity. The corners of the hole begin to show dendritic morphology. Coloration shows variation in height. Mirror boundary conditions were used with reflections occurring through the middle of the hole. The full video is available in Supplemental Materials (hole_2.mp4).
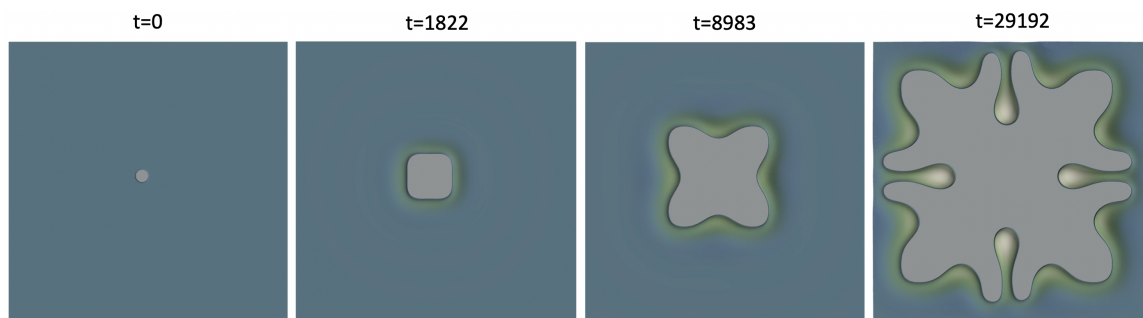
Figure 2-12: An initially circular hole in a simulated film with isotropic $\gamma(\hat{n})$ and anisotropic diffusivity. The corners of the hole begins to show strange dendrite-like morphology. Coloration shows variation in height. Mirror boundary conditions were used with reflections occurring only at the edges of the displayed domain, not through the center of the hole as in the two figures above. The full video is available in Supplemental Materials (hole_3.mp4).

69

2.3 Computational Performance

Our implementation of this simulation method was written in the Julia programming language [80] which enables high performance code that is easy to write and read. The most computationally intensive parts of our code have been parallelized, and for the size of simulations demonstrated here, overall performance saturates when 3 threads are used in 2D and 6 threads are used in 3D. This is because the fast marching package we use, scikit-fmm, is single-threaded and calls to its fast marching and velocity extension functions become rate limiting for the simulation. We have mitigated this issue through the use of scikit-fmm's ability to only update points in a narrow band around the $\phi = 0$ level-set. We run our code on a workstation computer with a 2019-era AMD Threadripper CPU. The 2D simulations shown here take tens of hours to complete while the 3D simulations take can take several days. Code that runs faster would allow for higher resolution simulations within reasonable times. The resolution of the simulation limits the size of facets that can be resolved, and simulations with resolution that is too low suffer from poor volume conservation and missing details. A potential approach for increasing performance, and thus practical resolution, is discussed below.

2.4 Future Work

The code developed for this work was designed with a high degree of modularity, with an eye toward future improvements to physical accuracy and performance. As with any simulation method, the degree to which this technique reproduces physical reality is limited by the accuracy of the materials properties used as input. The relatively simplistic models of $\vec{\xi}(\hat{n})$ and $D(\hat{n})$ used in this paper were evidently sufficiently accurate to yield simulation results that recover experimental observations, but more accurate models for $\vec{\xi}(\hat{n})$ and $D(\hat{n})$ will certainly lead to even more accurate simulation results. From a performance standpoint, this code has been optimized to the point where its calls to the scikit-fmm package are now the rate limiting steps. We

think it should be possible to write a new implementation of the velocity extension algorithm which allows multiple quantities (in this case, κ^γ and v_n) to be extended without repeating redundant fast marching computations. We anticipate that this could yield a roughly 3x boost in performance, perhaps more if the implementation is also written in Julia to eliminate the overhead of calls to Python-wrapped C-code. Another area of future work could be to use an adaptive simulation grid which locally increases the resolution of the simulation in regions of high curvature. We also believe there are likely better ways to suppress the formation of non-physical sawtooth surfaces than penalizing $\nabla^2 \phi(\vec{x})$, as we did here. Still, as demonstrated, this code already has sufficient performance and accuracy to probe many physical phenomena of interest in reasonable amounts of time.

2.5 Conclusions

The $\vec{\xi}(\hat{n})$ level-set method of simulating morphological evolution proposed and demonstrated above is capable of reproducing experimental results with a high degree of fidelity. This method is capable of handling surface energy functions with hard anisotropy in conjunction with anisotropic surface self-diffusivity. Critically, this method overcomes the numerical stability and volume conservation issues which are common in level-set simulations of high-order PDEs. The method uses $\nabla \cdot \vec{\xi}(\hat{n})$ to compute the weighted mean curvature which combines surface tension with geometry to produce the position-dependent surface-potential. The normal velocity $\vec{v}(\vec{x}, t)$ is computed from the surface Laplacian of weighted mean curvature. Incorporation of redistancing and velocity extension algorithms produces enhanced numerical stability and allows our method to achieve volume conservation within a few percent while maintaining the benefits of the level-set method, such as natural handling of topological changes. We have shown that our method matches known behavior for the isotropic Rayleigh instability and edge retraction. In addition, it matches behavior observed in experiments in which anisotropy plays a central role, including the orientational dependence of valley formation ahead of retracting edges and the

development of faceted holes that undergo a corner instability. Our software for simulating morphological evolution caused by anisotropic surface diffusion is available on Github. This software will enable new research on solid-state dewetting, including advances in understanding that will aid in the use of solid state dewetting to obtain specific morphologies useful in micro- and nano-scale devices.

Chapter 3

The Effects of Ambient Conditions on Edge Retraction in Nickel (110) Films

* The work in this chapter was conducted in collaboration with Yoon Ah Shin and Baoming Wang. It will form the basis of an upcoming paper and is also discussed in Yoon Ah's thesis [81].

3.1 Introduction

As discussed in chapter 1.8.2, ambient conditions can have a profound impact on dewetting phenomenology. In past work the impact of oxygen partial pressure on dewetting Ni films was explored, by controlling the flow rate of a hydrogen-based reducing gas to control P_{O_2} [36]. In this chapter, we present new experimental findings which show that the use of carbon monixide (CO) as a reducing gas also has a profound impact on the dewetting behavior of Ni (110) films and use the simulation technique introduced in chapter 2 to explain the observed differences.

3.2 Experimental Observations

As discussed in chapter 2, one dewetting phenomenon which has defied understanding is valley formation in strongly anisotropic materials. In past work, our group has long

observed that retracting edges in Ni (100) films do not exhibit valley formation, while Ni (110) films form deep valleys which eventually touch down to the substrate [4, 6]. An early success of our modeling work was reproducing this result and showing that the diffusivity of the top facet had a large impact on the rate of valley deepening. This was a powerful validation of our simulation method, especially considering that previous modeling work had concluded that valley formation was only possible in films for which there was no stable top facet [26]. The ability to tweak materials properties such as diffusivity is one of the most computational approaches' greatest strengths and is usually very difficult to achieve experimentally. As discussed in chapter 1, however, changing the ambient conditions used during annealing is one way in which the properties of the system can be significantly and reproducibly altered.

3.2.1 Experimental Apparatus

As part of a separate effort to understand the effects of ambient conditions on natural hole formation, we designed and constructed an experimental setup which allows us to safely use CO-based reducing gas (10% CO, 90% N_2). This setup consists of an tube furnace located inside a normally-closed fume hood. This furnace uses our standard quartz glass tubes with a 20.5mm inner diameter. Reducing gas is flowed from a small CO tank which is also kept inside the fume hood. To prevent users from having to open the fume hood during furnace operation, gas flow rate is controlled by a digital mass flow controller, which has the added benefit of using a normall-closed solenoid. This means that a loss of power to the lab, which could also take the fume hood offline, would cause gas flow to stop immediately. Additional safety measures include custom fabricated aluminum hard lines connecting the gas tank to the furnace, multiple CO detectors located throughout the lab, and a wireless emergency shutoff which can stop gas flow from anywhere in the lab. One downside of this setup is the small internal dimensions of the fume hood. Early experiments were plagued by mysterious contamination which was eventually attributed to rubber O-rings used in our gas fittings being overheated because they were too close to the furnace. The

issue was resolved by carefully reorganizing the individual components to allow for more space between the fittings and the furnace.

3.2.2 Experimental Procedures

To study the effects of ambient conditions on system properties, multiple 75nm-thick Ni (110) films were deposited on 1cm^2 MgO substrates. For more details on our deposition conditions, see chapter 1.5 (pg. 38). These films were then patterned with large (hundreds of microns in length and width) rectangular patches using photolithography. A subset of these samples were then annealed at 950° C in our standard H$_2$-based annealing ambient (5% H$_2$, 95% N$_2$, flowed at 2300 sccm), while the other samples were annealed at the same temperature using the CO-based reducing gas discussed above, also flowing at 2300 sccm. The edge retraction, valley formation, and pinch-off behavior of edges retracting along [1$\bar{1}$0] directions were then then carefully observed and quantified using HRSEM, TEM, and AFM. The [1$\bar{1}$0] direction was chosen because it is a kinetically stable orientation in both ambient conditions. Additionally, areas of the film were patterned with smaller patches designed to dewet into particles or wires from which the relevant cross-section of the systems' Winterbottom shape could be extracted.

3.2.3 Experimental Results

These experiments yielded a wealth of data, though the main experimental findings can be summarized by a few images, shown below. As shown in figure 3-1, after 1 hour of annealing, the films have retracted a significant distance ($\sim$ 40 times initial film thickness) along their [1$\bar{1}$0] direction, with the H$_2$-ambient film having retracted slightly further. However, although the total degree of dewetting is comparable, the morphology of the two films are very different. Most noticeably, the H$_2$-ambient film has formed a deep valley ahead of the rim while the CO-ambient film doesn't exhibit any noticeable valley formation. This morphological difference manifests itself

as a fundamental difference in the dewetting behavior of the two systems, with the H_2-ambient films eventually undergoing pinch-off as the valley touches down to the substrate, as shown in figure 3-2. Figures 3-3 and 3-4 show TEM cross-sections of retracting H_2-ambient and CO-ambient edges, respectively. Visible planes are labeled with their measured orientations, though the higher-index labels in 3-3 likely correspond to lower-index planes with steps in them. Without the exaggerated vertical scale of the AFM images, valley formation is far more subtle.

Though this disparity in valley formation is the most obvious result from this set of experiments, several other observations stand out. Perhaps most strikingly, the leading side of the rim, i.e. the side that connects the top of the rim to the bulk film or valley, is composed of a single, elongated 120-type facet. It is also apparent that the top facet of the CO-ambient rim is much larger than its H_2-ambient counterpart. Finally, we also observe that the substrate is more deformed in the vicinity of the triple-line in H_2-ambient samples than in CO-ambient samples. We believe that this interaction indicates that the MgO substrate has relatively high mobility under these annealing conditions and that the deformation is an energetic accomodation, in line with Rachel Zucker's work on the double-Winterbottom construction [82].
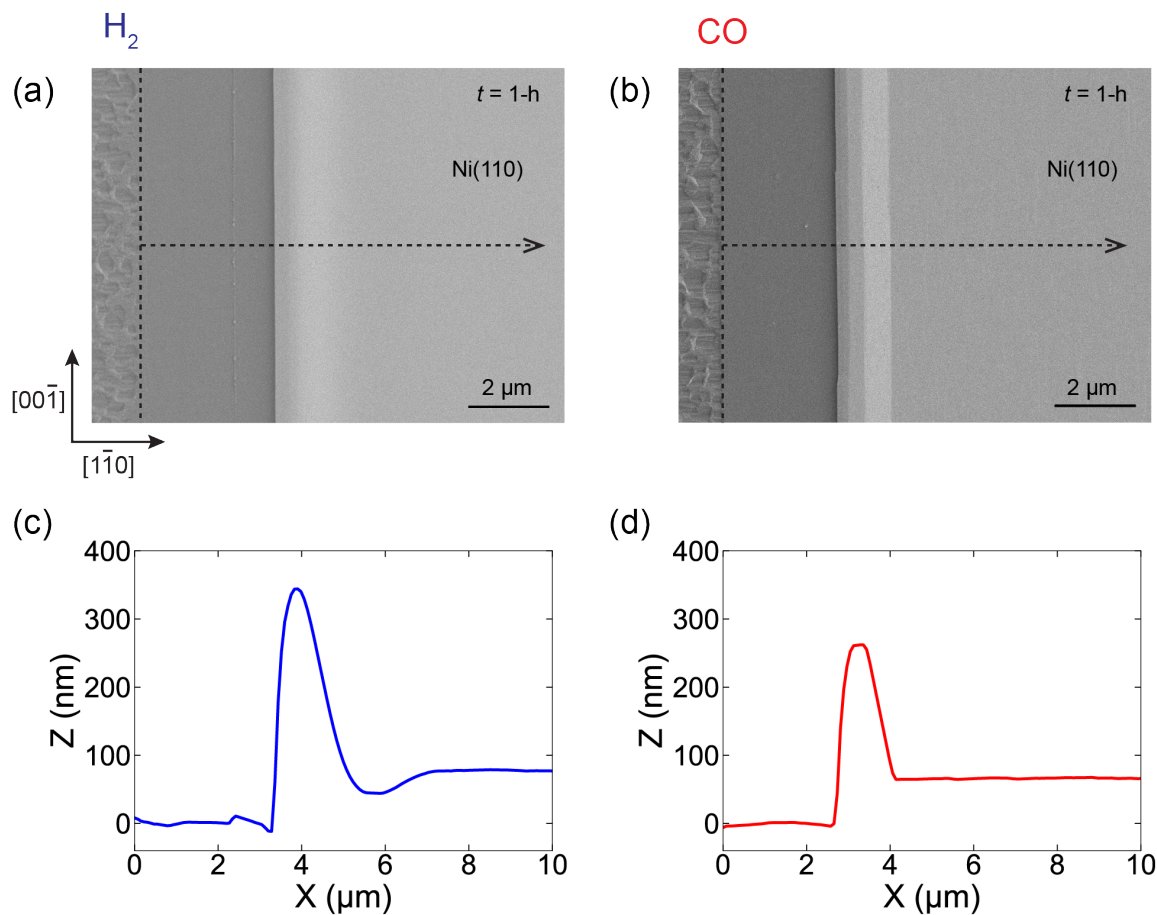
Figure 3-1: Effects of annealing ambient (H_2 versus CO) on edge retraction and pinch-off in 75-nm-thick Ni(110) films on MgO. (a),(b) Top-view SEM images of retracting edges, after a 1-h anneal at 950°C (a) in a reducing gas (5% H_2 - 95% N_2) flowing at 2310 sccm, and (b) in a reducing gas (10% CO - 90% N_2) flowing at 2310 sccm. (c),(d) AFM height profiles measured along the dashed arrows in (a) and (b) in each annealing ambient.
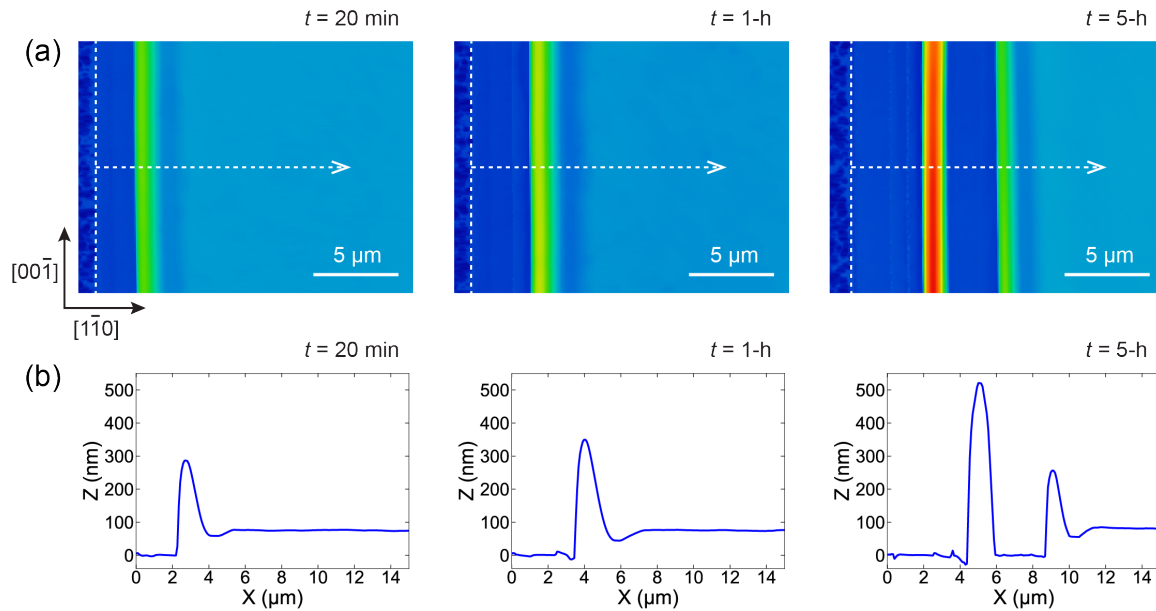
Figure 3-2: Valley deepening and pinch-off during retraction of a patterned edge in Ni(110) film on MgO in H_2 ambient. (a) Time series AFM images of a retracting edge along the $[1\bar{1}0]$ direction in a 75-nm-thick Ni(110) film on MgO. The annealing time is indicated at the top of each image. The annealing temperature was 950°C and the flow rate of the reducing gas (5% H_2 - 95% N_2) was 2310 sccm. The in-plane crystallographic orientation of the Ni(110) film is indicated at the bottom left corner. (b) AFM height profiles measured along the dashed arrows indicated in the AFM images in (a). The vertical dashed line in each image in (a) indicates the initial position of the patterned edge.
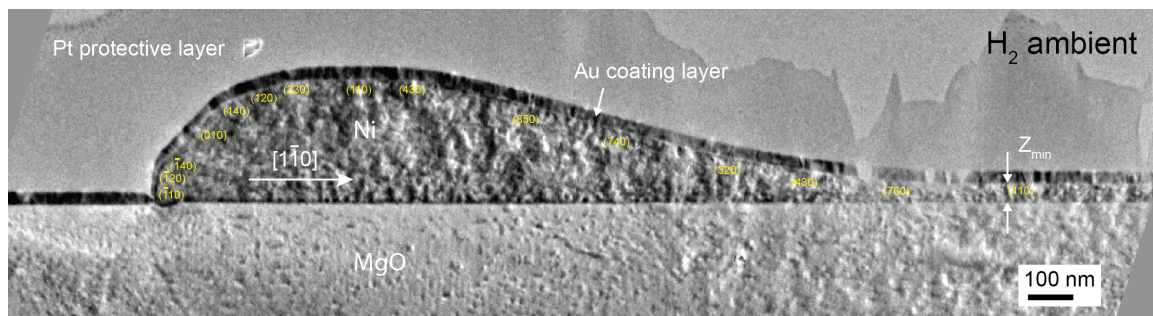
Figure 3-3: Cross-sectional TEM image showing the rim shape of a retracting edge in a 75-nm-thick Ni(110) film on MgO, after a 1-h anneal at 950°C in the H_2 ambient. Facets that appear on the rim are: $(\bar{1}10)$, $(\bar{1}20)$, $(\bar{1}40)$, (010), (140), (120), (230), (110), (430), (850), (740), (320), (430), (760), and (110) at the valley. The height at the valley Z_{min} is 45 nm.

Figure 3-4: Cross-sectional TEM image showing the rim shape of a retracting edge in a 75-nm-thick Ni(110) film on MgO, after a 1-h anneal at 950°C in the CO ambient. Facets that appear on the rim are: $(\bar{2}10)$, $(\bar{1}20)$, $(\bar{1}30)$, (130), (120), (110), (210). Valley did not form in the CO ambient.

3.3   Computational Study

The experimental results presented above show that films annealed in these two different ambients exhibit profoundly different dewetting behavior. On it's own, this is a very interesting result, the implications of which are discussed below, however, it is difficult to gain mechanistic insight from these experimental results alone. To better understand how these two sets of ambient conditions lead to different dewetting behavior, we turned to the modeling technique described in chapter 2.

3.3.1   Defining $\vec{\xi}(\hat{n})$

Before running any simulations, an appropriate $\vec{\xi}(\hat{n})$ needed to be constructed for each ambient condition. To this end, an equilibrated particle, from the H_2-ambient, and wire, from the CO-ambient, were cross-sectioned using FIB and subsequently imaged in a TEM. The wire was oriented such that it's length ran in the out-of-plane direction of figures 3-1, 3-2, 3-3, and 3-4, and both cross-sections were taken in the plane of those images. These cross-sections were then fit to a Wulff shape constrained to respect the crystallographic symmetry of Ni. Relative surface free energy densities were extracted from these fits, with the highest energy plane assigned a value of 1. The relative interfacial energy $\sigma = \frac{\gamma_{VS} - \gamma_{PS}}{\gamma_{PV}}$ can also be extracted from these fits. In principle, it should be trivial to measure the relative surface energies of different equilibrium facets by simply reverse-engineering the Wulff construction. However, this assumes a perfectly symmetrical cross-section with a clearly defined center. In practice, no cross-section is perfect, and fitting was done by generating a fully faceted Wulff shape in Wolfram Mathematica, overlaying this shape onto the TEM cross-section in Adobe Photoshop, adjusting the values of γ used to generate the Wulff shape, and repeating the process until unable to achieve a better fit. The best fits achieved are shown in figures 3-6 and 3-5, and the numerical values of the fits are summarized in table 3.1.

Measured Quantity	H$_2$-Ambient	CO-Ambient
γ_{110}	1.0	0.956938
γ_{120}	0.975806	0.964912
γ_{140}	not present	0.977671
γ_{010}	0.951613	1.0
σ	~ 0.4	~ -0.2

Table 3.1: Measured Relative Surface Free Energy Densities of Ni Films in Different Ambients
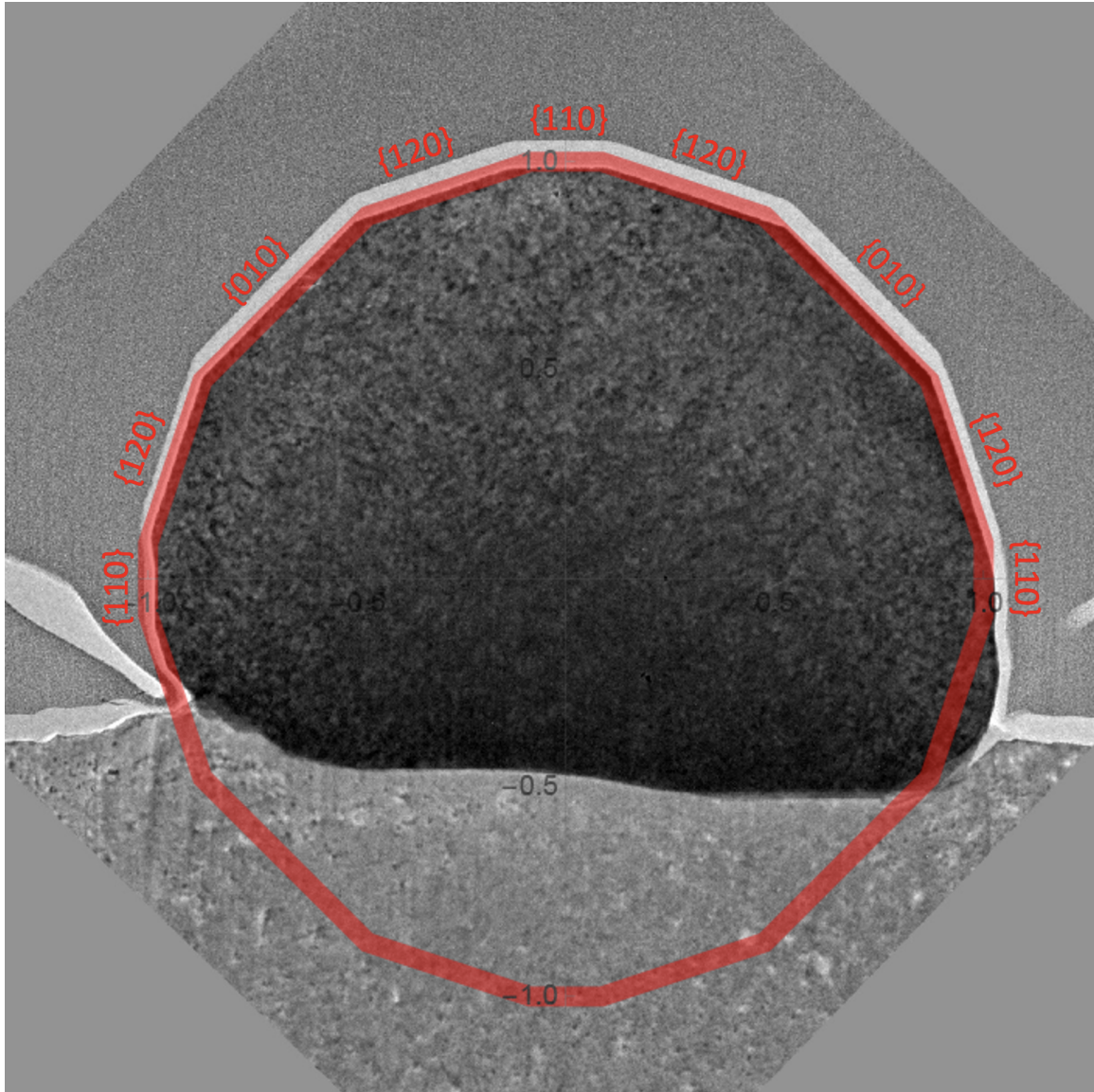
Figure 3-5: Cross-section of equilibrated Ni particle annealed in H$_2$-based ambient with fitted Wulff shape. $\gamma_{110} = 1.0$, $\gamma_{120} = 0.975806$, $\gamma_{010} = 0.951613$.
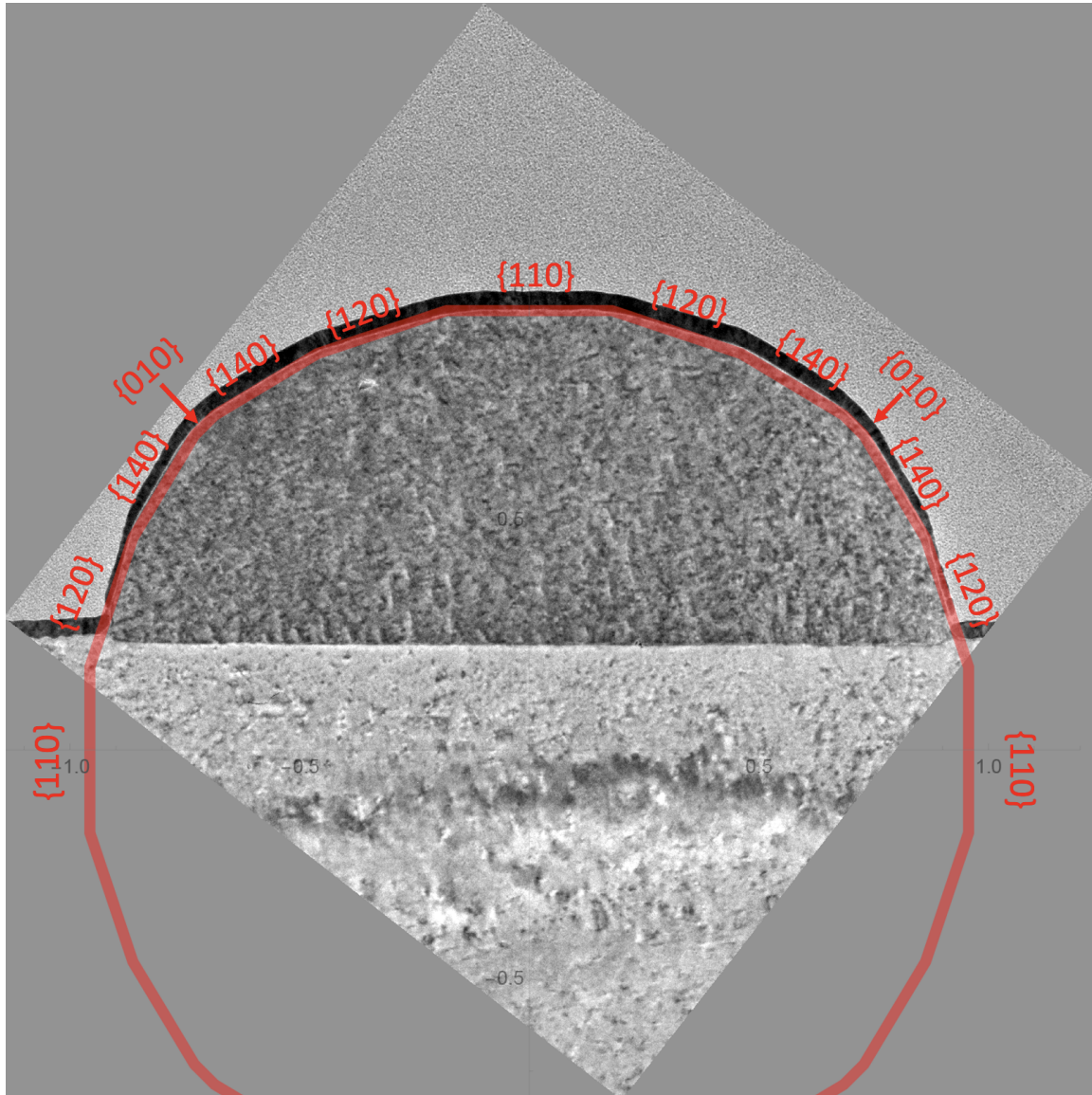
Figure 3-6: Cross-section of equilibrated Ni particle annealed in CO-based ambient with fitted Wulff shape. $\gamma_{110} = 0.956938$, $\gamma_{120} = 0.964912$, $\gamma_{010} = 1.0$, $\gamma_{140} = 0.977671$.

3.3.2 Simulating Edge Retraction

Using these measurements, a $\vec{\xi}(\hat{n})$ was constructed for both ambients and used to simulate edge retraction in two dimensions. The relative interfacial energy σ was set to 0.4 for the H$_2$-ambient films and -0.2 for the CO-ambient films. An additional simulation was run pairing the CO-ambient $\vec{\xi}(\hat{n})$ with the H$_2$-ambient σ to separate the effect of a higher σ, i.e. a higher driving force for dewetting, from the contributions of the very different $\vec{\xi}(\hat{n})$. For all three simulations, all parameters outside the energies used to construct $\vec{\xi}(\hat{n})$ were kept the same. In particular the radius of curvature of corners on $\vec{\xi}(\hat{n})$ was set to 0.1 and the $\nabla^2\phi$ smoothing coefficient was set to 0.2.

The results of these simulations are summarized in figures 3-7 and 3-8 which present the same data with AFM- and TEM-like scalings, respectively. In both figures, panels A) and B) show the results of the H$_2$- and CO-ambient conditions, respectively, while panel C) shows the output of the hybrid condition simulation. The two simulaations designed to match experimental conditions do in fact reproduce experimental behavior, with deep valley formation exhibited by the H$_2$-ambient film and no valley formation shown by the CO-ambient film. The hybrid film shows very minimal valley formation, suggesting that the high driving force for dewetting and larger effective contact angle make a much smaller contribution to valley formation than the Wulff shape itself. Another experimental observation, that the top facet of the retracting rim is proportionally larger than that of the equilibrium particle, is also reflected in these simulations. Furthermore, the experimental observation that the leading side of the rim is composed of a single, elongated facet is also born out by the simulations.
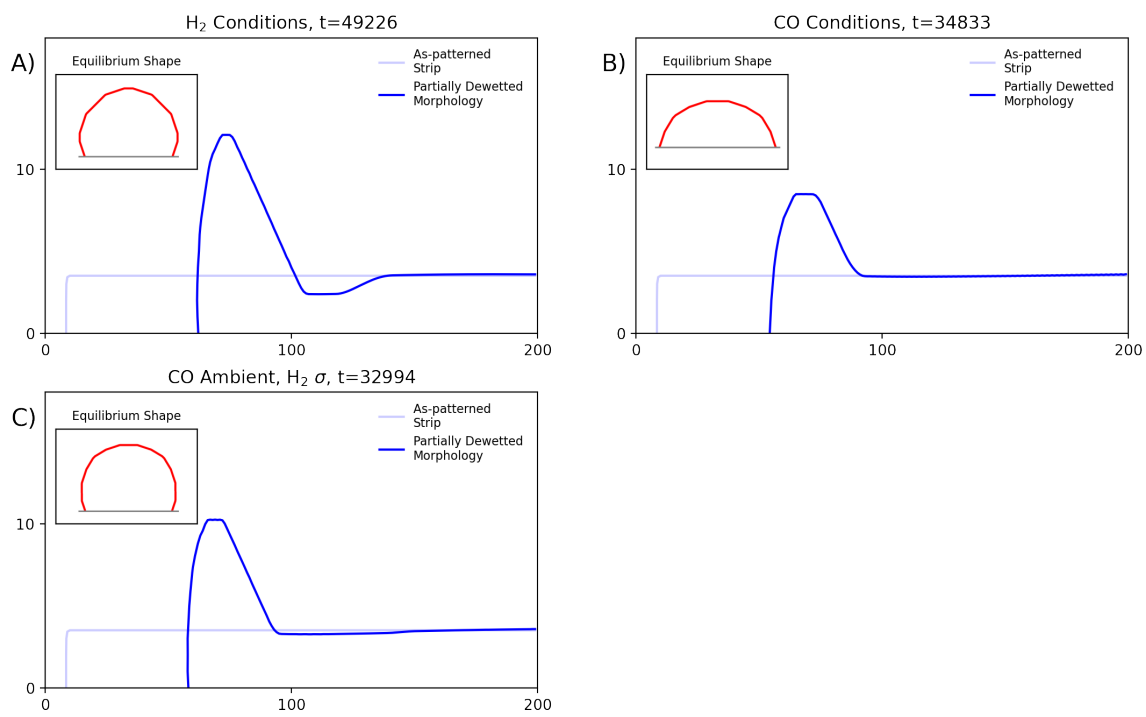
Figure 3-7: Summary of simulation results with equal axis scaling (comparable to AFM images). C) shows a fictitious system with the Wulff shape of the CO–based ambient and the effective contact angle of the H$_2$–based ambient. This shows that it is not effective contact angle which primarily drives valley formation.
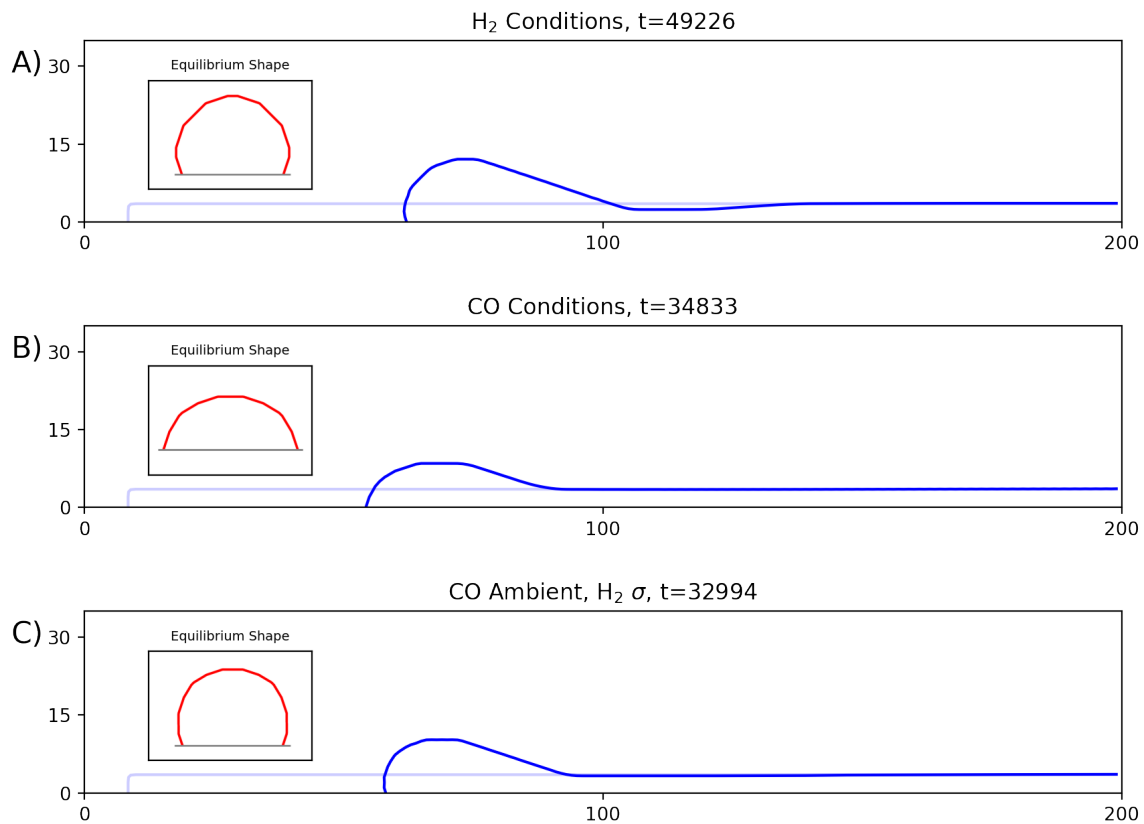
Figure 3-8: Summary of simulation results with equal axis scaling (comparable to TEM images). C) shows a fictitious system with the Wulff shape of the CO–based ambient and the effective contact angle of the H_2–based ambient. This shows that it is not effective contact angle which primarily drives valley formation.

3.3.3 Discussion of Computational Results

The simulations presented above were able to reproduce experimental results with high fidelity. It is notable that the simulations assumed isotropic surface energy, indicating that the most striking experimental features can be explained solely in terms of surface energy anisotropy. The enlargement of the top facet, relative to the equilibrium shape, on retracting rims and the fact that the leading side of the rim is composed of a single facet are both features which one might expect to result primarily from anisotropic diffusivity, but these simulations demonstrate that is not the case. Additionally, this work shows that the disparity between H_2-ambient behavior and CO-ambient behavior is more directly attributable to the different $\vec{\xi}(\hat{n})$, not the different σ.

3.4 Summary and Conclusions

The fundamentally different behavior exhibited by Ni (110) films annealed in our H_2- and CO-based ambients provides an opportunity to explore the fundamentals of valley formation during edge retraction. For films annealed in a H_2-based ambient, edges retracting along $[1\bar{1}0]$ directions exhibited significant valley formation and dewetted into particles with small top facets and a large effective contact angle ($\sigma \approx 0.4$). Films annealed in a CO-based ambient, retracting along the same direction, exhibited no valley formation and dewetted into particles with much larger top facets and a lower effective contact angle ($\sigma \approx -0.2$). Importantly, the H_2-ambient films eventually underwent pinch-off. As explored in Ref. [21], this pinch-off behavior is periodic and thus leads to retraction distance scaling linearly with time over sufficiently long time scales. The lack of pinch-off in CO-annealed films means that their edge-retraction rate will monotonically decrease with time, leading to greater morphological stability.

Our simulations demonstrate that this primary observation, in addition to the faceting of the rim's leading side and the enlargement of its top facet in both films, can be explained primarily by the features of $\vec{\xi}(\hat{n})$, without needing to invoke anisotropic

diffusivity or modify the effects of effective contact angle. This highlights the importance of correctly handling anisotropic surface energy in computational studies of dewetting. Additionally, the totality of these observations further demonstrates that dewetting behavior can be extremely sensitive to ambient conditions and that lessons learned from one set of conditions do not necessarily carry over to another.

Chapter 4

The Stability of Single-crystal Ruthenium Nanowires

4.1 Introduction and Background

Materials that are in cylindrical form are expected to break up into particles through a process first described for liquid jets by Plateau [29] and analyzed by Lord Rayleigh [27]. Rayleigh's instability analysis showed that a cylinder with isotropic surface energy and radius R_0 will decompose through growth of perturbations having a wavelength greater than $\lambda_{crit} = 2\pi R_0$. Nichols and Mullins showed that this result also holds for solid cylinders with isotropic surface energy that evolve through capillary-driven surface diffusion [30]. They further showed that when the shape evolves through surface diffusion, the fastest-growing perturbation has wavelength $\lambda_{max} = 2\sqrt{2}\,\pi\,R_0$, such that the resulting particles tend to be spaced at this distance. In addition, it was shown that the rate at which this perturbation grows is fixed for a given R_0, and increases with decreasing R_0. The analysis of Nichols and Mullins has been extended to the case of wires on substrates which they partially wet

with contact angles between 0 and 180° [45].

Santala and Glaeser showed that wire-shaped voids with lengths much greater than their average diameter that were artificially created in single crystals of sapphire broke up into more axisymmetric voids, as expected for a Rayleigh-like instability [32]. However, they found that the rate of this Rayleigh-like break up and the spacing and size of the voids that formed were strongly affected by the crystallographic orientation of the axis of the wire-shaped voids. More recently, Kim and Thompson showed that the break-up of Ni wires formed from patterned single crystal films broke up through a Rayleigh-like process that was also strongly dependent on the crystallographic orientation of the wire axis [5].

While Rayleigh-like break-up of wires with isotropic properties can be readily analyzed and simulated, the effects of anisotropy are much harder to treat, especially when facetted surfaces develop. Cahn originally studied the effects of anisotropy which was rotationally isotropic about the axis of a cylinder [84], while Gurski and McFadden more recently examined the stability of wires with cubic anisotropy [85]. However, a general understanding of the effects of anisotropy on the stability of wires has not emerged.

In this chapter we report on detailed studies of the break-up of single crystal Ru nanowires with axes aligned along different crystallographic directions. We find very pronounced effects of crystalline anisotropy on the Rayleigh-like break up of these wires and further show that break up of wires bound by equilibrium facets along their length is fully suppressed. We show that key features of these experiments are reproduced using a new level-set simulation of dewetting that captures the effects of anisotropic properties [ref to methods paper].

4.2   Experiments

Single-crystal (0001) Ru films were grown on (0001) sapphire substrates using DC magnetron sputtering, as detailed in reference [86]. Post deposition, but prior to

lithographic patterning, samples were step annealed in a vacuum furnace. The furnace tube was pumped down to 20 mTorr and then Ar/H_2 flowed at 16 sccm to provide a pressure of 100 mTorr during the annealing process. The furnace was then brought to $450°$ C and held for 1 hour. The temperature was subsequently increased in $100°$ C steps and held for one hour at each step until reaching and being held at 950C for 30 min. The temperature was then stepped down by $200°$ C every two hours until reaching $350°$ C, at which point it was allowed to cool to room temperature naturally. Ru was chosen both because of potential technological applications [87, 88] and because its HCP crystal structure seemed likely to yield behaviors which differed from those of well-studied FCC metals, such as Ni [4, 6, 8], and diamond cubic materials, such as Silicon [89, 90], in interesting ways.

For dewetting experiments, films were first patterned into large patches or long narrow strips using e-beam lithography. Patterned samples were then annealed in a tube furnace through which $95\%Ar/5\%H_2$ was flowing at 2300 sccm. The inner diameter of the furnace tube was 20.5mm. In experiments on large patterned rectangular patches of films, hundreds of microns in each dimension, it was found that annealing at $950°$ C for 3 hours resulted in solid-state dewetting to an intermediate state consisting of elongated wire-like features and hexagonal rings aligned along $< 11\bar{2}0 >$ directions, as shown in figure 4-1. This result suggested that wires with these alignments were likely to be resistant to Rayleigh-like breakup.

With this information, e-beam lithography was used to pattern radial arrays of nominally 10um long, 20nm wide strips of Ru from 5nm thick films. Each array contained 72 wires, each offset by $5°$ from its neighbors. The wafer was patterned with several replicate subsamples, each patterned with different e-beam exposure dosages to ensure at least one well-resolved subsample. Each subsample contained 10 such arrays, the first with 6 strips aligned along $< 11\bar{2}0 >$ directions and each subsequent array being increasingly offset from this in $0.5°$ increments, resulting in half-degree angular resolution overall. Figure 4-2 shows the layout of a single starburst, and figure 4-3 shows the lithographic pattern used to create the full array. This sample was
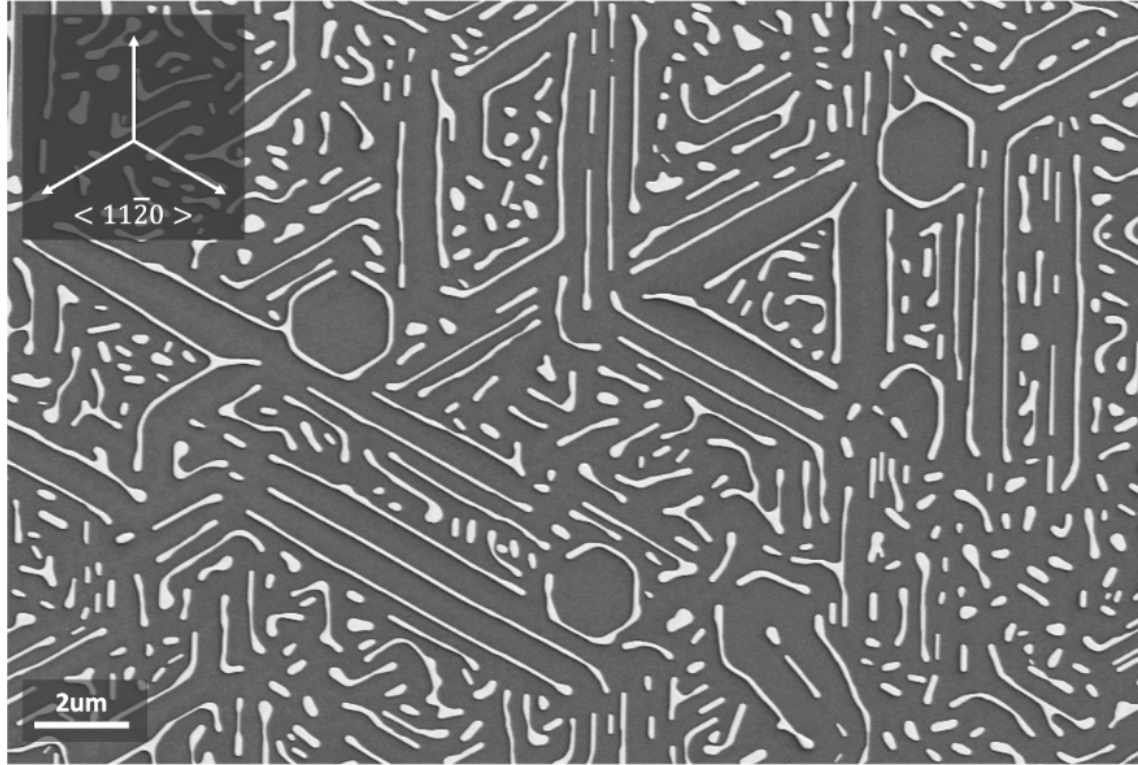
Figure 4-1: Representative view of a 5nm-thick (0001) Ru film annealed at 950° C for 3 hours. Solid state dewetting led to an intermediate state composed of wire-like features aligned along $< 11\bar{2}0 >$ orientations.

then annealed at 915° C for 3 hours and subsequently studied using high-resolution scanning electron microscopy (HRSEM). During annealing, the sides of the strips retracted to form wires and then most of the wires broke up into particles. The results from the best-resolved subsample, summarized in figure 4-4, are striking (other subsamples patterned with other dosages had strips which differed slightly in initial width but yielded very similar behavior).

Wires aligned along $< 11\bar{2}0 >$ directions were seen to be much more stable than wires with other orientations, with most remaining entirely intact and contracting significantly in length, while those offset by even a few degrees underwent negligible length contraction and broke up into dozens of particles. The dependence of both the number of particles and length contraction on strip orientation is highly non-uniform, with sharp cusps at stable orientations and the majority of the effect being saturated within a few degrees of offset.
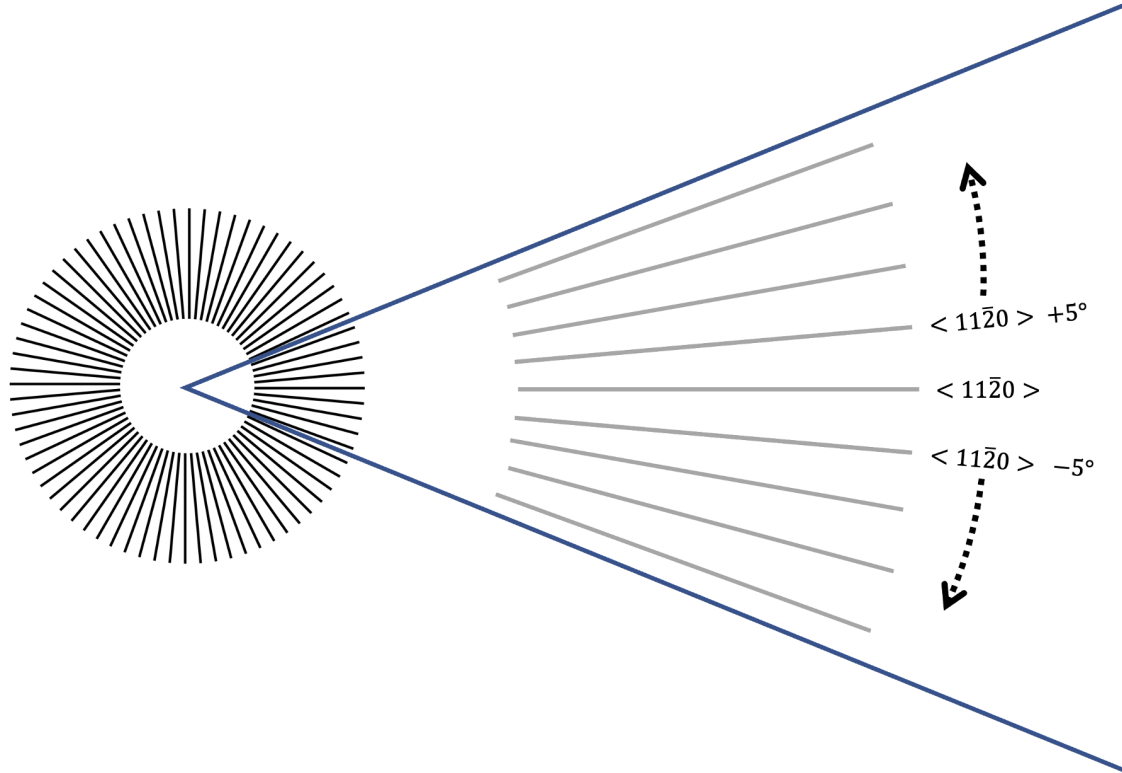
Figure 4-2: This figure shows a schematic of a single starburst array that includes wires with crystallographic axes aligned along $< 11\bar{2}0 >$ directions with other wires that are off-set by 5° increments. The full pattern shown in figure 4-3 consists of 50 such arrays with different orientations and as-patterned line widths.

A cross-sectional Transmission Electron Microscope (TEM) image of a stable Ru wire is shown in figure 4-5(a). This image shows that the wire is bound by specific low index facets. The wire was sectioned such that the image plane was normal to the axis of the wire, Fig. 4-5(b). The observed facets correspond well with equilibrium facets on the Wulff shape [15] generated from DFT calculations using the 3 lowest energy planes of Ru [72]. This supports the understanding that the facets seen in the cross-sectional image lie parallel to the axis of the wire. The Wulff shape shown in Fig. 4-5(c) has been generated with slightly rounded corners and edges to match the experimental observation. A wire bound by facets along its length is expected to be resistant to a Rayleigh-like break up because of the large energy penalty associated with growth of perturbations of the stable facets. This having been said, we have found that this effect is surprisingly strong, even in the presence of rounded corners
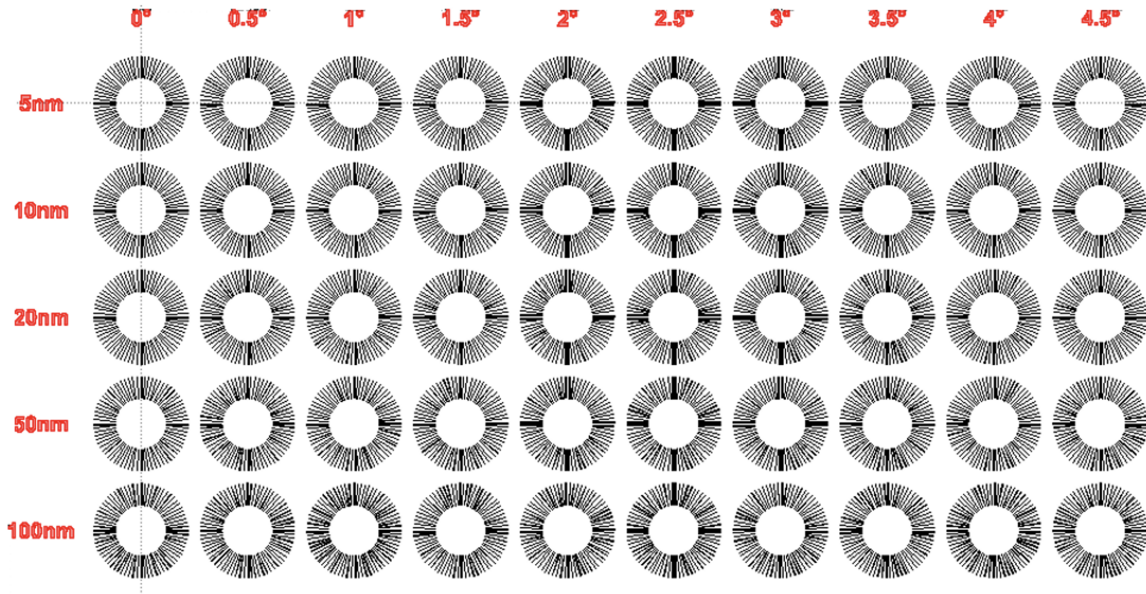
Figure 4-3: The full lithographic pattern used to create the first batch of samples. The labels on the left indicate the nominal strip width of the arrays in that row, and the labels across the top indicate the rotation of the starbursts in that column, relative to the alignment shown in the inset of figure 4-2. In practice, the pattern was not well-resolved for 5nm and 10nm wide strips. Multiple replicates of this pattern were created on the same wafer, using a different e-beam dosage for each replicate. The data used in this paper came from the replicate corresponding to a beam dosage of 3800 $\mu C/cm^2$.

and edges.

To explore the mechanisms leading to this very strongly orientation-dependent behavior, we patterned a new sample with starbursts of initially ~ 70 nm–wide strips. These strips were patterned by using a PMMA lift-off process to pattern an SiO_2 hard mask over the Ru film. This more complex patterning process was used because of COVID–era difficulties in obtaining HSQ. These wider samples were annealed under the same conditions as above in short time increments and examined between anneals using HRSEM. The sides of the strips rapidly retracted to form wires, and these wires then displayed behavior similar to that described above. The larger wire diameter led to slower evolution and to features that were more readily resolved in HRSEM images. Note that wires of all orientations have nominally identical cross-sectional areas, and in the isotropic case, would be expected to break up at the same rate to form particles
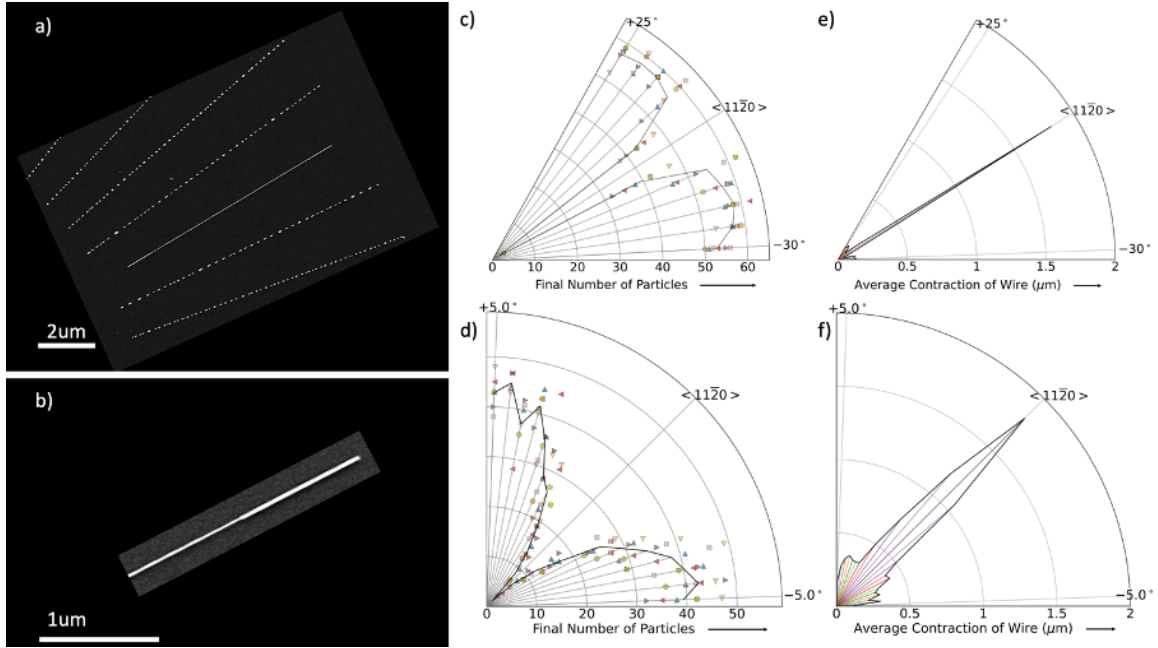
Figure 4-4: Summary of experimental results for patterned 20nm-wide lines (see figure 4-5 for post-anneal cross-section). (a) A representative image of dewetted wires after annealing at 950° C for 3 hrs. The wire aligned along a $< 11\bar{2}0 >$ direction has not broken up, but it has shortened significantly. Lines with other orientations have broken up but have not significantly shortened. (b) A close up of the end of the stable wire, highlighting how mazss from the retracting end has accumulated in a sharply defined thicker segment. (c) and (d) Plots of the average number of particles as a function of wire orientation, with (c) showing the whole range in 5° increments and (d) focusing on lines lying between ±5° around the central cusp in half-degree increments. Points show results for individual wires and the line indicates the average. e) and f) Plots of the average length contraction as a function of orientation, at 5° and 0.5° increments, respectively. For unstable wires, length contraction is defined as the difference between the as-patterned length and the distance between the two outermost particles.

with the same size and spacing. As previous work on single-crystal wire stability [5] would suggest, the development of a Rayleigh-like instability is evident for all but the wires aligned along $< 11\bar{2}0 >$ directions. Fig. 4-6(a) shows the development of such an instability on a wire offset from $< 11\bar{2}0 >$ by 5° . The wavelength of this instability is relatively large and leads to large particles at correspondingly large spacings. For larger angular offsets (Fig. 4-6(b), the periodicity of break-up, and thus the final spacing of the particles, was significantly smaller. In all cases, the Rayleigh instability develops with some irregularity along the length of the wire because it
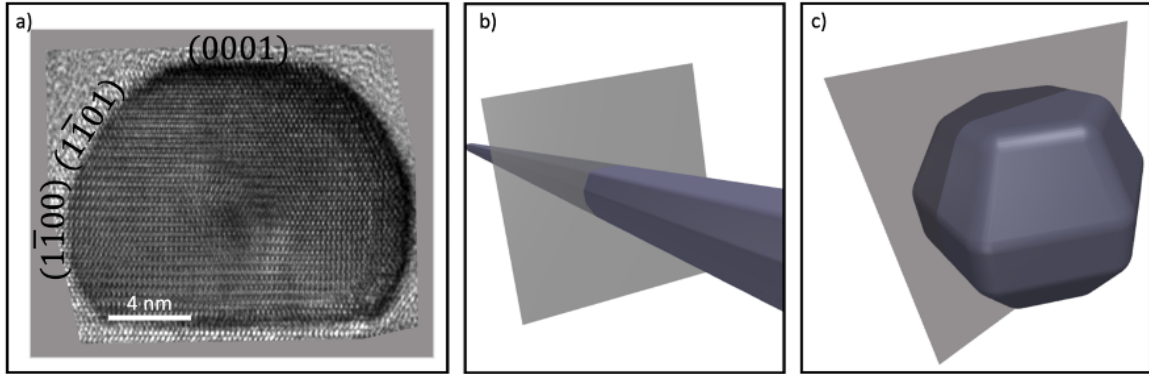
Figure 4-5: a) A cross-section of a stable wire obtained using focused ion beam sectioning and transmission electron microscopy. (b) Illustration of the TEM image plane relative to the axis of the wire, and c) the Wulff shape assumed in our simulations, with the relevant cross-sectional plane from (a) and (b) shown in gray.
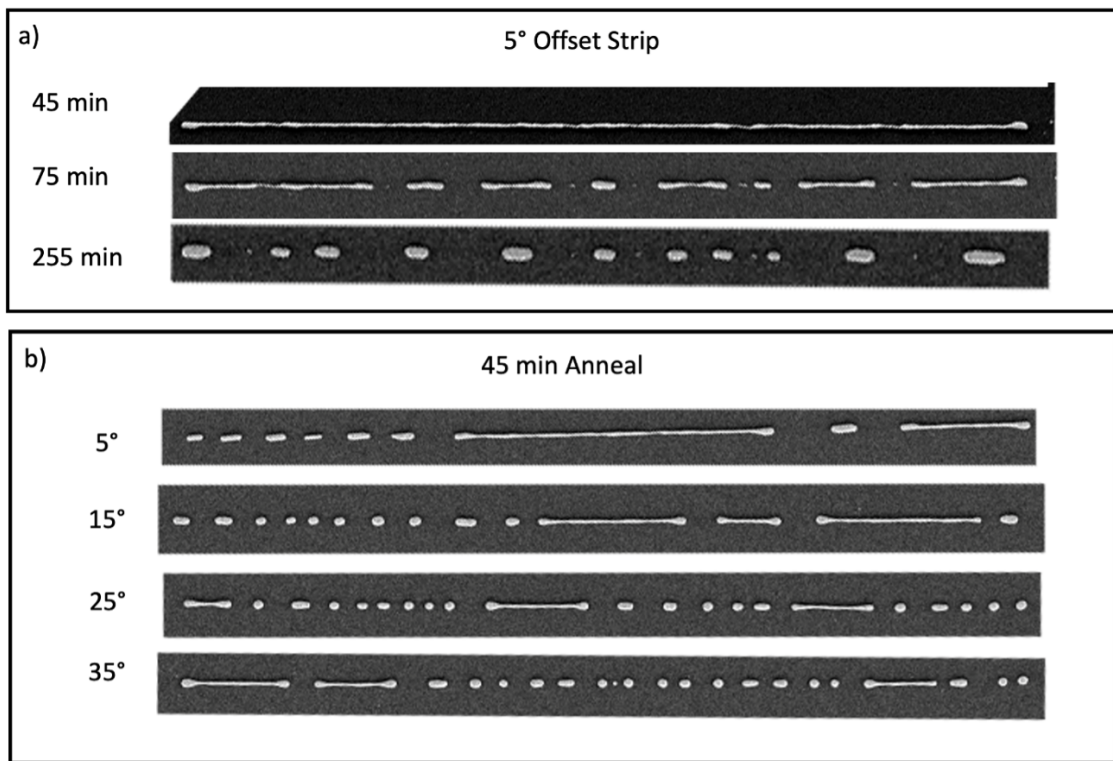
Figure 4-6: Images at selected times showing the evolution of a wire with 5° offset relative to a $< 11\bar{2}0 >$ direction, showing mostly Rayleigh-like breakup. b) Wires with selected offsets after 45 min of annealing showing evidence of both Rayleigh-like and ovulation behavior. Note that breakup of the 5° wires in both a) and b) leads to a significantly greater characteristic spacing than the wires with larger offset, which share similar particle spacings.

arises from random perturbations to the wire's surface. Therefore, at intermediate stages, long segments of unbroken wire coexist with fully-formed particles. These particles are observed to have a relatively broad distributions of sizes and spacings.

4.3 Simulations

To better understand the phenomenological observations made above, we used our recently developed simulation method, see chapter 2, to simulate the evolution of finite, cylindrical, free-standing Ru wires. In dimensionless units, these wires had length 379, and radius 5, with an initial sinusoidal perturbation of wavelength 10 and amplitude 0.1 to provide some surface roughness. Simulations were conducted using a Cahn-Hoffman vector $\vec{\xi}(\hat{n})$, corresponding to the Wulff shape shown in Fig. 4-5(b), see Supplementary Information for more details. The role of $\vec{\xi}(\hat{n})$ in encoding surface energy anisotropy in our simulations is discussed in detail in chapter 2[citation of methods paper]. In short, $\vec{\xi}(\hat{n})$ is a vector-valued quantity derived from material's surface energy $\gamma(\hat{n})$. Taking the divergence of $\vec{\xi}(\hat{n})$ along an object's surface yields it's weighted mean curvature, denoted κ^{γ}, which can be used as a replacement for the product $\kappa \cdot \gamma$ in the isotropic Mullins equation. Simulations were conducted for wires offset from $< 11\bar{2}0 >$ by $5°$, $10°$, $20°$, and $30°$, in the same plane as the experiment. For computational efficiency, only the top half of the wires were simulated, and mirror boundary conditions were used. A wire aligned along the stable orientation was simulated as well. The simulations used in this paper were implemented using the code developed in chapter 2. The surface energies used to create $\vec{\xi}(\hat{n})$ for these simulations were 2.6 for $\{0001\}$ surfaces, 2.88 for $< 11\bar{2}0 >$ surfaces, and 2.91 for $< 11\bar{2}0 >$ surfaces. These correspond to the DFT-obtained surface energies, in J/m^2, found in Ref. [72], however units are not used inside the simulation. All measures of length used in reference to the simulation (for example, the initial length of 379) are given in terms of the grid spacing underlying the simulation. Measurements of time come from the velocity term in the Mullins equation $v = -B\nabla_S^2 \kappa^{\gamma} = -B\nabla_S^2 \left(\nabla_S^2 \vec{\xi}(\hat{n}) \right)$. In all simulations shown in this paper, B is simply taken to be 1 for all surface orientations.

Thus, the measurements of time and length given by the simulations could be easily rescaled to physical units if B,$\vec{\xi}\left(\hat{n}\right)$, and the grid spacing were assigned physical values. As discussed in chapter 2, the level-set function $\phi\left(\vec{x},t\right)$ is smoothed by adding a term which penalizes $\nabla^{2}\phi\left(\vec{x},t\right)$ to the diffusion potential. In the simulations shown here, the numerical pre-factor multiplying $\nabla^{2}\phi\left(\vec{x},t\right)$ was set to 0.4.

As in the experiments, the simulated wire aligned along the $<11\bar{2}0>$ contracted significantly in length with no breakup or evidence of a Rayleigh-like instability. In the other simulations, ovulation [31] of the wires' ends led to greatly reduced contraction in length—measured as the difference between the initial length of the wire and the span between the two farthest points of Ru surface once evolution is complete, see Fig. 4-7(a).
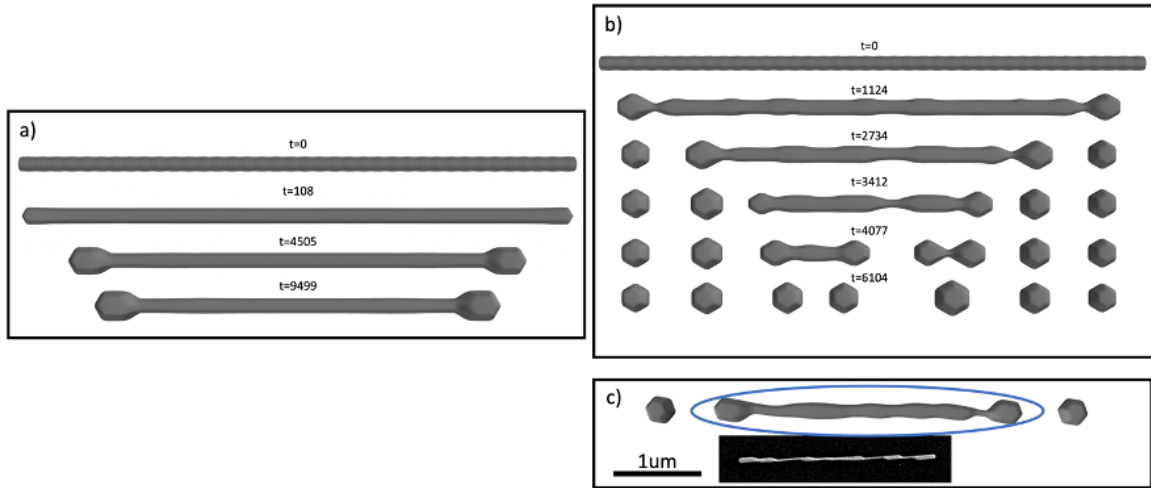
Figure 4-7: Examples of simulations reproducing experimentally observed behavior. a) A stable (0° offset) wire undergoing length contraction with no ovulation or Rayleigh instability. b) Simulation of a wire offset from the stable orientation by 30°. Both Rayleigh-like and ovulation modes are evident. c) A snapshot from a 10° offset simulation matching the behavior of a segment of a 6° offset wire from experiment. The values for time given in the simulations can be compared across figures but are not directly comparable to experiments. Full videos of both a) (wire_0_degree.mp4) and b) (wire_30_degree.mp4) are available in Supplemental Materials.

For all non-zero offsets, Rayleigh instabilities develop along the length of the wire, with the instability on the 5° offset wire having a much larger wavelength. Rayleigh-

like pinch-off does not occur everywhere at the same time, so long segments coexist with fully broken-up regions, as in experiments. The ends of the long segments begin to ovulate as they retract so that ovulation significantly contributes to the overall break-up process, Fig. 4-7(b) shows an example. Qualitative comparisons of simulation snapshots and experimental images suggest that the simulations are faithfully capturing many details of the experimental system, as exemplified in Fig. 4-7(c). These comparisons also drew attention to experimental images in which ovulation appears to be occurring or to have recently occurred, including at the ends of long segments created by Rayleigh-like pinch-off. From such comparisons, we conclude that both Rayleigh-like modes and ovulation play critical roles in the breakup of Ru nanowires and that it is the combination of Rayleigh-like pinch-off and ovulation that leads to the relatively broad distributions of particle sizes and spacings observed in both the simulations and experiments. The importance of ovulation, particularly ovulation acting on long segments created from initially Rayleigh-like behavior, is an unexpected result that challenges the idea that the Rayleigh instability is the dominant mechanism of breakup for long wires. It is especially noteworthy that wires bound by facets along their length are stable with respect to both Rayleigh break-up and ovulation. The simulations reproduce the experimentally observed orientational sensitivity of both the retraction distance and the number of particles into which a wire breaks up, as shown in Fig. 4-8.
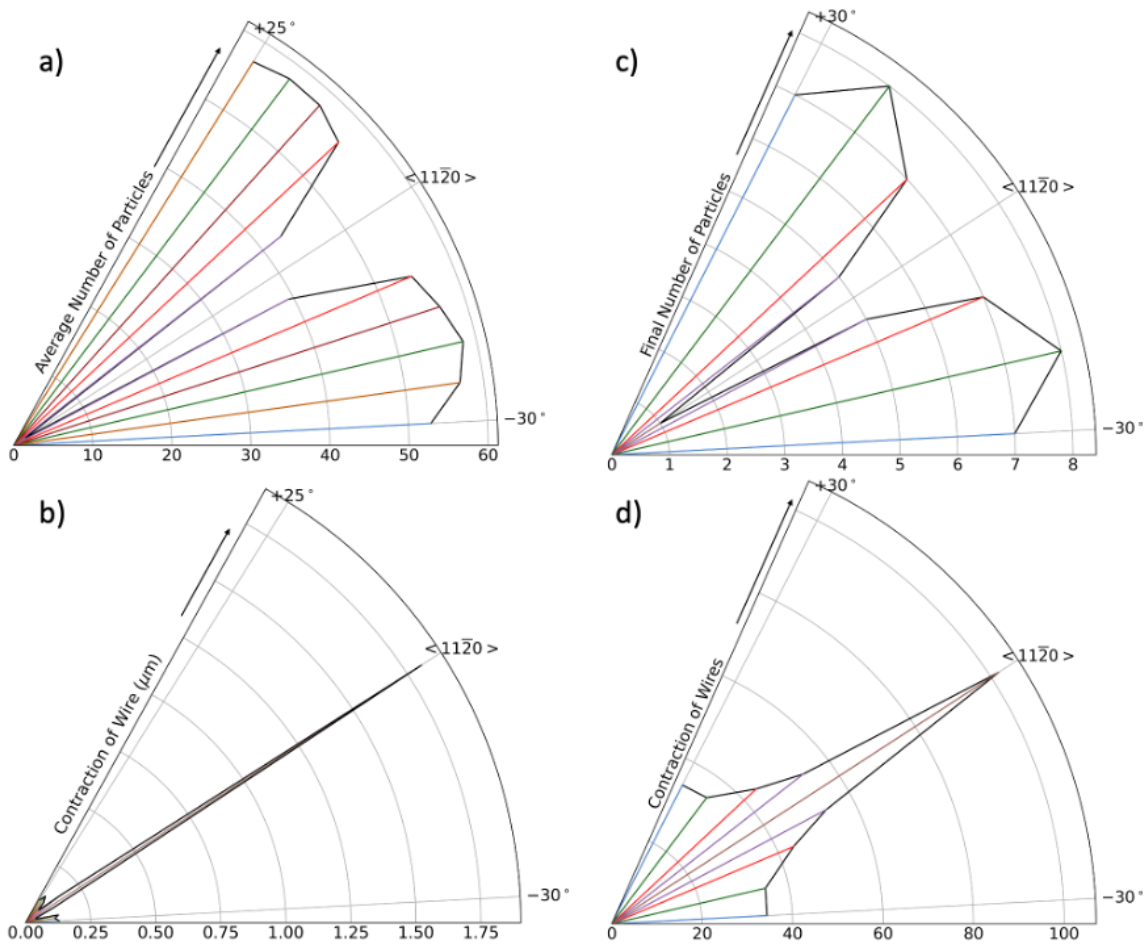
Figure 4-8: Comparison of experimental and simulation results. a) and b) in this figure reproduce the data in Figs. 4-4 (c) and (e) while c) and d) in this figure show analogous plots based on simulation results. Each orientation is assigned a distinct color, so that results can be readily compared.

4.3.1 Additional Simulation Time Series

Time series from simulations of wires with the stable orientation and a 30° offset are shown in Fig. 4-7. Time series for the other simulations referenced in this chapter are shown below. Full videos of all simulations referenced in this chapter are also available in Supplemental Materials.

t=0

t=418

t=5982

t=7433

t=11821
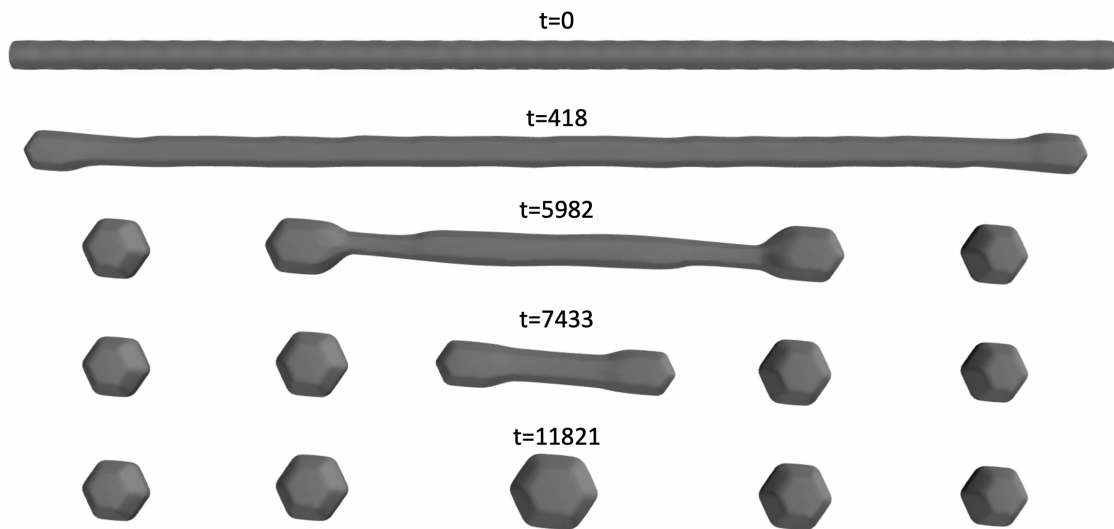
Figure 4-9: Time series of simulated ruthenium nanowire with 5° offset. See Supplemental Materials (wire_5_degree.mp4) for a full video.

t=0

t=800

t=2141

t=4764

t=6620
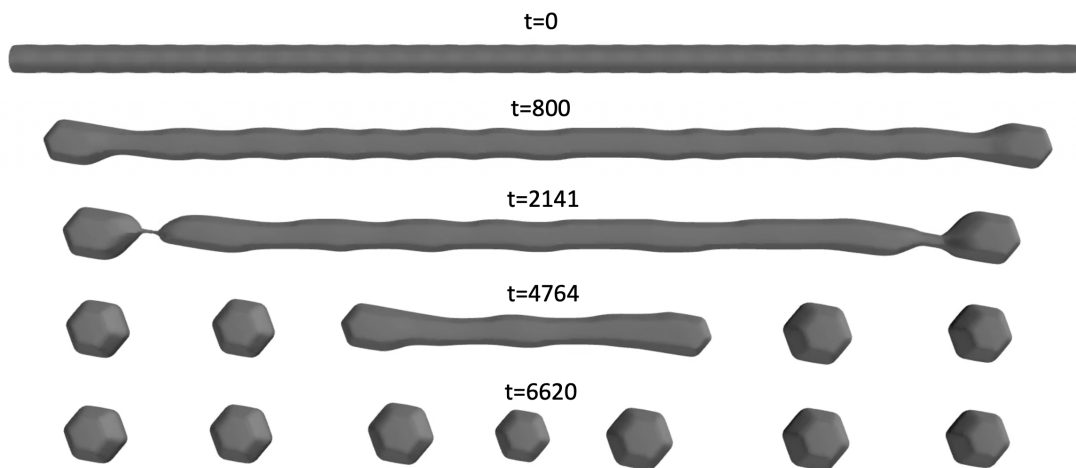
Figure 4-10: Time series of simulated ruthenium nanowire with 10° offset. See Supplemental Materials (wire_10_degree.mp4) for a full video.
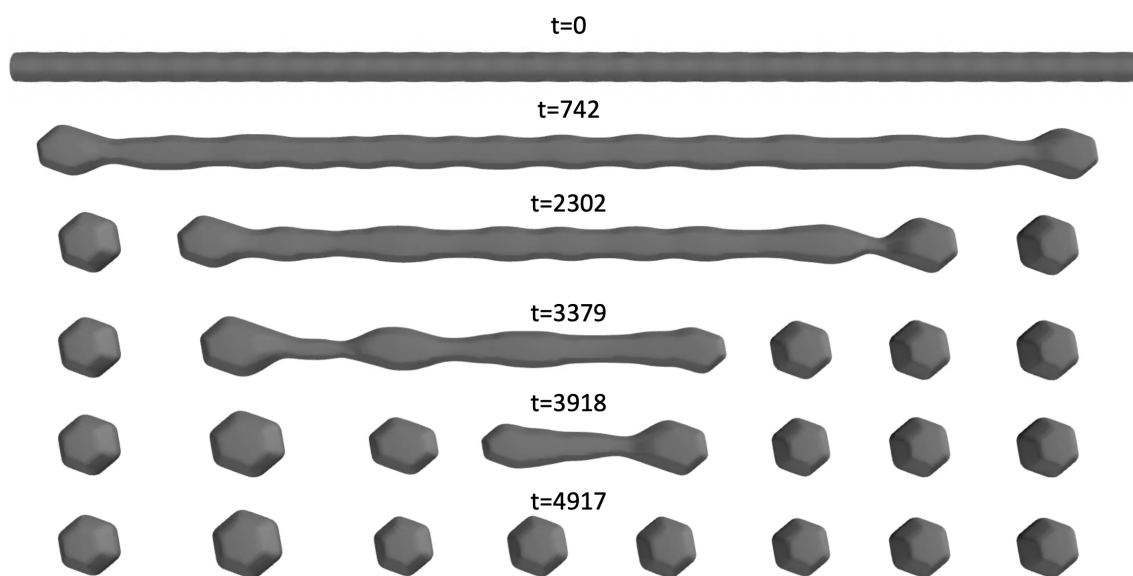
Figure 4-11: Time series of simulated ruthenium nanowire with 20° offset. See Supplemental Materials (wire_20_degree.mp4) for a full video.

4.4 Conclusions

Understanding the morphological stability of nanowires with strongly anisotropic properties has proven to be a challenging problem for some time. In experiments using single crystal Ru nanowires aligned along different crystallographic axes, we have shown that wires bound by facets along their length are stable with respect to Rayleigh-like break-up and ovulation, while wires with nominally the same cross-sectional dimensions but different orientations breakup through an interplay of both mechanisms. We show that a level-set simulation that accounts for the effects of strong surface energy anisotropy reproduces the behavior seen in experiments. These results point to the importance of crystallographic alignment in producing morphologically stable nanostructures and provides a framework for analysis and prediction of morphological stability that accounts for the strong crystalline anisotropy.

Chapter 5

A Simple Model of Dendritic Dewetting

* This chapter is adapted from an upcoming paper [91].

In several materials systems, it has been observed that the rims of growing holes can become unstable and develop dendritic morphology [6, 75, 89, 92–97]. Experimental characterization of these dewetting dendrites [7] has identified key features which hint at the underlying mechanisms of their growth including:

1. These dewetting dendrites are oriented such that their main axis is along specific crystallographic orientations.

2. The rim height at the tip of the dendrite is small and doesn't increase over time.

3. The tips of the dendrites propagate with constant velocity [7].

Recently, kinetic Monte Carlo (KMC) simulations have also been used to explore hole growth phenomenology from an atomistic perspective [98]. Despite their scientific and practical interest, a clear explanation of dendritic dewetting phenomenology is absent from the literature. On the other hand, dendritic solidification has been studied and explained far more thoroughly (see Refs. [99–101], for example). The striking resemblance dewetting and solidification dendrites bear to one another, as
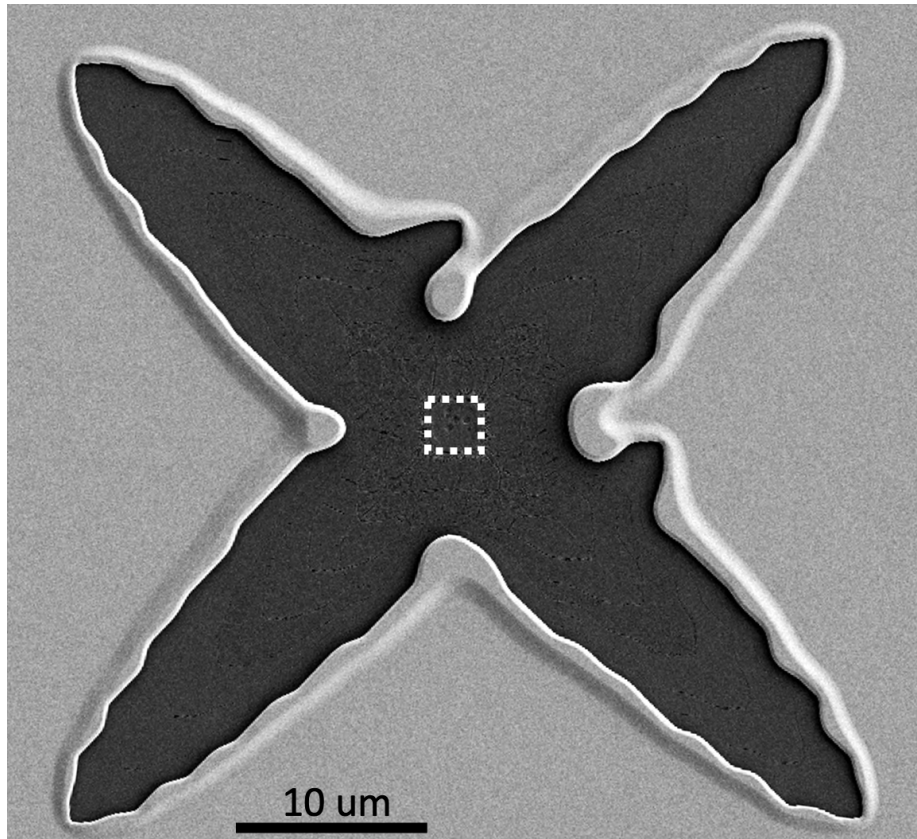
Figure 5-1: An initially square hole (outlined with white dashed line), the corners of which have become unstable and begun to exhibit dendritic behavior. The film (light gray) is an 85nm Ni (100) film on MgO (dark gray) annealed for 6hrs at 950° C in flowing 95% H_2, 5% N_2.

well as the observation that both phenomena arise in systems with diffusive transport in a highly out of equilibrium system, suggests that an analogy between these two systems might provide insight into dendritic dewetting. In this chapter, we formalize this analogy and explore the space of behaviors it predicts, drawing inspiration from comparisons to both dewetting experiments and the solidification literature.

First, we illustrate that the physics of dewetting can be modeled as a two-dimensional problem by separating the effects of in-plane and out-of-plane curvatures—which we will denote κ_{tl} (tl for triple–line) and κ_{rim}, respectively—and embedding them as effective quantities defined along the triple–line. In other words, the triple–line is treated as a dynamic curve in two spatial dimensions, and the height of the rim ahead of the triple–line is inferred by the volume accumulated during retraction. These two

quantities are used to calculate the motion of the triple–line, as detailed below. In analogy to the stabilizing effect of surface tension on the Mullins-Sekerka instability, linear stability analysis of our simplified dewetting model shows that the triple–line is fundamentally unstable unless an equivalent line-tension term appears. Next, we find that further insight into dewetting is provided by comparison to dendritic solid-ification and the Saffman-Taylor instability in Hele-Shaw cells [102]. In particular, we explore how these systems relate to the notion of microscopic solvability (the idea that dendrite morphologies are stable attractors in configuration space [101]) as a necessary condition for steady–state pattern selection (i.e. dendritic morphologies) and propose that the combined effect of anisotropic surface energy and diffusivity can satisfy an analogous solvability condition in dewetting systems. We illustrate the plausibility of this solvability condition by studying the role of anisotropy in level-set simulations of our model, making use of the method of characteristics to visualize the role of anisotropy.

5.1 Background

According to the Mullins equation developed for isotropic systems [40], surface self-diffusion driven by gradients in curvature leads to surfaces whose velocity along their normal is proportional to the surface Laplacian of curvature. In the case of a straight edge in a semi-infinite thin film, mass flows from the triple line and accumulates in a growing rim. The profile of this rim determines the flux of mass normal to the triple–line, see Figure 5-2. Larger rims lead to a lower overall driving force for edge retraction, and approximating the rim as having a semi-circular cross-section along which rejected mass diffuses yields that the velocity of the rim, $v \propto h^{-3}$ [7, 20]. For edges retracting away from their center of curvature—such as a hole in a film—this relationship is more complicated, as the arc-length of the triple–line is increasing, spreading out the accumulated mass over a greater length of rim. This reduces the rim height in regions of high curvature (κ_{tl} is defined to be positive for regions of triple–line protruding into the film, as in Figure 5-2), driving faster retraction. Likewise, regions
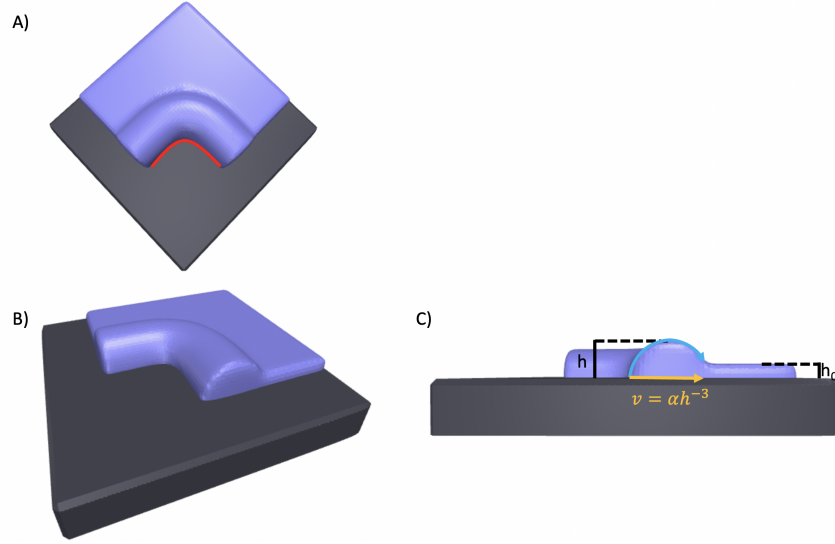
Figure 5-2: Schematic of assumed corner geometry. A) Top view with triple–line highlighted in red. B) Perspective view. C) Side view highlighting the path of material rejected away from the triple–line (blue) and the dependence of retraction velocity on rim height (yellow).

in which $\kappa_{\text{tl}} < 0$ accumulate mass in their rims more quickly and therefore retract more slowly. Additionally, as we explore below, κ_{tl} can be thought of as interacting with an effective line tension that resists increases in κ_{tl}.

In single-crystal films, sufficiently large holes of any initial shape grow to be bound by kinetically stable edges with straight morphologies that, due to the combined effects of both anisotropic surface energy and diffusivity, retract more slowly than edges with other orientations [6]. However, the corners of these holes are localized regions of high in-plane curvature and can become unstable and propagate faster than the rest of the hole as mass rejected from the triple line accumulates in the straight sections of rim left behind by the corner. These corners propagate along specific crystallographic directions and develop dendritic morphologies as they race ahead of the rest of the rim.

Solidification fronts exhibit a similar curvature–induced enhancement/retardation dynamic, as shown in the analyses of Mullins and Sekerka [99, 100]. During solidification, the rate at which either heat (for a pure system) or solute (for an alloy) is dissipated away from the solidification front controls the rate of solidification. The

heat/solute accumulates ahead of the solidification front and decreases the local driving force. This accumulation of heat/solute is analogous to the increase of rim height ahead of a dewetting triple–line. The key insight made by Mullins and Sekerka was that areas of positive curvature increase the arc-length of the solidification front as they grow. This increases the area over which rejected heat/solute is dissipated, locally reducing the concentration of heat/solute and increasing the driving force for solidification. Likewise, areas of negative curvature lead to rejected heat/solute accumulating more rapidly ahead of the front, reducing the driving force for solidification. In this model, any perturbation of the solidification front will be amplified over time. However, Mullins and Sekerka's initial analysis ignored the effect of surface tension, as did early work on steady–state tip morphology [103, 104]. Attempts to rectify this issue instead determined that any degree of capillarity in an isotropic system eliminated the dendritic instability, as the tips of runaway perturbations would be blunted by capillary effects and grow in size [101, 105–108]. Two review papers by Langer [101, 109] provide an excellent overview of these models, their successes, and their shortcomings. Instead, it was determined that dendritic solidification was only possible in the presence of surface energy anisotropy that fixes the dendrite tip's geometry, a condition called solvability [101]. More specifically, solvability theory hypothesizes that a necessary condition for dendritic behavior is the existence of a tip geometry that is an attracting fixed point in configuration space [101]. This means that solidification dendrites propagate along specific crystallographic axes, as in dewetting. Clearly there are parallels between these two systems, which we discuss below in more depth.

5.2 Building an Analytical Model

To formalize the analogy between dendritic dewetting and dendritic solidification, we developed a simple analytical model of dewetting. Our model assumes that the rim ahead of the triple–line has a semi-circular cross-section of radius h, which we illustrate for the corner of a rectangular hole in figure 5-2. Our model focuses only

on mass transport orthogonal to the triple–line which we justify by noting the gradient in chemical potential should be far larger in this direction than along the rim, unless $\nabla_s \kappa_{tl}$ is very large. This is supported by experimental observations showing that rim height varies relatively slowly along the rim [7] and by noting that in-plane curvature of the triple–line creates roughly equal and opposite gradients of curvature on the hole–side and film–side of the rim, a point which will have further significance in our analysis below. We assume that mass rejected from the triple–line accumulates in the rim with a semi-circular cross-section, such that the effective gradient in curvature over the rim goes as h^{-2} and the retraction velocity goes as h^{-3}, where h is the height of the rim. Notably we assume the same rim geometry as Brandon and Bradshaw's analysis [20] and obtain the same scaling relationships, but as Ref. [24] shows, Brandon and Bradshaw's model makes two errors that happen to cancel and yield the correct result. Namely, Brandon and Bradshaw take retraction velocity to go as the first derivative of curvature, rather than the second derivative, while also erroneously scaling the rate of mass accumulation with the height of the rim, rather than the height of the film, recovering an extra factor of h left out by their first mistake. In either case, it has been noted that this geometric construction does not correctly treat the region of transition between the rim and unperturbed film and thus does not rigorously conserve volume [24]. In principle, this criticism is valid, but the development of a valley ahead of the dewetting rim, as seen in [21, 39], shows that this transition region is far smoother than in the volume conserving model proposed in [24]. Importantly, the construction presented here predicts that the retraction distance of a straight edge should scale as $t^{2/5}$, which is, after initial transients, the scaling predicted by far more sophisticated models, [21, 24, 39] and observed in experiments [6, 25].

Using this construction, we can, at every time t, uniquely label each point along the triple–line, $\vec{x}$ and assign to it a value $h(\vec{x}, t)$, defined as the maximum height of the rim along a line emanating from that point, normal to the triple–line, see Figure

110

5-2. The velocity of the triple–line is a function of this height,

$$v(\vec{x}, t) = \alpha h^{-3}(\vec{x}, t). \tag{5.1}$$

As discussed above, it is important to correctly capture the effect of the triple–line's in-plane curvature on the in-plane arc-length of the rim. Such curvature leads to either localized arc-length expansion or contraction, which, in turn, either enhances or counteracts the dissipation of mass rejected from the triple–line, respectively. For a small segment of rim of arc-length L which has volume V and in-plane curvature κ_{tl}, the cross-sectional area A of the rim is given by $\frac{V}{L}$. We want to see how A changes as the rim advances. If we use ν to describe the displacement of the triple–line along its normal, we find that

$$\frac{\partial A}{\partial \nu} = \frac{\partial}{\partial \nu}\left(\frac{V}{L}\right) = \frac{\frac{\partial V}{\partial \nu}L - V\frac{\partial L}{\partial \nu}}{L^2} \tag{5.2}$$

$$= \frac{h_0 L \cdot L}{L^2} - \frac{V\kappa_{tl}L}{L^2}$$

$$= h_0 - \frac{V\kappa_{tl}}{L}$$

$$= h_0 - A\kappa_{tl}$$

$$\frac{\partial A}{\partial \nu} = h_0 - \kappa_{tl}\frac{\pi}{2}h^2 \tag{5.3}$$

To convert back to rim height,
$$\frac{\partial h}{\partial t} = \frac{\partial A}{\partial t}\frac{\partial h}{\partial A}.$$

For a semi-circular rim, this yields

$$\frac{\partial h}{\partial t} = \frac{\alpha h_0}{\pi h^4} - \frac{\alpha \kappa_{tl}}{2h^2}. \tag{5.4}$$

Finally, since velocity is only a function of rim height,

$$\frac{\partial v}{\partial t} = \frac{\partial v}{\partial h}\frac{\partial h}{\partial t},$$

111

$$\frac{\partial v}{\partial t} = \frac{3\alpha^2 \kappa_{\mathrm{tl}}}{2h^6} - \frac{3\alpha^2 h_0}{\pi h^8}. \tag{5.5}$$

In analogy with Mullins and Sekerka [100], we examine the behavior of a retracting rim with a small sinusoidal perturbation. If we imagine a nearly straight retracting triple–line with in-plane profile

$$y(x,t) = y_0(t) + \delta(t)\sin(kx), \tag{5.6}$$

such that the positive y-direction points into the film and $y_0(t) \propto t^{2/5}$ denotes the retraction distance of an equivalent triple–line without a perturbation, for small delta, $\kappa_{\mathrm{tl}} \approx -y'' = \delta k^2 \sin(kx)$. The minus sign in our expression for triple–line curvature preserves the sign conventions we established above. This means that

$$\frac{\partial v}{\partial t} = \frac{3\alpha^2 \delta k^2 \sin(kx)}{2h^6} - \frac{3\alpha^2 h_0}{\pi h^8}.$$

Therefore, in the frame of reference moving with the velocity of an unperturbed rim,

$$\frac{\ddot{\delta}}{\delta} = \frac{3\alpha^2 k^2}{2h^6}. \tag{5.7}$$

According to this analysis, all perturbations are unstable (i.e., they have positive acceleration when $\delta \sin(kx)$ is positive and negative acceleration where $\delta \sin(kx)$ is negative), with shorter wavelength perturbations being more unstable.

5.3 Comparison to Simulation

The model produces highly unstable behavior, but from the Mullins-and-Sekerka-style analysis alone, it is difficult to tell if our model captures fully dendritic behavior. For this, we turn to computational modeling, specifically a simple level-set method simulation [110, 111] in which the signed distance function $\phi(\vec{x},t)$ is the distance from the triple line measured in the plane of the substrate, and the rim height $h(\vec{x},t)$ is stored on the same grid as ϕ. The triple line is advanced according to equation 5.1

112

and the rim height is updated according to equation 5.4. Both the rim height and the velocity calculated at the triple line are extended over the entire computational domain using the Python package scikit-fmm's implementation of the Fast Marching algorithm [67–69]. Periodic redistancing of ϕ, which returns it to a signed-distance function, is also implemented using scikit-fmm. A discussion of numerical artifacts and volume conservation is presented in the supplementary information. Selected snapshots from one such simulation are shown in figure 5-3.
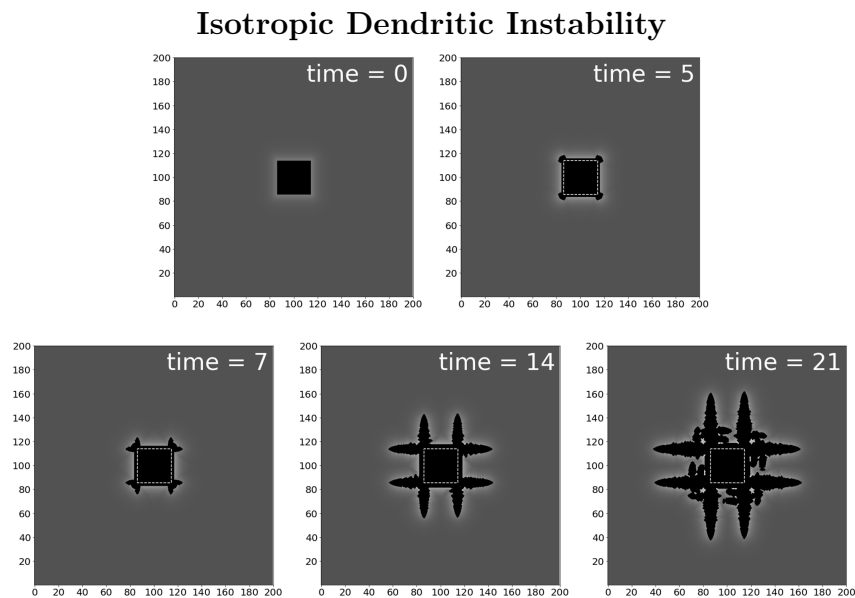
Figure 5-3: A level-set method simulation of our simple Mullins-and-Sekerka-inspired model. An initially square hole immediately exhibits dendritic instability at the corners.

The simulation appears to reproduce dendritic behavior, including a steady–state tip morphology and side-branching. However, as in Mullins and Sekerka's linear stability analysis that we emulate, the line tension of the interface (in this case the triple–line) is neglected.

5.4   Considering In-plane Capillarity

By embedding the gradient in curvature over the rim into a function of rim height, we have ignored the effective triple–line tension. As alluded to above, a region of

triple–line with non-zero in-plane curvature yields curvatures of opposite sign and roughly equal magnitude on the hole-facing and film-facing sides of the rim. For a section of triple–line with positive curvature, like the tip of a dendrite, the gradient of in-plane curvature of the rim has the opposite sign of the out-of-plane curvature gradient driving dewetting and thus acts to locally slow edge retraction. Within the context of our simple model outlined above, we account for this effect by rewriting our expression for triple–line velocity as $v = \alpha(\frac{1}{h} - \tau\kappa)h^{-2}$. The effective line tension, τ accounts for the gradient of curvature caused by in-plane triple–line curvature. For a semicircular rim, we assume $\tau \approx 2$, matching the assumption of equal and opposite curvatures, but it could vary with other rim geometries. The effective triple line tension can be related to the surface tension integrated over the surface area that is proximate to the triple line. It is plausible that this line tension could be a function of rim height, and we suggest this as a topic for further analysis. Repeating the analysis above with this new expression for v, noting that velocity now has a dependence on κ_{tl} and thus,

$$\frac{\partial v}{\partial t} = \frac{\partial v}{\partial h}\frac{\partial h}{\partial t} + \frac{\partial v}{\partial \kappa_{tl}}\frac{\partial \kappa_{tl}}{\partial t},$$

yields

$$\frac{dv}{dt} = -\frac{3\alpha^2 h_0}{\pi h^8} + \frac{5\alpha^2 h_0 \kappa_{tl}\tau}{\pi h^7} + \frac{3\alpha^2 \kappa_{tl}}{2h^6}$$
$$- \frac{2\alpha^2 h_0 \kappa_{tl}^2 \tau^2}{\pi h^6} - \frac{3\alpha^2 \kappa_{tl}^2 \tau}{2h^5}. \tag{5.8}$$

Again using a triple–line with an in–plane perturbation given by equation 5.6, we find that

$$\frac{dv}{dt} = -\frac{3\alpha^2 h_0}{\pi h^8} + \frac{3\alpha^2 \delta k^2 \sin(kx)}{2h^6} + \frac{5\alpha^2 \delta h_0 k^2 \tau \sin(kx)}{\pi h^7}$$
$$- \frac{3\alpha^2 \delta^2 k^4 \tau \sin^2(kx)}{2h^5} - \frac{2\alpha^2 \delta^2 h_0 k^4 \tau^2 \sin^2(kx)}{\pi h^6}$$

To first order, the front is still unstable, but the second order terms suggest that long-time behavior might be more complicated.

Capillary Suppression of Dendritic Instability
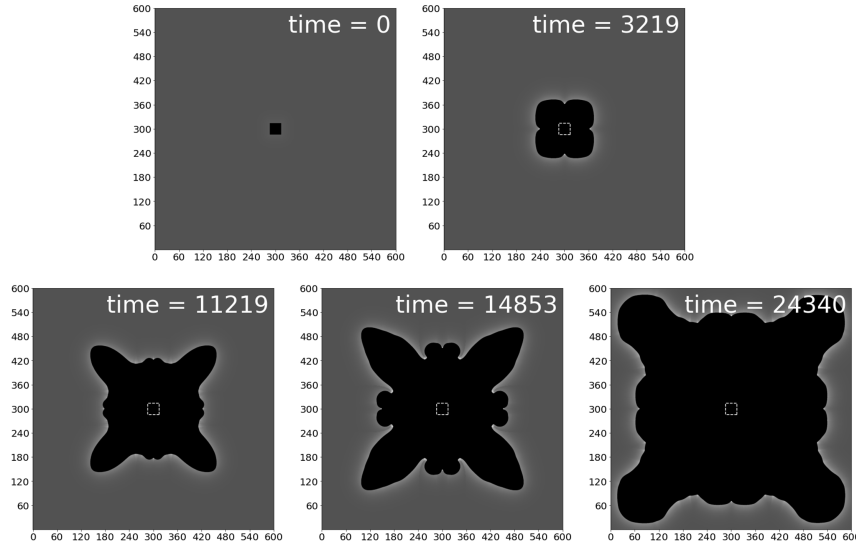
Figure 5-4: A simulation of an initially square hole with in-plane capillarity included in the model. System behavior is no longer dendritic and more closely resembles viscous fingering.

Simulations of the system described in this model, see figure 5-4, produce corners that do retract faster than the surrounding film but which also grow blunter over time and fail to achieve a steady–state, producing morphological evolution more evocative of viscous fingering in a radial Hele-Shaw cell [112] than of dendritic solidification. This finding is consistent with Langer's discussion of the two phenomena, [101] which highlights that dendritic solidification and viscous fingering are mathematically analogous, with pressure fulfilling the of role heat/solute and surface free energy density acting as an effective line tension. In our model of dewetting, we have decoupled the components of capillarity acting orthogonal and parallel to the triple–line, with the former analogous to the pressure in a Hele-Shaw cell and the latter acting as an effective line tension. In Hele-Shaw cells, this line tension means that the system lacks solvability, such that there is no tip geometry that propagates in a self-similar manner. Instead, viscous fingers are driven to grow increasingly blunt by line tension, matching the behavior of our simulated isotropic dewetting. Langer highlights a particularly insightful set of experiments by Couder et al. [113] in which viscous fingers are made to exhibit steady–state, dendrite-like behavior by air bubbles trapped at

their tips. These air bubbles bias the tips toward a specific radius of curvature, counteracting the capillary driving force toward broadening and thus endowing the system with solvability. In solidification, crystalline anisotropy plays a fundamentally similar role by providing a driving force that favors a specific tip geometry and length-scale. The experimental findings that dewetting dendrites consistently form along specific crystallographic directions suggests that anisotropy is playing a similar role in these systems as well.

5.5 The Role of Anisotropy

For dewetting films, anisotropic diffusivity and surface energy can cause edge retraction velocity to vary strongly as a function of in-plane orientation [6]. Given that long-time Brandon and Bradshaw scaling seems to be a universal feature of unperturbed triple–lines [24, 25], a reasonable but simple way to introduce anisotropy into our model and simulations is to add an orientation-dependent pre-factor to our equation for retraction velocity, such that $v = \alpha(\vec{n})(\frac{1}{h} - \tau\kappa)h^{-2}$, for triple–line normal vector $\vec{n}$. It is likely possible to gain analytical insights into this system of equations for certain well-behaved anisotropy functions, as in Barbieri, Hong, and Langer's work on solidification dendrites using WKB techniques [108, 114], but we believe that the level-set simulation method we have demonstrated above is better suited to studying long-time behavior. In the anisotropic simulations shown below, we chose

$$\alpha(\vec{n}) = \frac{1}{2}(1 + \beta(n_x^4 + \zeta n_x^2 ny^2 + ny^4)) \tag{5.9}$$

because it has tunable anisotropy and can be made to roughly match the shape of the effective $\alpha(\vec{n})$ measured for Ni (100) films [6]. For a film of unit thickness, our level-set simulation yields the behavior shown in figure 5-5 for $\beta = 3, \zeta = 6$.

This behavior is clearly dendritic, with the tip reaching a steady–state profile and side branches forming at later times. We have also explored our model's parameter space using this simulation technique, including the effects of film thickness (see figure

Anisotropic Dendritic Dewetting in a Film of Unit Thickness
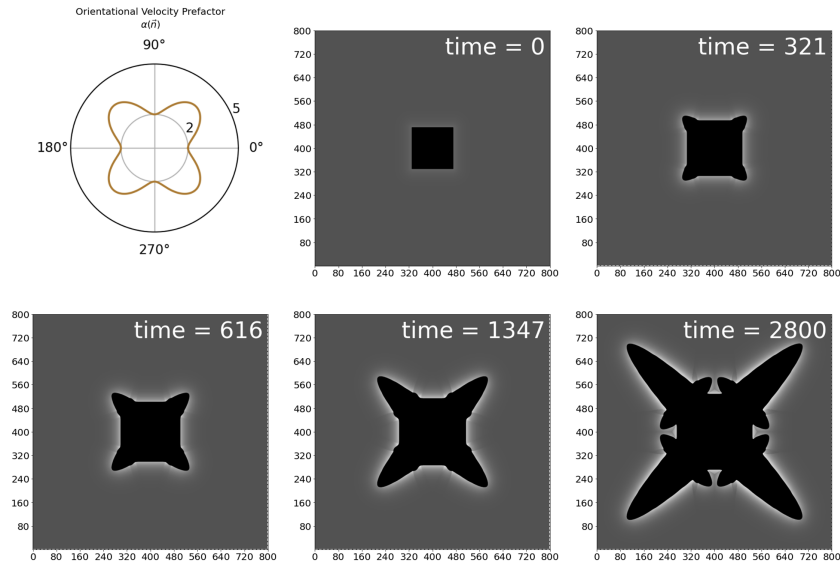
Figure 5-5: A simulation of the growth of a square hole in a film with unit thickness with $\beta = 3, \zeta = 6$.

5-6), anisotropy strength (see figure 5-7), and the strength of in-plane capillarity (see figure 5-8), which could vary depending on the cross-sectional profile of the rim.

Anisotropic Dendritic Dewetting in a Thinner Film
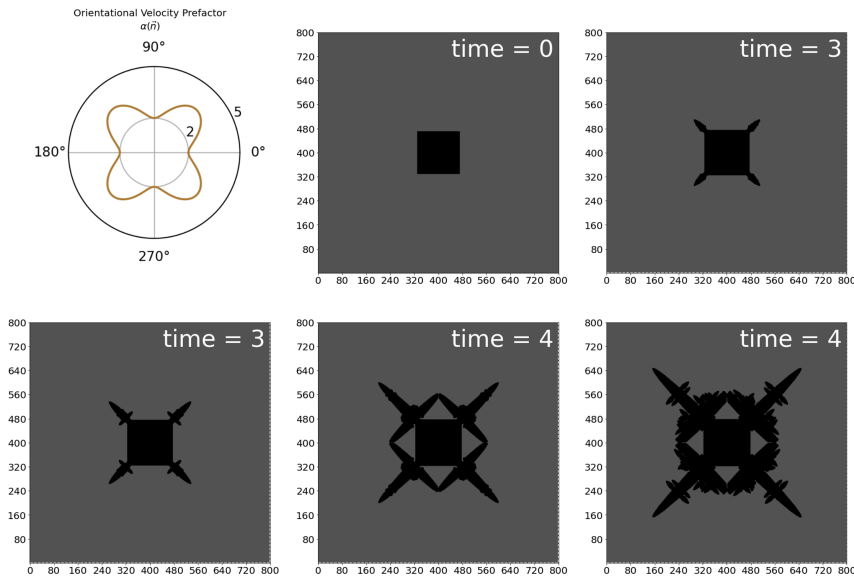
Figure 5-6: A simulation of the growth of a square hole in a film with thickness = 0.05 and $\beta = 3, \zeta = 6$.

Insufficiently Strong Anisotropy for Dendritic Dewetting
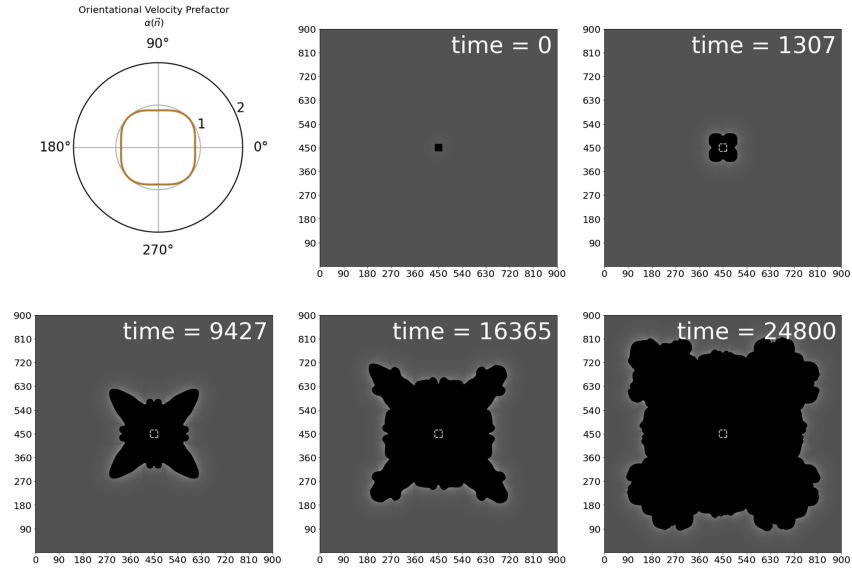
Figure 5-7: A simulation of the growth of a square hole in a film with weaker anisotropy ($\beta = \zeta = 1$, with $\vec{n}$ rotated by 45° to align the corners of α with the corners of the more anisotropic α used elsewhere) and thickness $= 1$. This anisotropy is not strong enough to sustain truly dendritic behavior.

Anisotropic Dendritic Dewetting with Reduced In-plane Capillarity
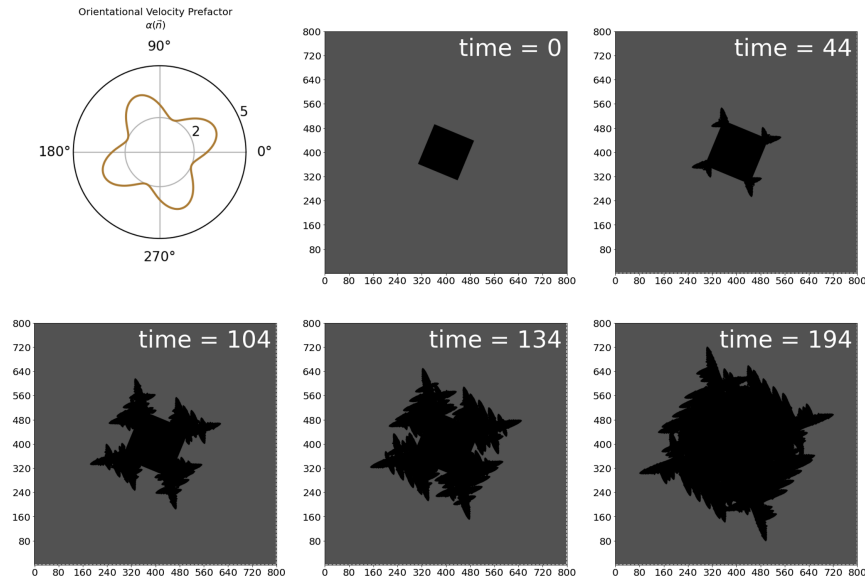
Figure 5-8: A simulation ($\beta = 3, \zeta = 6$) of the growth of a square hole in a film with unit thickness and reduced in-plane capillarity($\tau = \frac{1}{2}$). The hole and anisotropy function are also rotated by 22.5° to illustrate that $\alpha(\vec{n})$ is indeed determining dendrite orientation.

5.6 Connections to Solvability Theory

Understanding the Effect of Anisotropy
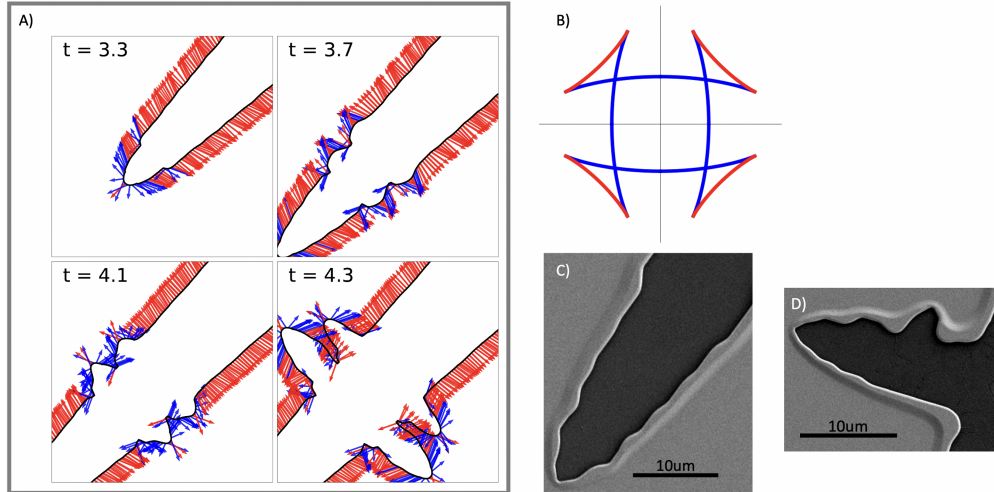
Figure 5-9: A) select frames from the same simulation as figure 5-6 with orientationally-determined characteristics overlaid to show the role of anisotropy. The convergence of $\alpha(\vec{n})$–characteristics at the tip and in regions which become side branches illustrates the role of anisotropy in fixing a steady–state tip morphology. B) A Cahn-Hoffman-like gradient construction created by connecting all characteristics emanating from a point. C) The corner of a square patterned in a 85nm thick 100 Ni film that has become unstable during growth induced by annealing at 950° C in a reducing ambient of 5% H_2, 95% N_2. Note the well-defined tip geometry and the jogging of the triple–line behind the tip. The sample had been annealed for a total of six hours when this image was taken. D) shows the formation of a side branch along the dendritic triple–line of another hole after 315 minutes of annealing.

We claim that employing the method of characteristics with a Cahn-Hoffman-type construction provides further insight into the role of anisotropy in dendritic dewetting. The method of characteristics is a relatively general approach to solving the initial value problem for PDEs. It produces curves, called characteristics, that emanate from the initial surface and project it forward in time; see Refs. [115, 116] for relevant overviews. We posit that the existence of an experimentally observed steady–state tip geometry with finite in-plane curvature implies that a region of the tip has characteristics which are parallel and of equal length. Furthermore, we contend that the fundamental arguments of solvability theory must also apply to dewetting systems that exhibit dendritic behavior, namely that the steady–state

geometry is a configuration-space attractor. This implies that there exists a set of geometries neighboring the steady–state geometry in configuration-space which have regions of finite, positive in-plane curvature with converging characteristics. We have shown above that in systems with isotropic and weakly anisotropic $\alpha(\vec{n})$, these criteria are not met. Furthermore, because $\alpha(\vec{n})$ is a simple multiplicative prefactor to triple–line velocity in our model, we hypothesize that the way in which it modifies the triple–line's characteristics can be qualitatively explored by examining the characteristics the triple–line would have if $v(\vec{x}, t) = \alpha(\vec{n}(\vec{x}, t))$. This simplification yields linear characteristics, as demonstrated in [115]. These characteristics, scaled appropriately in length, point to what would be the future location of the triple–line, if it were evolving under purely orientationally-dependent velocity. We illustrate this by overlaying these characteristics onto the profile of a simulated dendrite tip, see figure 5-9 A), to get a qualitative idea of anisotropy's contribution to the system's behavior. These characteristics are color-coded to match the velocity gradient construction in 5-9 B), the convex part of which corresponds to the kinetic Wulff shape of our velocity function and the ears of which correspond to orientations which are kinetically unstable over long time, see [58, 79] for a detailed explanation. We see that the tip of the dendrite has converging characteristics, which correspond to the lower left ear of our gradient construction. The convergence of these characteristics shows that velocity anisotropy is driving the persistence of a steady–state tip morphology that in-plane capillarity would otherwise blunt, fulfilling the reframed solvability criteria given above. Although not a rigorous proof, this graphical construction provides plausibility to the hypothesis that the presence of ears in the gradient construction of $\alpha(\hat{n})$ is a necessary, though likely insufficient, requirement of solvability for dewetting systems. The formation of side branches can be understood in a similar way, starting with the observation that, because the rim further away from the tip has been retracting for more time, the dendrite must, on average, get wider with increasing distance from the tip. We see, however, in both simulation and experiment (figure 5-9 C)), that the dendrite accommodates this constraint through the formation of in-plane jogs created through kinetic faceting. Figure 5-9A) highlights how these jogs create

alternating regions of diverging and converging characteristics. This behavior is analogous to the "varifolds" in minimal anisotropic surfaces introduced by Taylor [117, 118]. In the absence of rim height and in-plane curvature considerations, we would expect those parts with converging characteristics to get ahead of the neighboring areas with diverging characteristics and form new branches. Instead, side branches only form when this effect, coupled with the arc-length instability associated with regions of high in-plane curvature, is strong enough to overcome the stabilizing effect of in-plane capillarity.

5.7 Discussion

In analogy to the original analysis of dendritic solidification by Mullins and Sekerka, in solid–state dewetting the arc length instability is driven by enhanced dissipation of excess free energy at areas of high in-plane curvature. Specifically, in areas of positive curvature, the retraction of the triple line creates new arc length through which mass rejected from the triple line can diffuse. This is in contrast to areas of zero or negative curvature where mass rejected from the triple line accumulates into an ever-thickening rim, reducing the driving force for retraction. Again, in analogy with Mullins and Sekerka, in the absence of an energetic term that counteracts high in-plane curvature, the dissipative advantage of high curvature areas is sufficient to drive the formation of sharply pointed, needle-like dendrites. The absence of in-plane capillarity is non-physical, and the addition of a term accounting for the gradient in in-plane curvature from the hole–side to the film–side of the rim is sufficient to entirely suppress dendritic behavior. To regain dendritic behavior, as in the case of solidification, the introduction of anisotropy is necessary. Motivated by experimental findings in the literature that the retraction velocity of the triple–line can be highly orientationally dependent, our numerical simulations multiply the simple isotropic velocity by an orientationally dependent prefactor, $\alpha(\vec{n})$. For $\alpha(\vec{n})$ with sufficiently hard anisotropy, this simple change restores dendritic behavior, and our simulations qualitatively match key experimental findings, including jogs in the triple–line that

give rise to side branches. We also show that the role of anisotropy can be graphically illustrated using the method of characteristics.

5.8   Conclusions

Solidification and solid-state dewetting share phenomenology that produces dendritic evolution for some materials parameters. In each case, regions of high curvature accelerate the dissipation of excess free energy. This curvature effect is necessary but insufficient to explain observed dendritic behavior during solid-state dewetting. Our results suggest that coupling this instability with crystalline anisotropy produces dendritic morphologies. We have also shown that, although anisotropic surface energies and diffusivities interact in complicated ways, a simple treatment that combines their effects into a single orientationally dependent pre-factor to the triple–line velocity plausibly explains the core features of dendritic dewetting. In our model, we have identified the functional form of this anisotropy, the thickness of the initial film, and the magnitude of the effective line tension accounting for the gradient of in-plane curvature over the rim as the three factors controlling dendritic behavior and morphology. Increased film thickness and line tension broaden the tip of the dendrite, while the effects of anisotropy are more nuanced. In our simulations, we find that, in order for dendritic dewetting to occur, anisotropy must be sufficiently strong to overcome in-plane capillarity. This suggests that solvability theory from the solidification literature can be used to understand dendritic dewetting and is also consistent with our heuristic that—for solid-state dewetting—a steady–state tip must contain a region of converging $\alpha(\vec{n})$–characteristics.

Chapter 6

Conclusions

As stated at the beginning of this document, the goal of this thesis work was to develop a more predictive understanding of solid-state dewetting in systems with anisotropic properties. As a problem which is both deeply complex and well-studied, it seemed clear from the beginning that new insights into dewetting behavior were likely to come from the intersections of different scientific disciplines and viewpoints. It is therefore not a coincidence that this thesis features work of experimental, computational, and theoretical character and examines the behavior of strikingly disparate materials systems. Each of these efforts provided unique insights, with interesting results and puzzles from one approach providing information and inspiration for the others.

6.1 Main Results

The main thrust of this work was the development of a new simulation method which allowed for the faithful modeling of the anisotropic Mullins equation for systems with strongly anisotropic properties. This method, outlined in chapter 2, is based on the level-set method and synthesizes many ideas from the fields of materials physics, applied mathematics, and computational materials science to realistically encode the physics of solid-state dewetting into the level-set framework. By making use of tech-

niques in the level-set method literature such as narrow-banding, velocity extension, ghost values, and redistancing, in addition to improvements we developed ourselves, such as adaptive time-stepping tied to volume conservation and energetically penalizing $\nabla^2\phi(\vec{x})$, we were able to create a simulation framework which preserved the traditional strengths of level-set simulations—sharp interfaces and natural handling of topological changes—and mitigates their traditional weaknesses—poor computational performance, poor volume conservation, and poor numerical stability when modeling high-order differential equations. This method was validated against known analytical and numerical solutions for isotropic dewetting phenomena in addition to observed experimental behavior in strongly anisotropic systems. This framework was used to study edge retraction, wire stability, and hole growth and the dependence of these behaviors on surface energy and surface self-diffusivity anisotropy. These computational studies were paired with experiments carefully designed to probe the same behavior in complementary ways.

Beginning with edge retraction, these simulations recovered the experimental observation that films with stable top facets are still capable of exhibiting valley formation. This behavior is seen in experiments on Ni (110) films but couldn't be explained using previous modeling techniques. Our simulations reproduce not only this behavior but also its dependence on ambient conditions, using measured values for relative surface free energy densities and σ. Additionally, these simulations showed that surface energy anisotropy alone can account for the morphology of these retracting rims' leading sides as well as the elongation of the top facet relative to the Winterbottom shape.

These simulations also recovered, in surprising detail, the orientational dependence of Ru nanowire stability on orientation. In fact, the videos produced by these nanowire simulations aided in developing the hypothesis, which was experimentally confirmed months later, that ovulation and the Rayleigh instability act together along a wire's full length. The other experimental findings from the Ru nanowire work were equally striking, with the stability of these wires having a remarkably strong dependence

on orientation. In both experiment and simulation, wires aligned along stable $<11\bar{2}0>$ directions seemed impervious to both the Rayleigh instability and ovulation and exhibited dramatic length contraction over the same length of time the unstable wires took to break up. Furthermore both experiment and simulation showed that the orientation dependence of wire stability was mostly saturated within $5°$ of offset from $<11\bar{2}0>$ orientations. These results show the extreme importance anisotropy could have in the reliability of single-crystal devices, and they illustrate the potential utility of our LSM framework in studying and designing for device reliability.

One of the most striking behaviors observed in dewetting is the corner instability followed by dendritic dewetting. Simulations of this behavior were shown in chapter 2. Using DFT-calculated values for the surface energy of Ni's 3 lowest-energy facets, an initially circular hole in a (100) film was shown to first grow to it's kinetic Wulff shape, subsequently undergo the corner instability, and finally begin to develop dendritic characteristics, including the beginnings of side branches. Such behavior was recovered using both isotropic and anisotropic surface self-diffusivities, though clear qualitative differences in behavior were apparent between the two cases, suggesting that further simulations can be used to tease apart the effects of diffusivity and surface energy. This behavior was also examined from a theoretical perspective in chapter 5, drawing insight from the extensive literature on dendritic solidification and viscous fingering. This work hinged on a simplified model of dewetting which embeds the most essential characteristics of dewetting edges into a set of coupled two-dimensional equations. Among other simplifications, this model combined the orientational dependencies of surface energy density and surface self-diffusivity into a single quantity, allowing the effect of anisotropy to be studied more generally. Thus simplified, dewetting behavior becomes at least somewhat analytically tractable, and a Mullins-Sekerka-type analysis was conducted on this model system, in addition to simple LSM simulations of these simplified governing equations—it is worth reiterating that these simulations are entirely distinct from those introduced in chapter chapter 2 and used in chapters 3, and 4. These analyses revealed, in analogy to dendritic solidification, that dendritic dewetting is only possible in the presence of

sufficiently strong anisotropy. We extended the analogy further and hypothesized that systems which exhibit dendritic dewetting behavior must satisfy a solvability criterion which mirrors the microscopic solvability criterion used to explain dendritic solidification. We provided support for this conjecture by using the method of characteristics to illustrate that anisotropy can push a dewetting system toward dendritic morphology with a steady-state geometry.

6.2 Looking Forward

Though we have made significant progress in developing a more predictive understanding of dewetting, there is certainly more work to be done. As outlined in chapter 2, there are several areas of our simulation framework which could be improved upon, including a more efficient implementation of coupled fast marching and velocity extension algorithms and development of a smoothing operator which more selectively targets non-physical sawtooth surfaces. Ironically, the ability to model systems with arbitrarily anisotropic properties raises a host of questions about how to model anisotropy less arbitrarily. Thus, much more work is also needed in developing realistic physical models of anisotropic surface energy density and surface self-diffusivity.

There are also many more experiments to be conducted, including work on electromigration in single-crystal nanowires, further exploration of the effects of CO reducing gas on the dewetting behavior of Ni films, more careful study of nanowire stability at junctions and intersections (see appendix C), and testing of our solvability hypothesis in systems with weakly anisotropic and isotropic properties. Branching out from fundamental explorations, the ability to predict dewetting behavior computationally should aid in developing dewetting-based nanofabrication techniques, with applications in areas like photonics and sensing.

Appendix A

Designing $\vec{\xi}(\hat{n})$

A recurring theme in this thesis is the use of $\vec{\xi}(\hat{n})$ which embody strong crystalline surface anisotropy. In this appendix, I will briefly overview how such $\vec{\xi}(\hat{n})$ were constructed, how their functional form can be physically interpreted, and what improvements can be made in the future.

A.1 Defining the Problem

As stated in the introduction of this thesis, surface free energy density is a complex function of temperature, ambient, and orientation. Existing models of these effects tend to focus on orientations with small offsets from stable orientations. Several such models are discussed in [119], and we made attempts to develop $\gamma(\hat{n})$s based on these models. The difficulty with these models is that they contain many parameters accounting for different entropic and energetic factors. Given the difficulty of measuring surface free energy densities for non-equilibrium orientations, such complex models present an over-fitting problem. Furthermore, such models tend to focus on describing the properties of a single surface and it's neighboring orientations, meaning that $\gamma(\hat{n})$s naïvely assembled from models of an equilibrium shape's constituent surfaces are not guaranteed to be smooth or even continuous. Attempts to fix and smooth the resulting $\gamma(\hat{n})$s lead to complex functions which lose physical interpretability and,

for whatever it's worth, just don't look quite right. This begs the question, is modeling $\gamma(\hat{n})$ in this way the best approach? In most contexts, the surface free energy density, $\gamma(\hat{n})$, though it contains the same information as $\vec{\xi}(\hat{n})$, is thought of as the more fundamental or natural of the two quantities. Working from this point of view, it is natural to try and define a $\gamma(\hat{n})$ for a system and compute $\vec{\xi}(\hat{n})$ as needed. In keeping with this thesis's overarching goal theme of trying to reframe problems in more tractable ways, we take a different approach.

A.2   Starting with $\vec{\xi}(\hat{n})$

Rather than starting with $\gamma(\hat{n})$ and computing $\vec{\xi}(\hat{n})$, we have found that it is far better to directly construct $\vec{\xi}(\hat{n})$ and compute $\gamma(\hat{n})$ if desired. The foundation for this approach is the observation that, if a system's surface free energy density were defined such that $\gamma(\hat{n})$ was always equal to the energy of the energy minimizing linear combination of facets (effectively the energy density corresponds to that of vicinal surfaces), the resulting $\vec{\xi}(\hat{n})$ would be composed of a few discontiuous points. In this scenario, for $\hat{n}$ corresponding exactly to equilibrium surfaces, $\vec{\xi}(\hat{n}) = \hat{n}\gamma(\hat{n})$. For all other orientations, $\vec{\xi}(\hat{n})$ corresponds to the vertex connecting the relevant facets or, in three dimensions, possibly the center of the edge connecting two relevant facets. Starting with this set of discrete points, it is relatively straightforward to computationally construct a function which smoothly connects them. In some sense, the problem is one of simply parameterizing the surface of a polygon or polyhedron with some degree of corner rounding. If a $\vec{\xi}(\hat{n})$ with orientational spinodes is desired, the corners of these shapes are given negative radii of curvature.

A.3   Example Mathematica Code

The following code is a tidy example of how a $\vec{\xi}(\hat{n})$ corresponding to a simple square could be constructed, following the logic outlined above.

```
SetDirectory[NotebookDirectory[]];

roundingRadius = 0.1;

orientationParser4Fold[vx_, vy_, energy_]:=
Module[{orientations, energies},
orientations =
DeleteDuplicates[{{vx, vy}, {vx, −vy}, {−vx, vy}, {−vx, −vy}}];
energies = ConstantArray[energy, Length[orientations]];
{orientations, energies}]

normedVecs = {{1, 0}, {0, 1}};

avgEnergies = {1, 1};

startingFaces = Table[Append[normedVecs[[i]], avgEnergies[[i]]],
{i, 1, Length[avgEnergies]}];

temp = orientationParser4Fold@@@startingFaces;

unnormedNormals = Flatten[temp[[;;, 1]], 1];
energies = Flatten[temp[[;;, 2]]];

normedNormals = (#/Norm[#])&/@unnormedNormals;

allPlanes = Table[Append[normedNormals[[i]], energies[[i]]],
{i, 1, Length[normedNormals]}];

cusps = allPlanes;

coeffs = Table[Symbol[a <> ToString[i]], {i, Length[allPlanes]}];

faces = −allPlanes[[;;, 1;;2]];

nodes =
Union[Append[#, 1]&/@
```

```
Quiet[Cases[LinearSolve[Most/@#, −Last/@#]&/@

Subsets[allPlanes, {2}], _List]]];

vertices = DeleteDuplicates[Select[nodes, Chop[Min[allPlanes.#]]>=0&],

Equal];

vertices = DeleteDuplicates[vertices/.n_?NumericQ/;Abs[n] < 1*^-5 → 0,

Equal];

roundedPlanes = allPlanes;

roundedPlanes[[;;, 3]] = roundedPlanes[[;;, 3]] − roundingRadius;

roundedNodes =

Union[Append[#, 1]&/@

Quiet[Cases[LinearSolve[Most/@#, −Last/@#]&/@

Subsets[roundedPlanes, {2}], _List]]];

roundedVertices =

DeleteDuplicates[Select[roundedNodes,

Chop[Min[roundedPlanes.#]]>=0&], Equal];

roundedVertices =

DeleteDuplicates[roundedVertices/.n_?NumericQ/;Abs[n] < 1*^-5 → 0,

Equal];

roundedVerts = roundedVertices[[;;, 1;;2]];

verts = vertices[[;;, 1;;2]];

normedVerts = verts/Map[Norm, verts];

normedRoundedVerts = roundedVerts/Map[Norm, roundedVerts];

thetaStep = 1*^-3;

thetas = Range[−thetaStep, 2π + thetaStep, thetaStep];

xiNiTestSolvedEdges[nx_, ny_]:=
```

```
Block[{v = {nx, ny}, thresh = 0.99, factor, faceProds, vertProds,
faceLoc, vertLoc, vertsSorted, alphaVert},
faceProds =
NMinimize[{Total[coeffs * allPlanes[[;;, 3]]],
Total[coeffs * allPlanes[[;;, 1;;2]], 1] == v&&
LogicalExpand[AllTrue[coeffs, # ≥ 0&]]}, coeffs][[2]]//Values;
vertProds = #.v&/@roundedVerts//N;
faceLoc = Ordering[faceProds][[-1]];
vertsSorted = Ordering[vertProds];
vertLoc = vertsSorted[[-1]];
factor = Min[Max[(faceProds[[faceLoc]] − thresh)/(1 − thresh), 0], 1]^
2;
allPlanes[[faceLoc, 1;;2]] * allPlanes[[faceLoc]][[3]] * factor+
(1 − factor) * (roundedVerts[[vertLoc]] + roundingRadius * v)
]

xis = xiNiTestSolvedEdges[Cos[#], Sin[#]]&/@thetas;

ListLinePlot[xis, PlotRange → {{−1.8, 1.8}, {−1.8, 1.8}},
AspectRatio → 1, PlotStyle → {Red, Thickness[0.005]}]
```
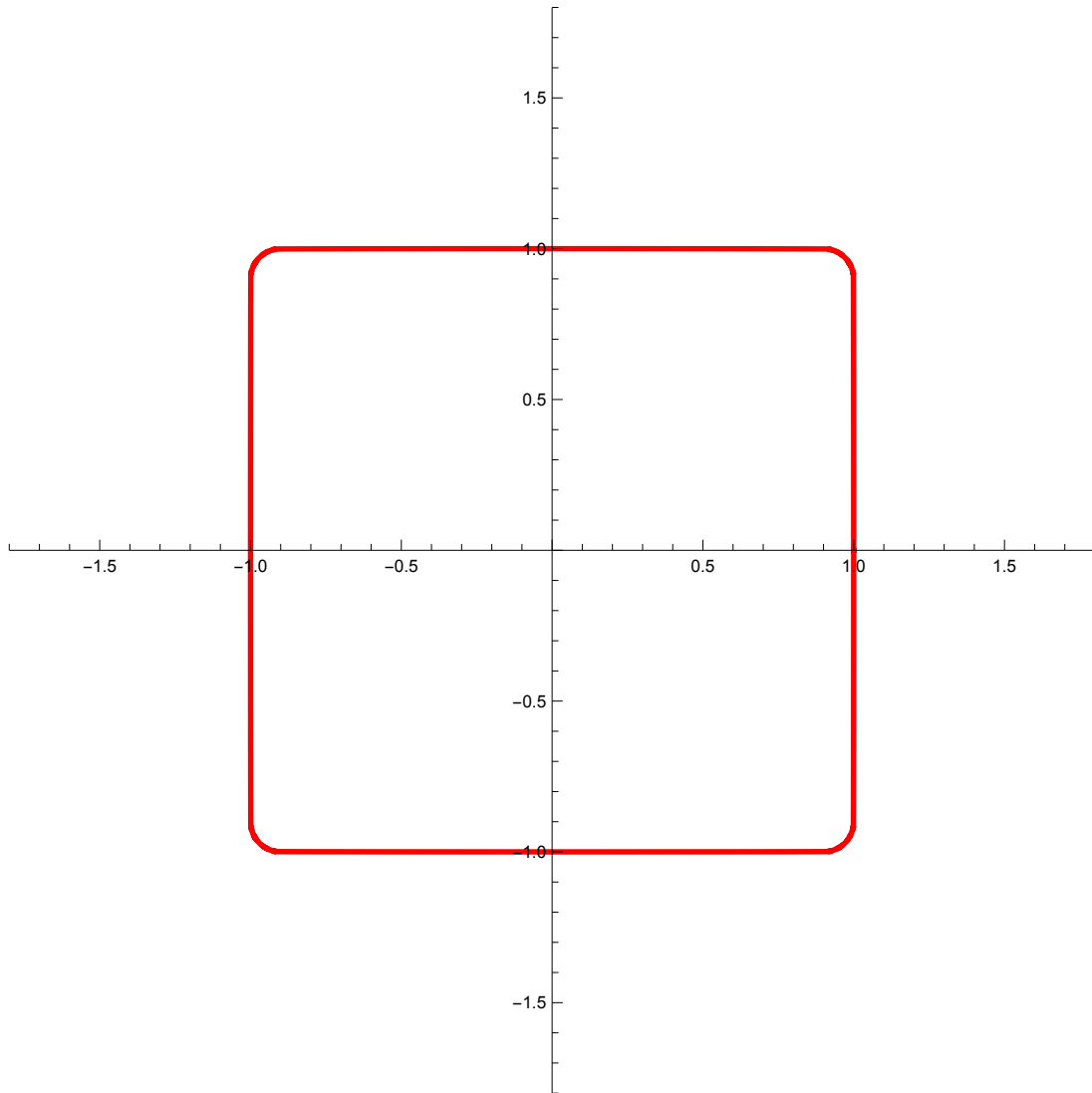
gammas = Table[{Cos[thetas[[i]]], Sin[thetas[[i]]]}.xis[[i]],

{i, 1, Length[thetas]}];

ListPolarPlot[{thetas, gammas}//Transpose, Joined → True]
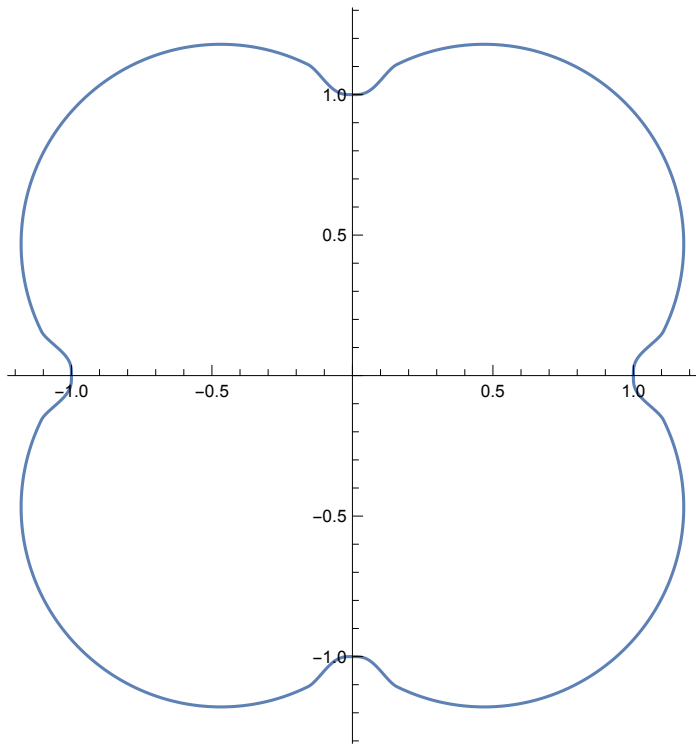
Appendix B

Notes on the Simulations in Chapter 5

B.1   Numerical Artifacts and Volume Conservation

As mentioned in the Comparison to Simulation section, the simulations presented in this work show some evidence of numerical grid effects. These effects are most apparent in isotropic simulations without effective line tension ($\tau = 0$). Our linear stability analysis shows that these simulations should produce infinitely sharp dendrites—and they do. However, there is a limit to the curvatures which the grid underpinning our simulations can resolve. Furthermore, the simulation can resolve higher curvatures along Cartesian directions. As a result, corners initially patterned in any orientation quickly turn toward the closest Cartesian direction. The addition of non-zero line tension greatly diminishes this effect, though it is not entirely eliminated. Figure 8 demonstrates that although $\alpha(\vec{n})$ does determine the direction of dendritic dewetting, side-branch formation is erroneously asymmetric. In simulations in which $\alpha(\vec{n})$ was chosen to have maxima offset from Cartesian directions by only a few degrees, the direction of dendrite propagation was biased toward the Cartesian directions. This suggests that further enhancements to our numerical methods, such as using adaptive regridding [120] or using a triangular mesh [121] rather than

a Cartesian grid are necessary, but the main features of dewetting phenomenology are clearly being captured. Of course, the governing equations being simulated here are already intentional simplifications, and a full-three dimensional simulation of the anisotropic Mullins equation would be necessary for full accuracy, as shown in chapter 2. Nevertheless, our results provide a framework for understanding and describing the phenomenology of dendritic dewetting. Another shortcoming of this simple simulation method is that volume is not conserved when rims from different regions of the triple-line run into each other and merge into wires, so the long-time behavior of side-branches is not correctly captured.

Appendix C

Miscellaneous Results

Over the course of this thesis work, we explored several other areas of research which, for one reason or another, have not yet been sufficiently investigated to merit a dedicated thesis chapter. In this appendix, we present a collection of interesting findings from this work which merit further investigation.

C.1 Additional Ruthenium Results

As part of our research on the stability of Ru nanowires, we also explored the dewetting behavior of other related geometries, such as wire intersections and junctions between strips of different dimensions. These were annealed under the same conditions as the Ru nanowires in chapter 4 and showed similar orientational dependence of stability.

C.1.1 Electrical Test Structures

One of the major motivations for our work on Ru nanowires was an interest from industry in next-generation single-crystal Ru interconnects. To better understand the electrical properties of these nanowires, in particular how the faceting induced by dewetting might increase conductivity, our collaborators at the University of Central

Florida designed and fabricated a test structure in which narrow single-crystal Ru lines were connected to large poly-crystalline Ru electrical pads. These connections were mediated by additional single-crystal lines of far greater width (500 nm). All single–crystal features were patterned from 5 nm–thick films. In the first batch of samples, the polycrystalline films were under a great deal of as-deposited stress which caused them to rupture and delaminate during annealing. This rendered the samples useless for electrical testing, so we instead annealed them to the point of significant dewetting to observe how the larger strips and the junctions between different strips behaved. AFM measurements show that our Ru films do not exhibit significant valley formation, but we repeatedly see that lines wider than ∼250 nm (for 5 nm–thick films) tend to bifurcate into wider lines. We believe that the mechanism of breakup is likely to be the formation of holes inside the strips which then lead to channel dewetting [97]. Uncovering the exact width which leads to bifurcation will require experiments with more granular variation in line width.

These experiments also show that a significant amount of dewetting occurs at the junction between the wider and narrower lines, often leading the narrower lines to pinch–off from the wider ones. This suggests that future designs could be improved by widening the narrower wire in the region of the junction, to allow the junction to dewet and facet without pinching off.
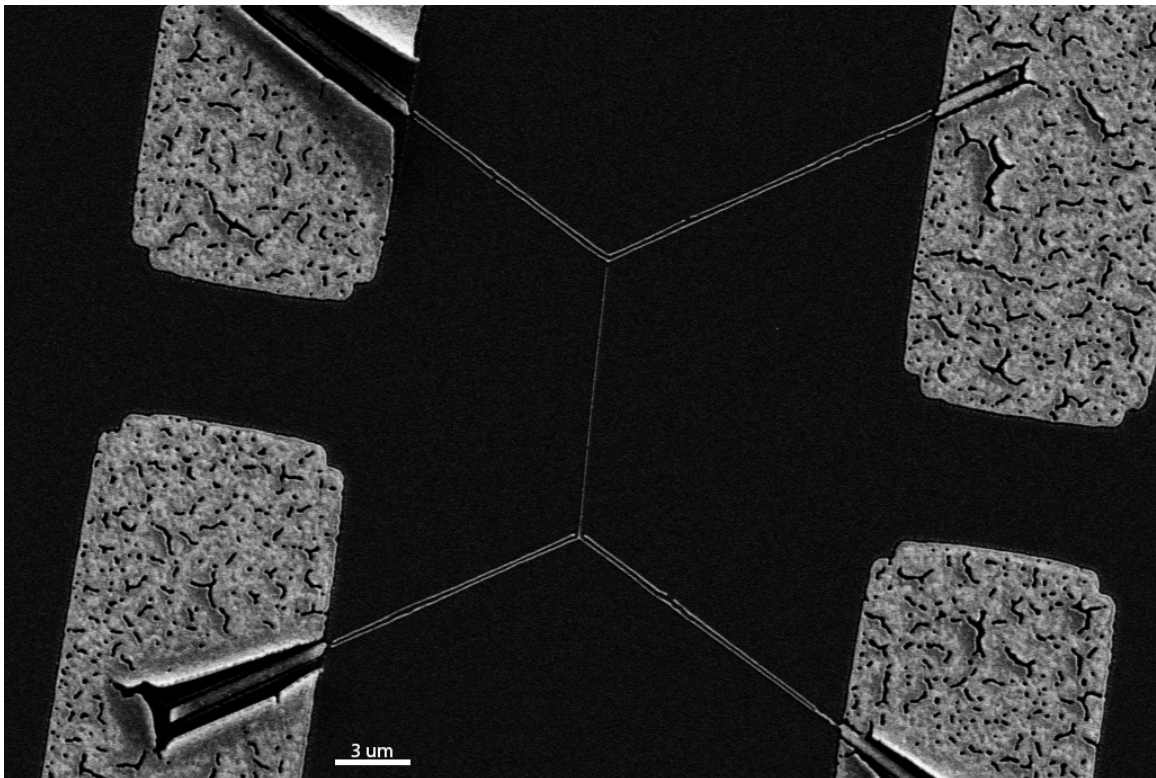
Figure C-1: This figure shows a wide view of a significantly dewetted electrical test structure. The wide lines leading to the center test line have bifurcated and the polycrystalline contacts have ruptured and partially delaminated.
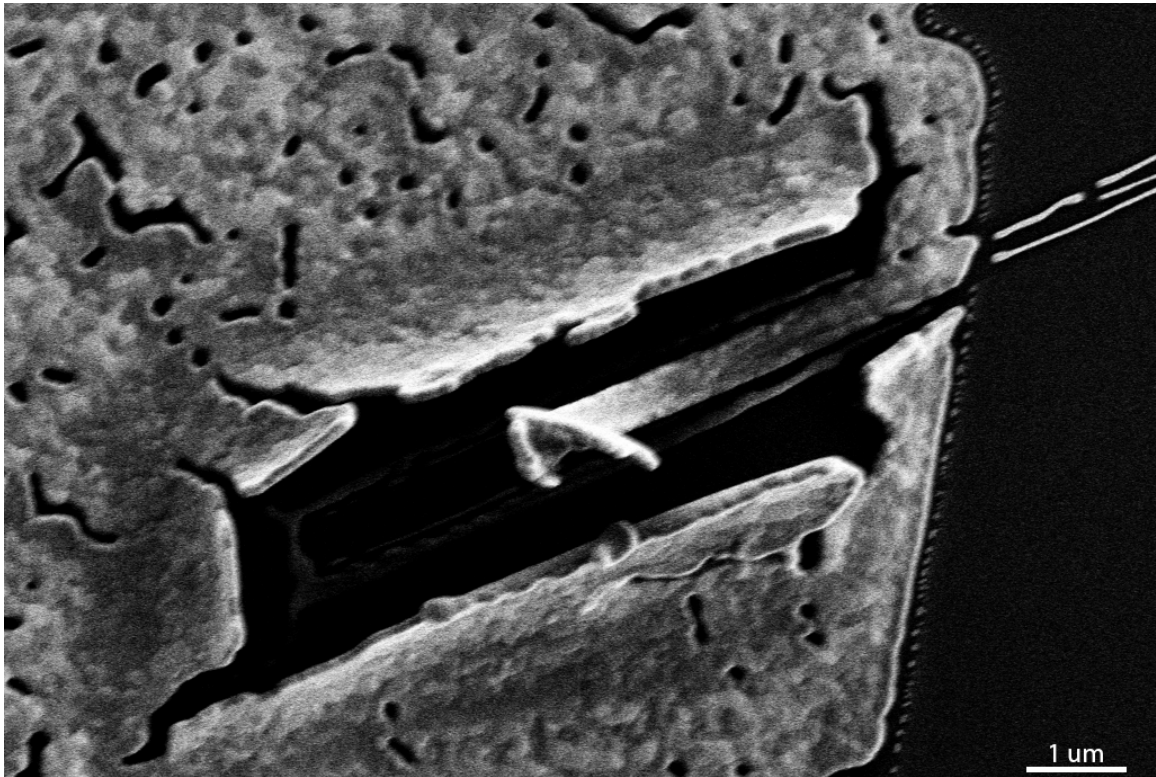
Figure C-2: A closer view of a ruptured and partially delaminated polycrystalline electrical contact
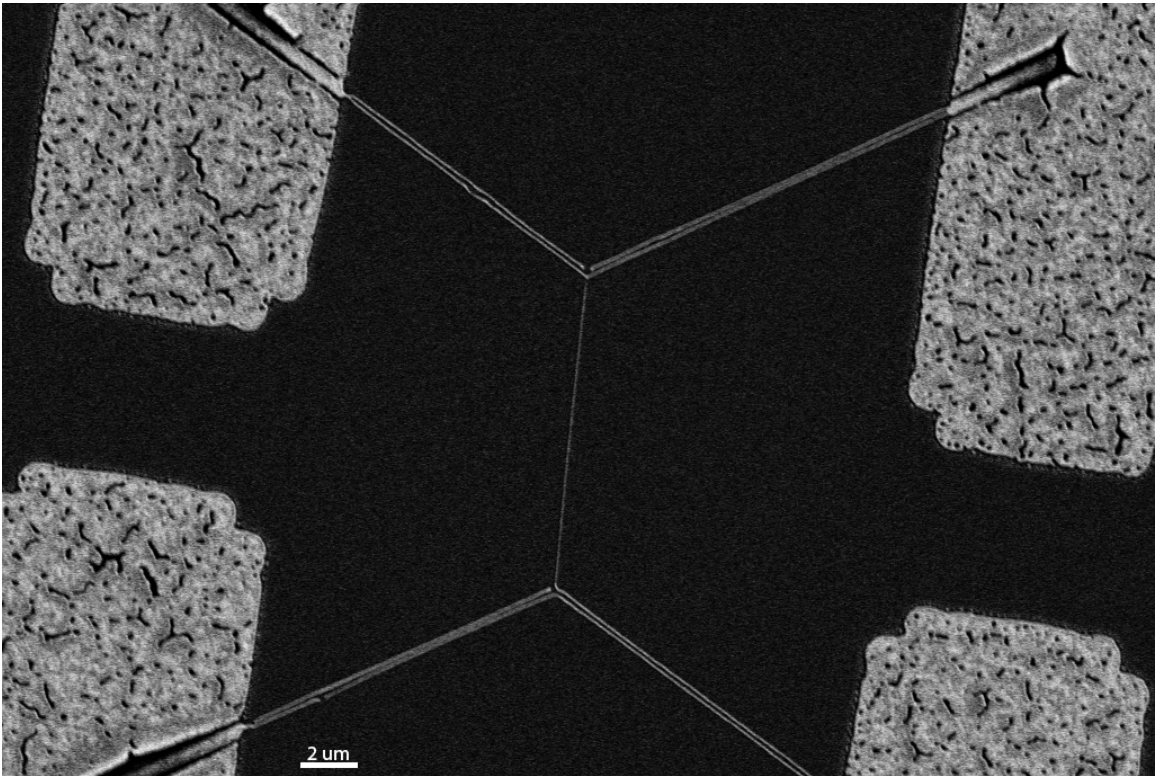
Figure C-3: A wide view of an additional electrical test structure
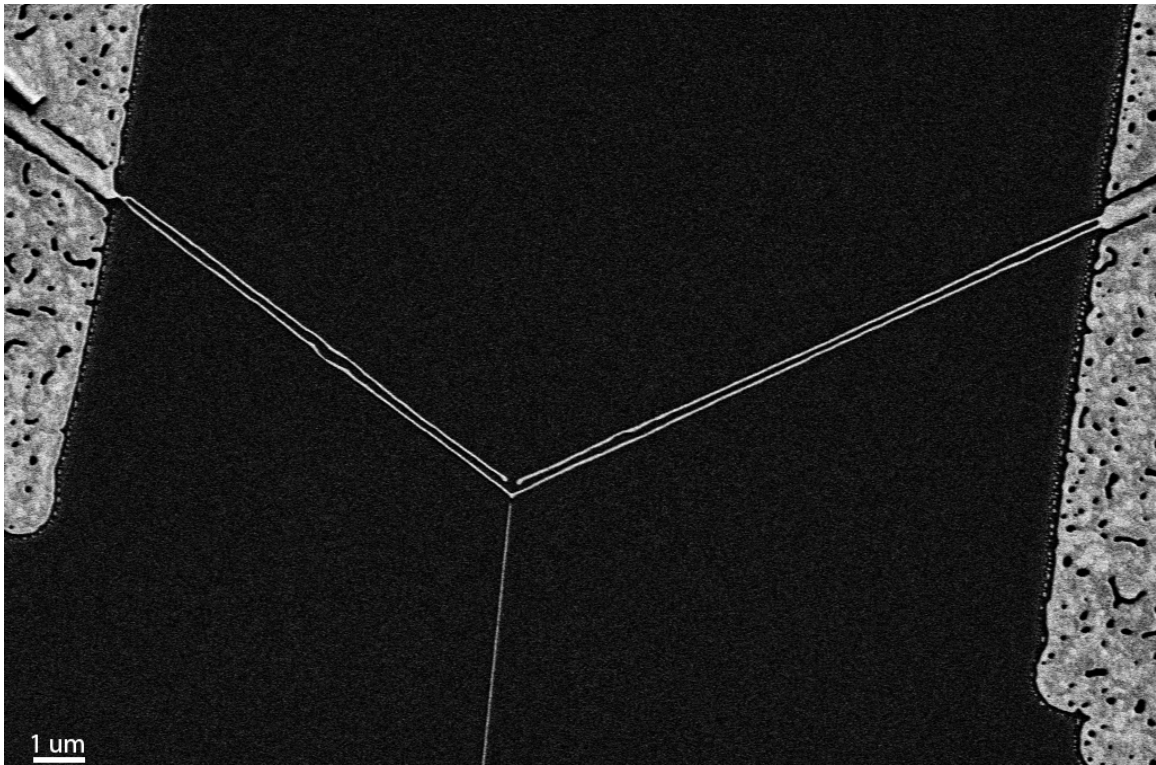
Figure C-4: A closer view of the structure shown in figure C-3 showing the junction between wide and narrow lines, with the wide lines having undergone bifurcation and the narrow line staying relatively stable. Material has pulled away from the junction, separating the two lines.
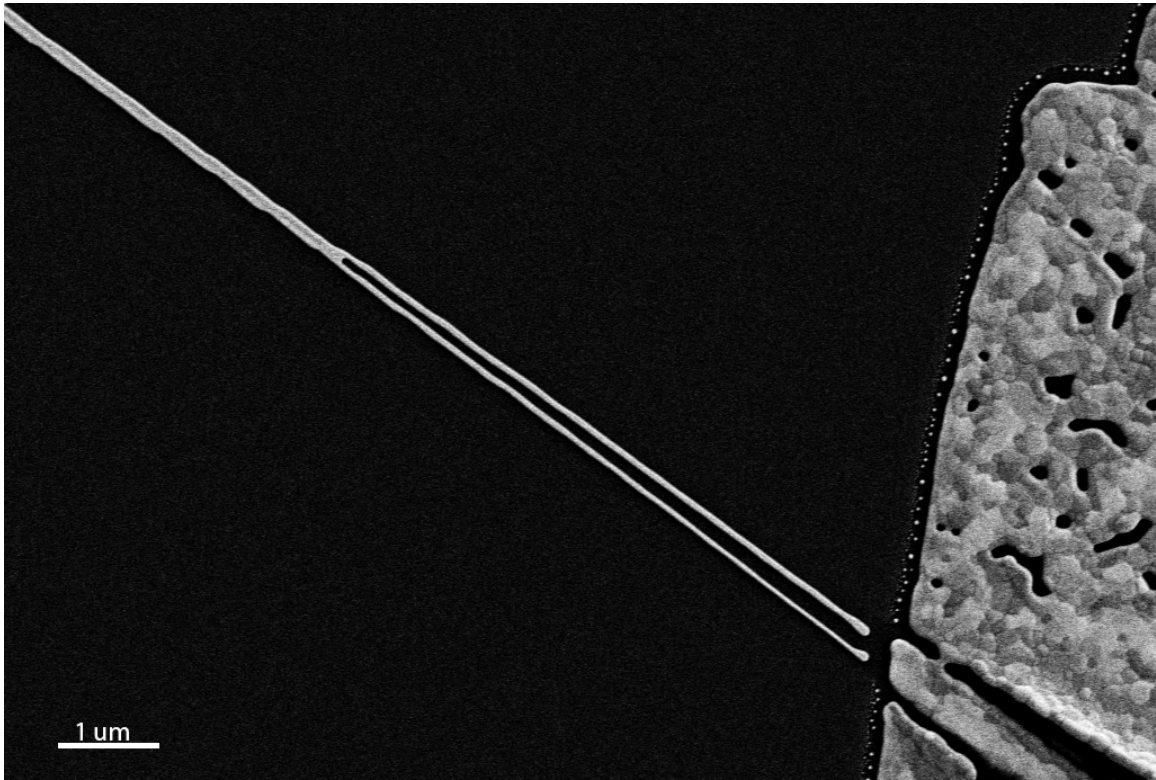
Figure C-5: This image shows a channel which has partially propagated through a narrowing wide line, leading to partial bifurcation. This is direct evidence that channel dewetting is playing a role in line bifurcation, rather than the bulk thinning mechanism alone.
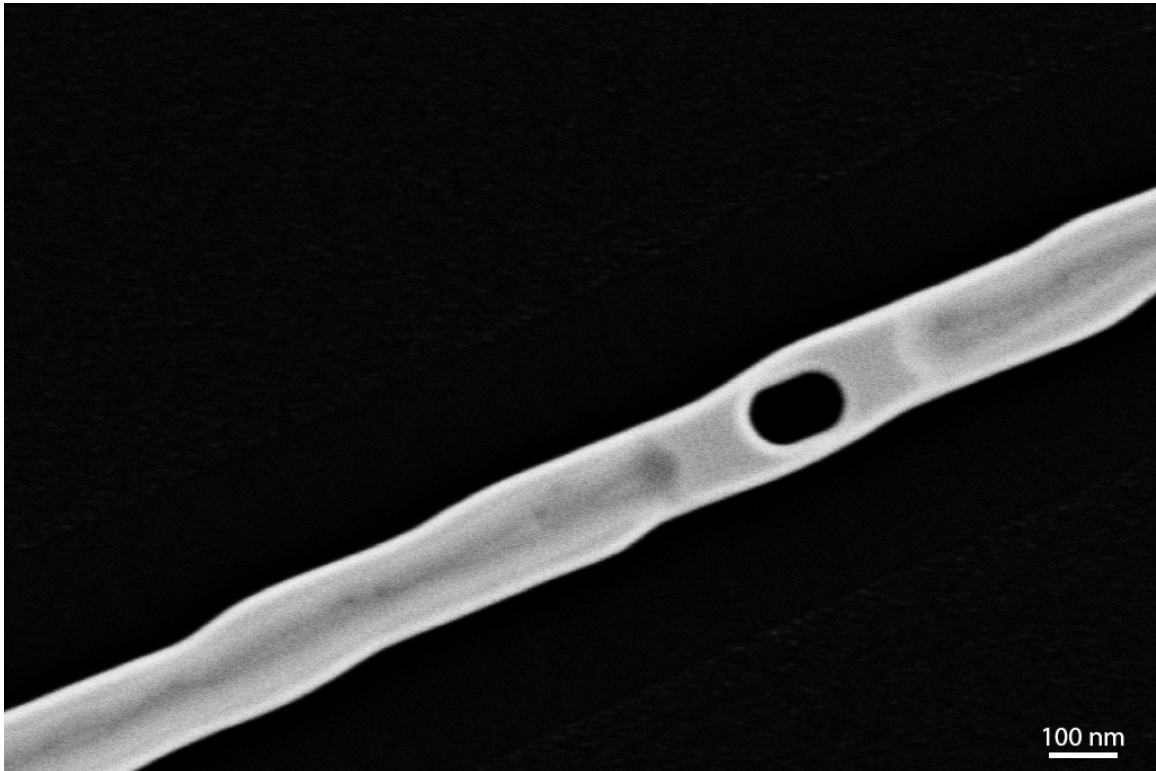
Figure C-6: We observed holes in many of the wide lines, at various stages of dewetting. It is our belief that hole formation coupled with channel dewetting is likely the primary mechanism by which wide lines bifurcate.
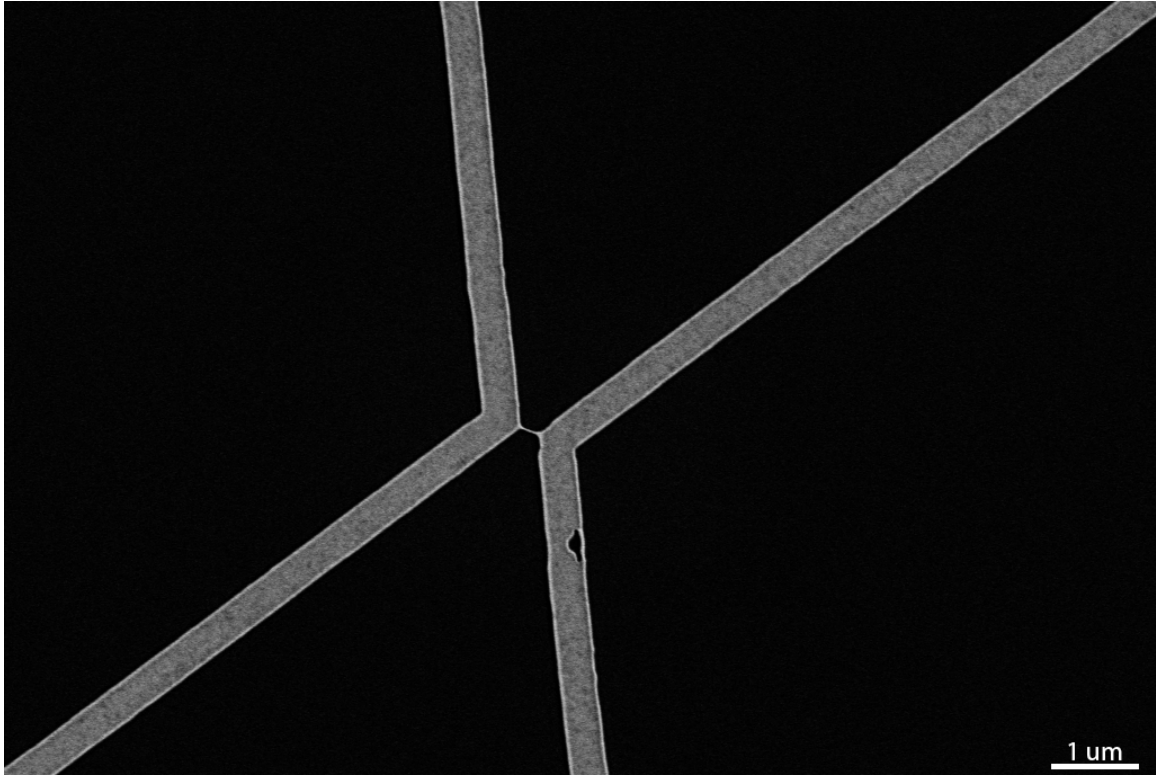
Figure C-7: A set of wider electrical leads (initially 500 nm–wide) at an earlier stage of dewetting
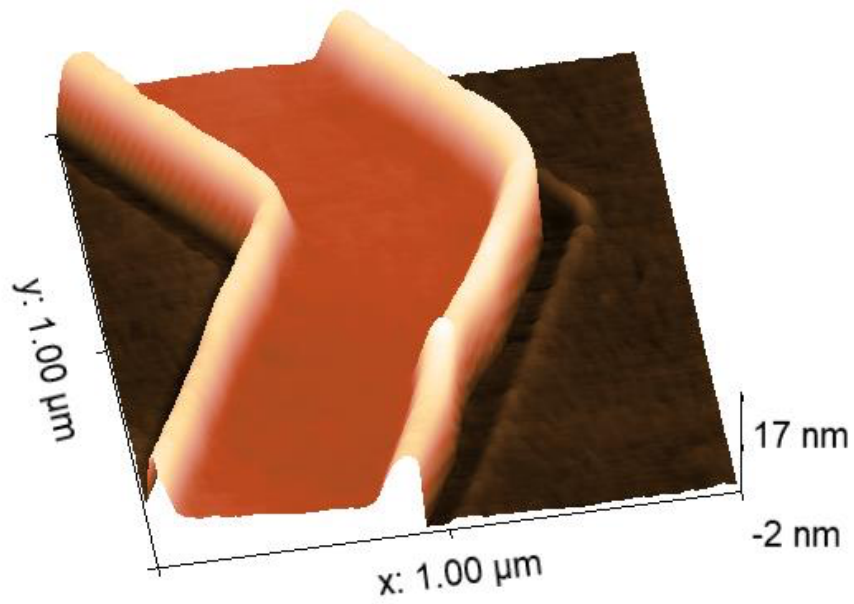
Figure C-8: An AFM scan of a set of lines similar to those seen in figure C-7.
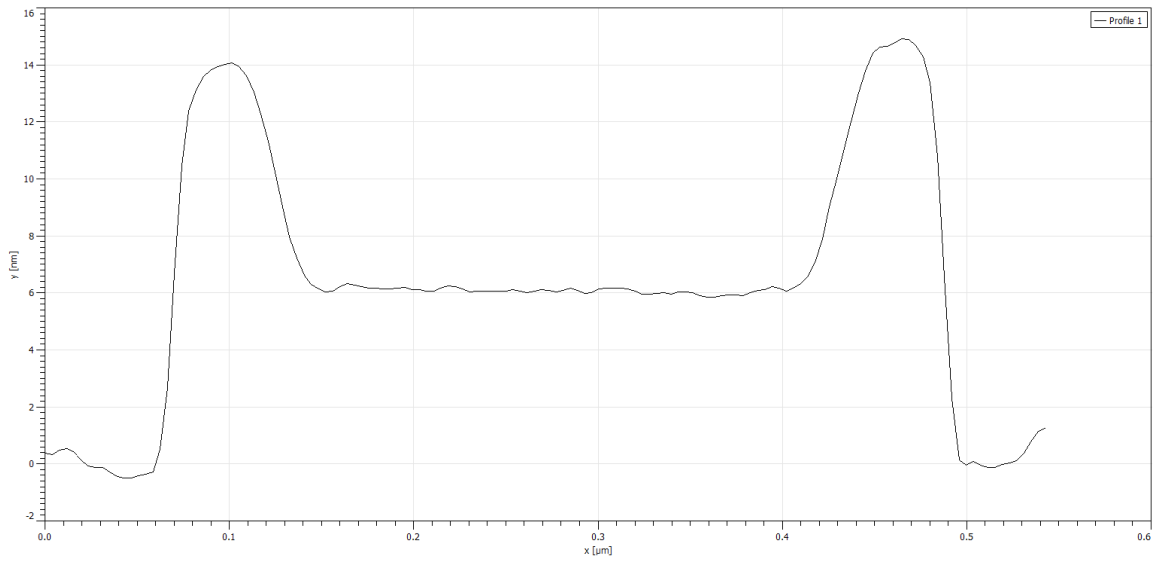
Figure C-9: A line scan extracted from the AFM data shown in figure C-8. This shows no evidence of valley formation.

C.1.2 Narrow Line Intersections

In addition to studying the junctions between lines of different widths, we also annealed samples featuring intersections of relatively narrow lines of the same width. The results of these experiments further showcase the twin roles of ovulation and Rayleigh-like modes in Ru nanowire breakup, as the point of intersection can nucleate instability. These structures were patterned from 5 nm–thick films.
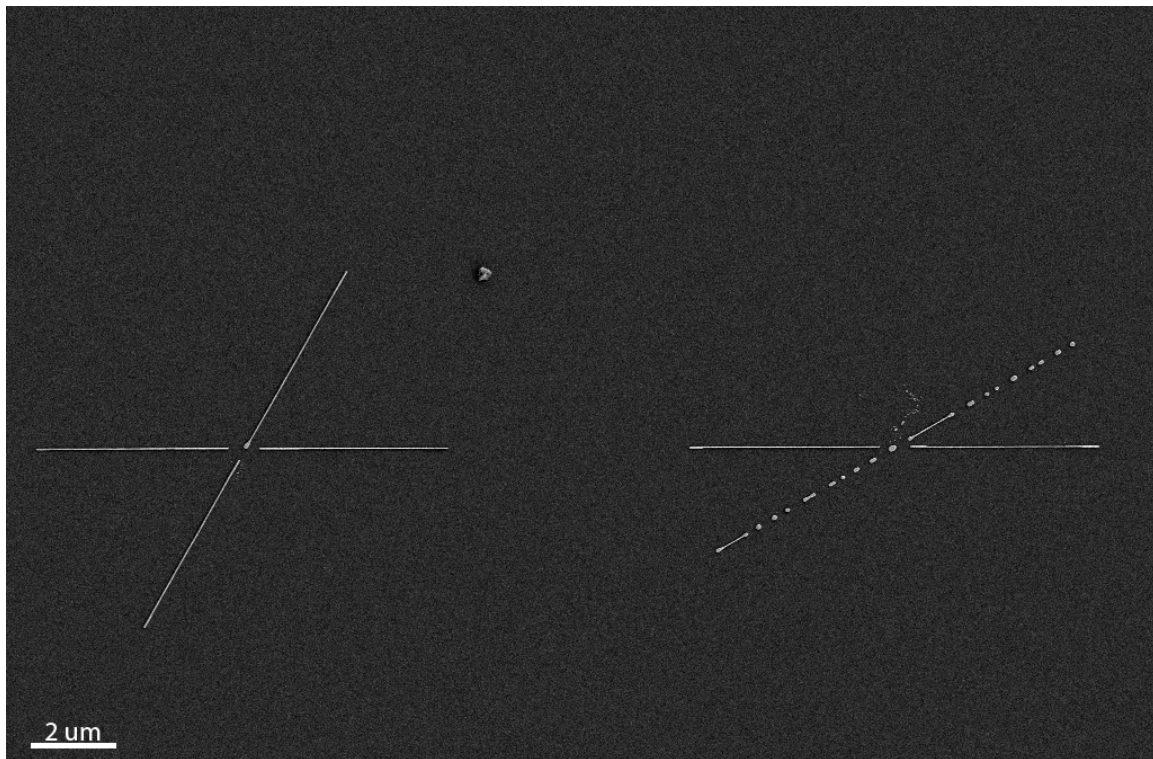
Figure C-10: Intersections of $\sim$70 nm–wide as–patterned lines. The left intersection is composed of two stable $< 11\bar{2}0 >$ lines while the right contains one stable and one unstable line.
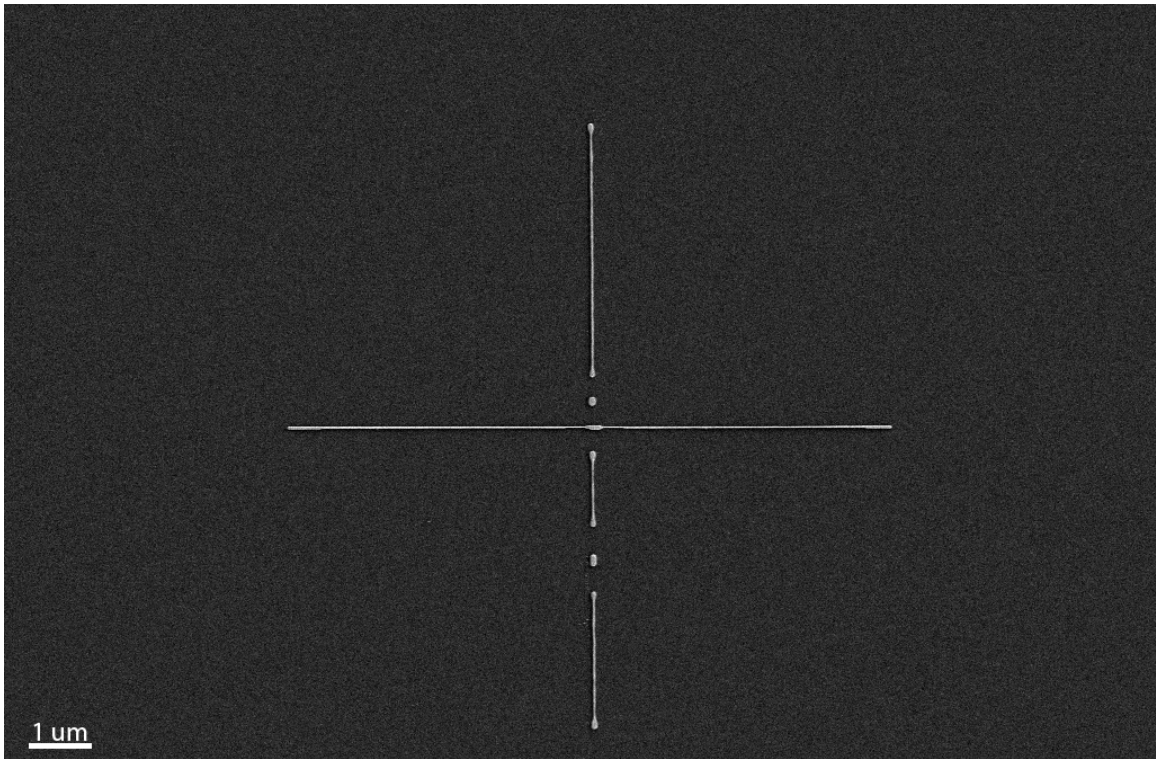
Figure C-11: Intersection of ~70 nm–wide as–patterned lines. The horizontal line is aligned along a stable $< 11\bar{2}0 >$ direction, and the vertical line is 30° offset from such an orientation.
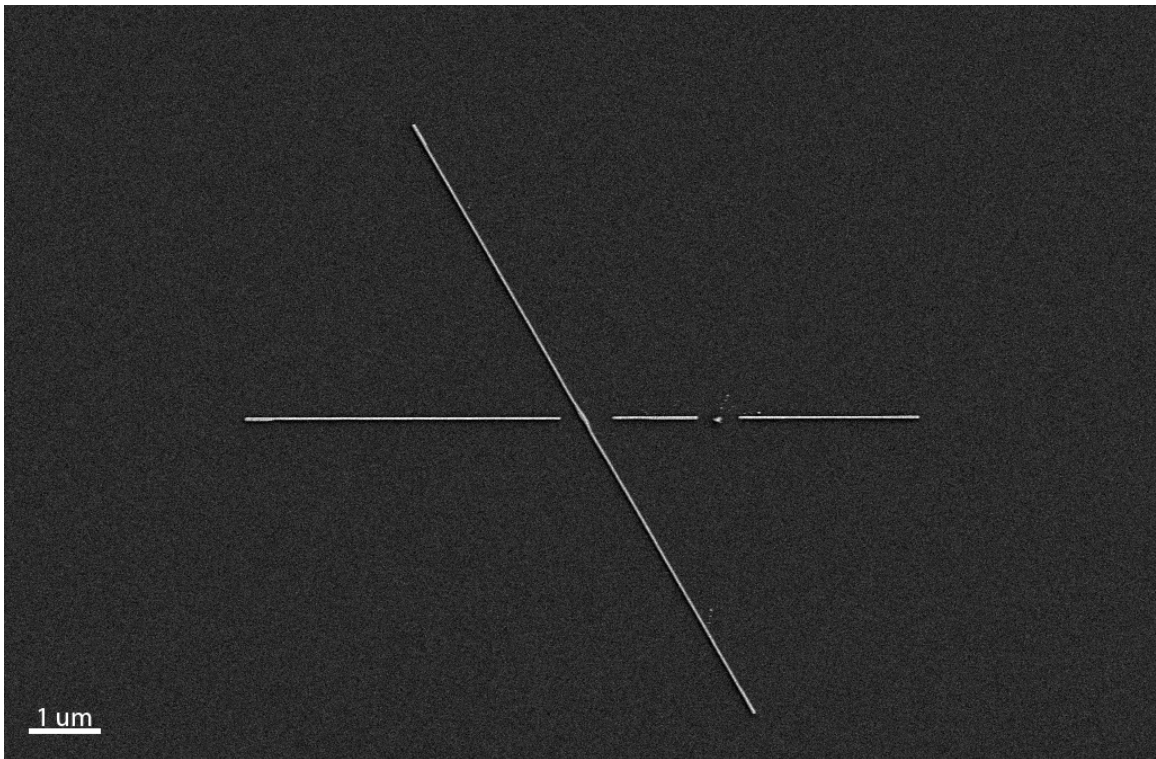
Figure C-12: Intersection of ~70 nm–wide as–patterned lines. Both lines are aligned along stable $< 11\bar{2}0 >$ directions.
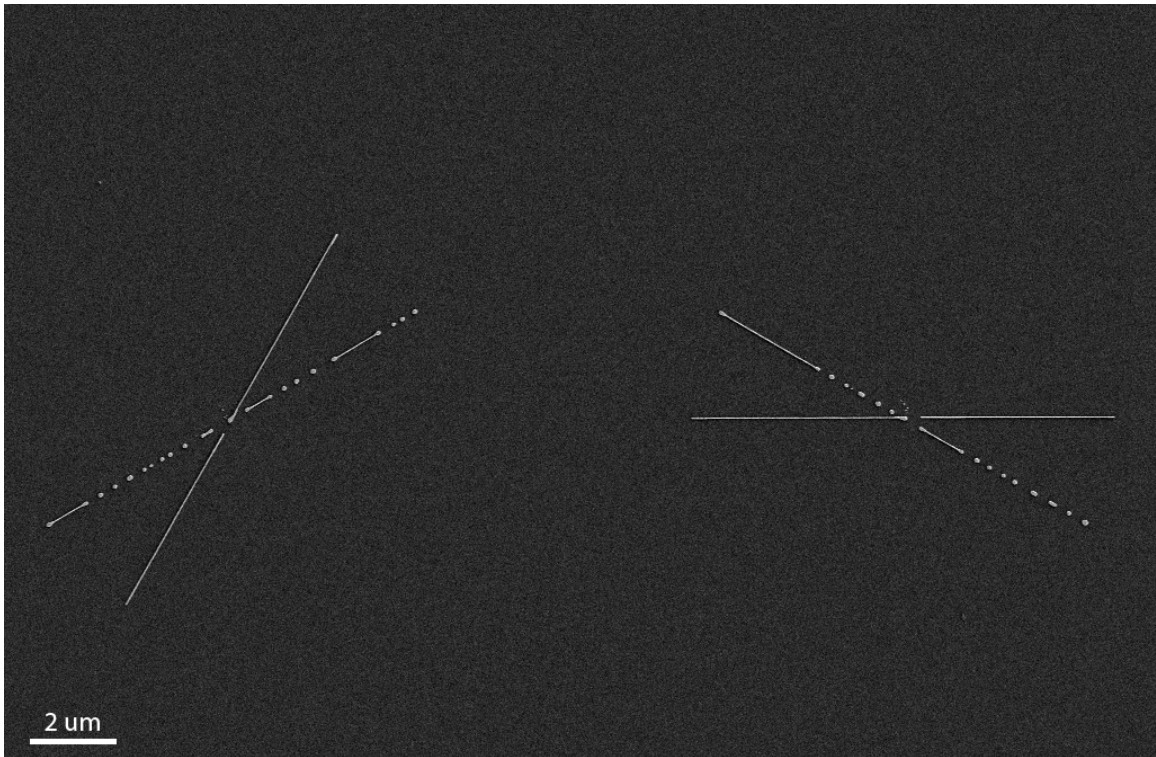
Figure C-13: Intersections of $\sim 70\,\text{nm}$–wide as–patterned lines. Both intersections contain one stable $< 11\bar{2}0 >$ and one unstable line.
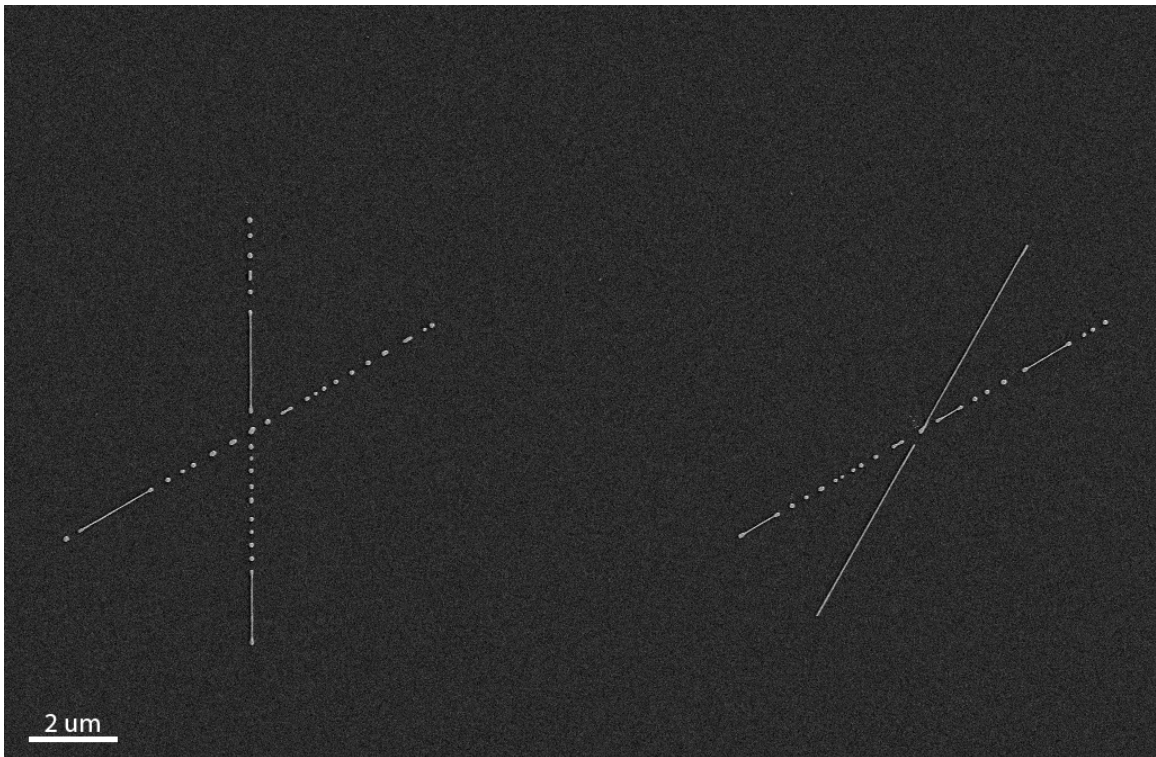
Figure C-14: Intersections of ∼70 nm–wide as–patterned lines. The left intersection contains two unstable lines, and the right intersection contains one unstable line (the line closer to horizontal) and one stable $< 11\bar{2}0 >$ line (the line closer to vertical).
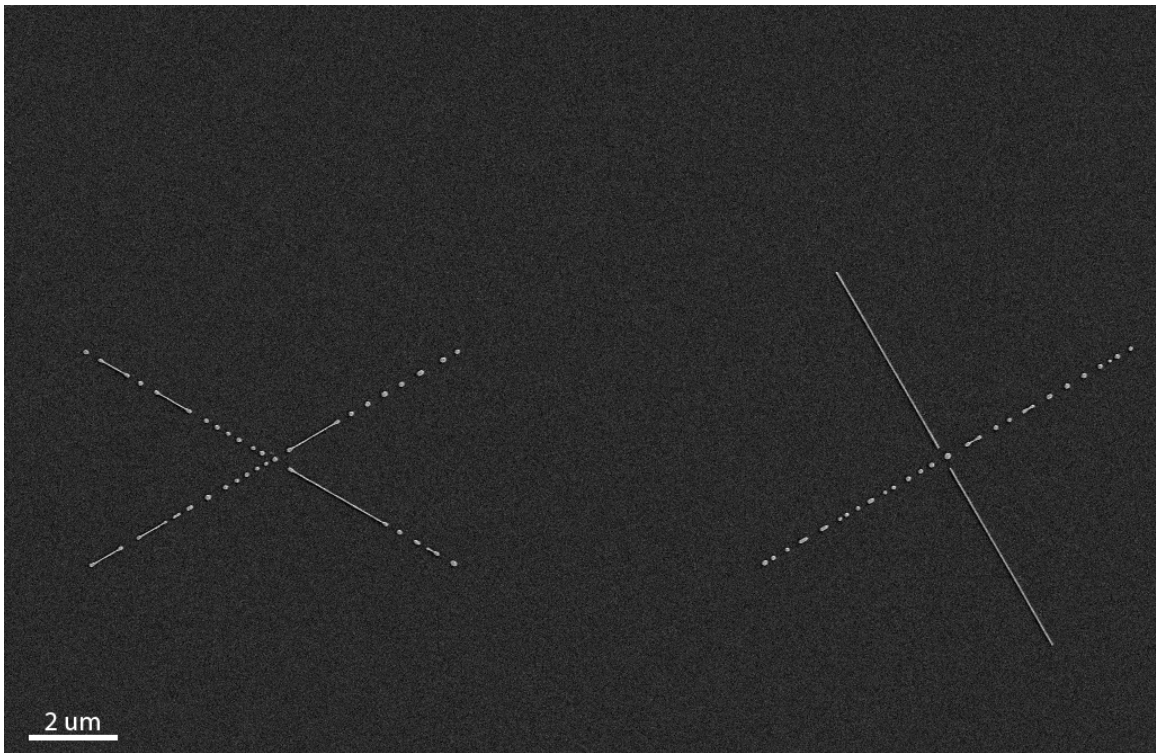
Figure C-15: Intersections of ~70 nm–wide as–patterned lines. The left intersection contains two unstable lines, and the right intersection contains one unstable line (the line running from lower left to upper right) and one stable $< 11\bar{2}0 >$ line (the line running from upper left to lower right).

Figure C-16: Intersections of ~70 nm–wide as–patterned lines. The left intersection is composed of two stable lines and has decomposed into 3 pieces: two lines and one sideways "V". The right intersection contains unstable line (the vertical line) and one stable $< 11\bar{2}0 >$ line.
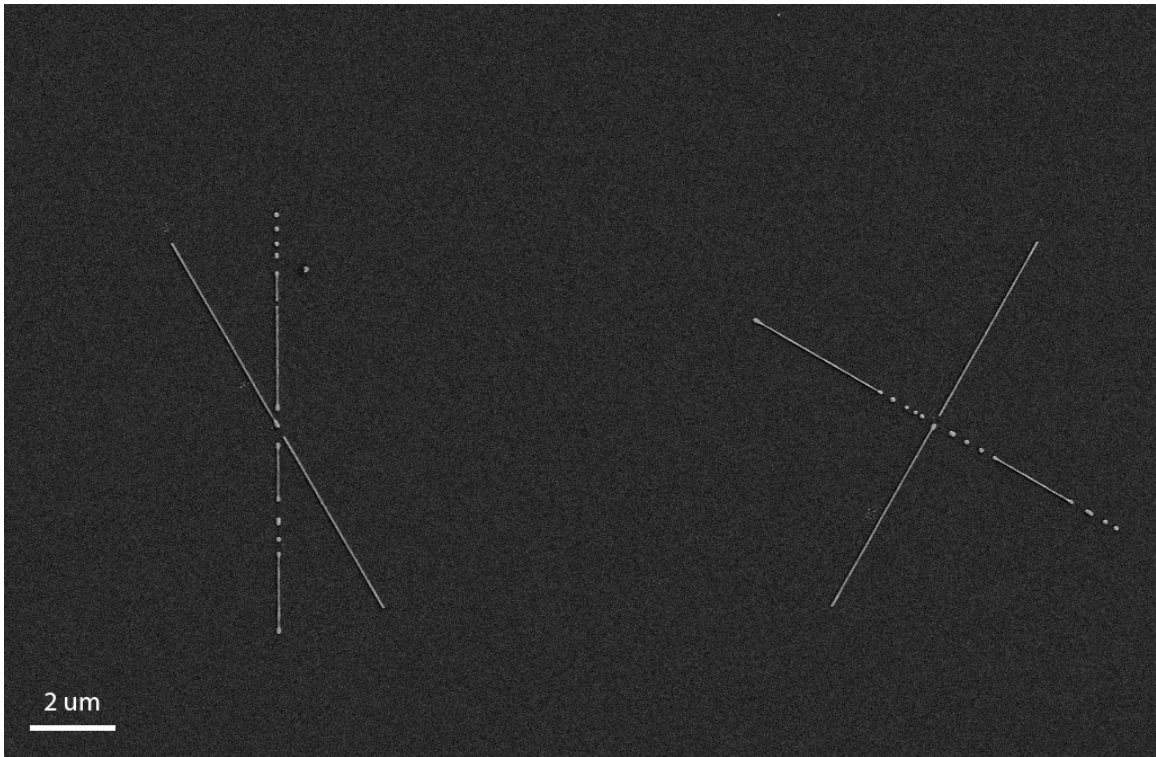
Figure C-17: Intersections of $\sim$70 nm–wide as–patterned lines. Both lines contain one stable $< 11\bar{2}0 >$ line and one unstable line.

Figure C-18: Intersections of ~ 70 nm–wide as–patterned lines. The left intersection contains one stable $< 11\bar{2}0 >$ line (oriented closer to vertical) and one unstable line. The right intersection is composed of two unstable lines.

C.1.3 Hexagonal Patches

Some samples were also patterned with hexagonal patches of different sizes and orientations. Those shown below were patterned from a 5 nm–thick film.

Figure C-19: A Ru patch which has been annealed for 45 minutes. The edges of the pattern are all 30° offset from stable $< 11\bar{2}0 >$ orientations. These edges have formed lines which are now in the process of breaking up.
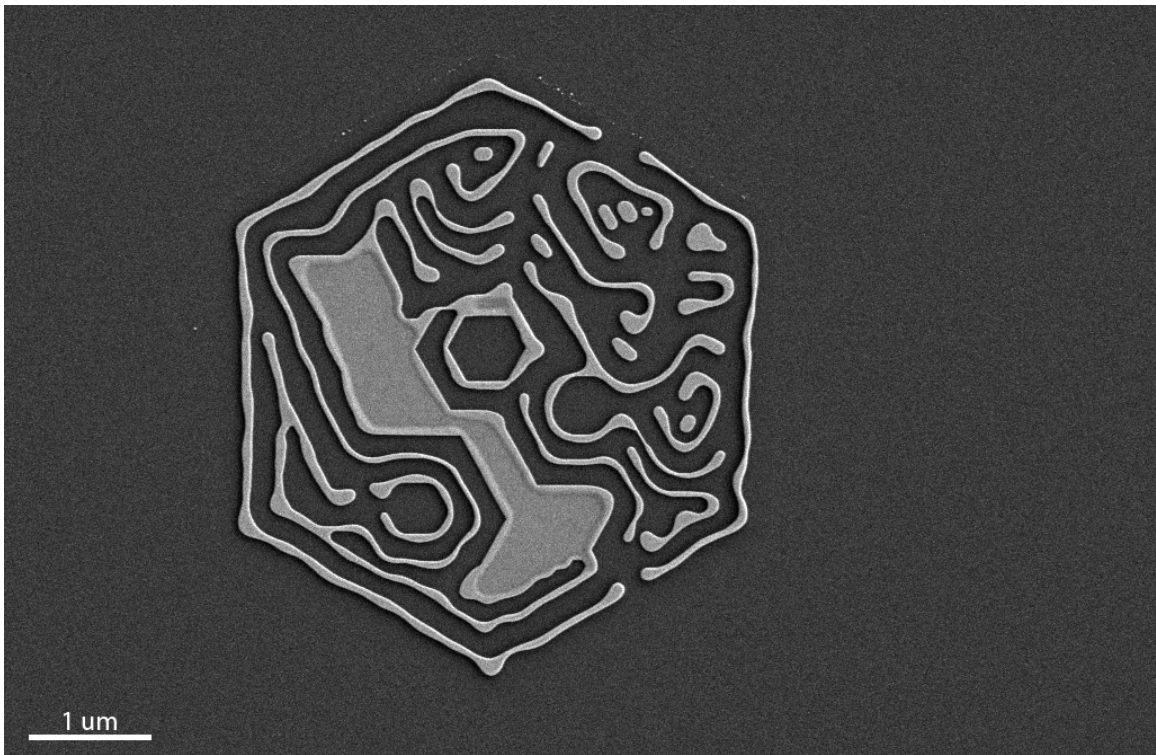
Figure C-20: A Ru patch, far smaller than that shown above, which has been annealed for 45 minutes. The edges of the pattern are all 30° offset from stable $< 11\bar{2}0 >$ orientations. These edges have formed lines which are now in the process of breaking up.
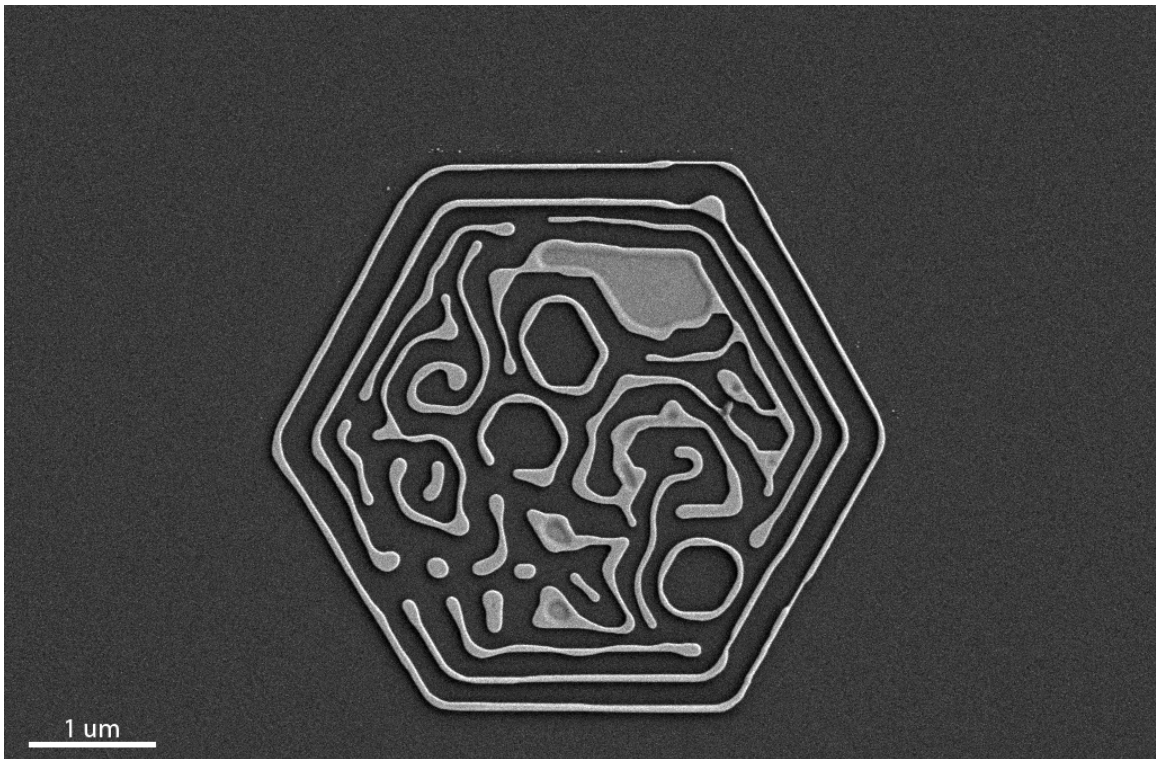
Figure C-21: A Ru patch which has been annealed for 45 minutes. The edges of the pattern are aligned along stable $< 11\bar{2}0 >$ orientations and thus appear more stable than those in figures C-19 and C-20. We believe channel dewetting is the likely mechanism by which the concentric hexagonal rings are formed.
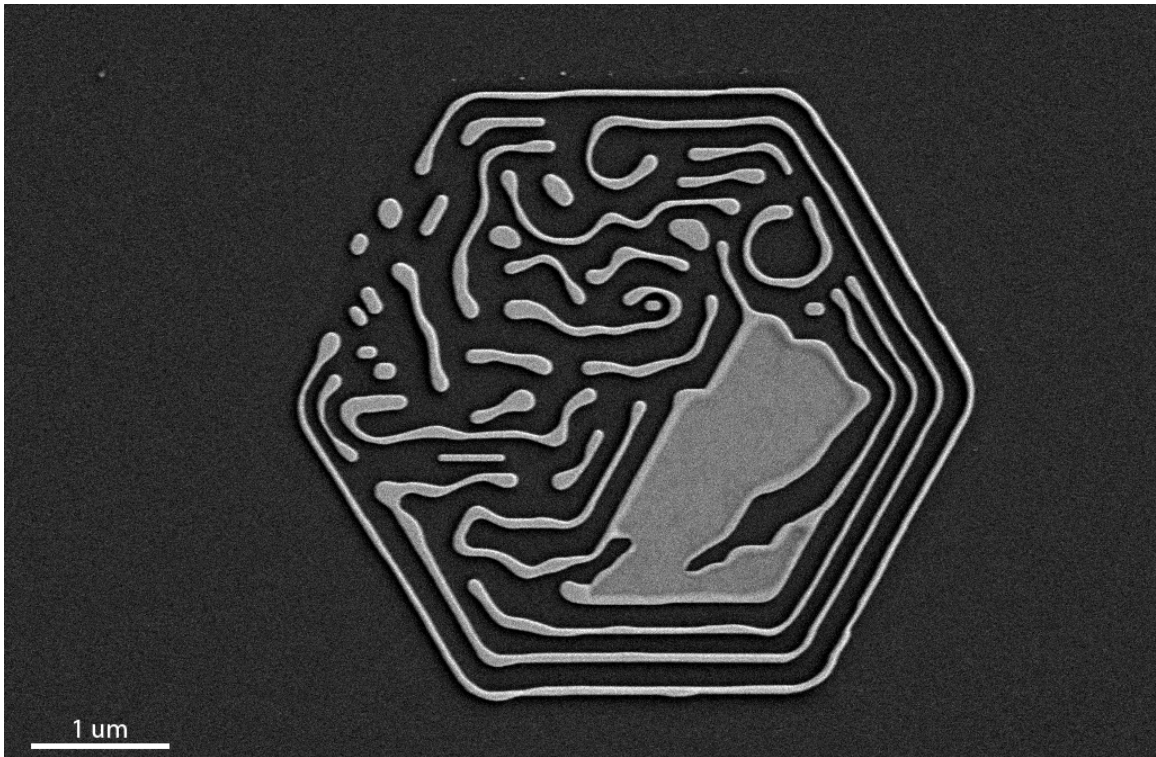
Figure C-22: A Ru patch which has been annealed for 45 minutes. The behavior seen in this image is similar to that in figure C-21.

Bibliography

(1) Jiran, E.; Thompson, C. V. *Thin Solid Films* **1992**, *208*, ISBN: 0040-6090, 23–28.

(2) Yu, R.; Mazumder, P.; Borrelli, N. F.; Carrilero, A.; Ghosh, D. S.; Maniyara, R. A.; Baker, D.; García De Abajo, F. J.; Pruneri, V. *ACS Photonics* **2016**, *3*, DOI: `10.1021/acsphotonics.6b00090`.

(3) Ye, J.; Thompson, C. V. *Advanced Materials* **2011**, *23*, ISBN: 1521-4095, 1567–1571.

(4) Ye, J.; Thompson, C. V. *Physical Review B - Condensed Matter and Materials Physics* **2010**, *82*, 1–4.

(5) Kim, G. H.; Thompson, C. V. *Acta Materialia* **2015**, *84*, Publisher: Pergamon, 190–201.

(6) Ye, J.; Thompson, C. V. *Acta Materialia* **2011**, *59*, Publisher: Acta Materialia Inc. ISBN: 1359-6454, 582–589.

(7) Zucker, R. V.; Kim, G. H.; Ye, J.; Carter, W. C.; Thompson, C. V. *Journal of Applied Physics* **2016**, *119*, Publisher: American Institute of Physics, 125306.

(8) Shin, Y. A.; Thompson, C. V. *Acta Materialia* **2021**, *207*, 116669.

(9) Balluffi, R. W.; Allen, S. M.; Carter, W. C., *Kinetics of Materials*, 2005; 672 pp.

(10) Herring, C. In *Fundamental Contributions to the Continuum Theory of Evolving Phase Interfaces in Solids: A Collection of Reprints of 14 Seminal Papers*, Ball, J. M., Kinderlehrer, D., Podio-Guidugli, P., Slemrod, M., Eds.; Springer Berlin Heidelberg: Berlin, Heidelberg, 1999, pp 33–69.

(11) Hoffman, D. W.; Cahn, J. W. *Surface Science* **1972**, *31*, 368–388.

(12) Taylor, J. E. *Acta Metallurgica Et Materialia* **1992**, *40*, 1475–1485.

(13) Mullins, W. W. *Journal of Applied Physics* **1957**, *28*, ISBN: 0001-6160, 333–339.

(14) Young, T. *Philosophical Transactions of the Royal Society of London* **1805**, *95*, Publisher: Royal Society, 65–87.

(15) Wulff, G. *Zeitschrift für Kristallographie - Crystalline Materials* **1901**, *34*, Publisher: De Gruyter Oldenbourg, 449–530.

(16) Winterbottom, W. *Acta Metallurgica* **1967**, *15*, Publisher: Pergamon, 303–310.

(17) Thompson, C. V. Materials Processing for Micro and Nano-Systems, Course Notes, Course Notes, Massachusetss Institute of Technology, 2018.

(18) Plummer, J. D.; Deal, M.; Griffin, P. B., *Silicon VLSI technology : fundamentals, practice and modeling*; Prentice Hall electronics and VLSI series; Prentice Hall: Upper Saddle River, NJ, 2000.

(19) Ohring, M., *Materials Science of Thin Films*, 2nd ed.; Elsevier Science: Burlington, 2001.

(20) Brandon, R.; Bradshaw, F. J. *the Mobility of the Surface Atoms of Copper and Silver Evaporated Deposits*; Royal aircraft establishment Farnborough (United Kingdom), 1966.

(21) Wong, H.; Voorhees, P. W.; Miksis, M. J.; Davis, S. H. *Acta Materialia* **2000**, *48*, 1719–1728.

(22) Srolovitz, D. J.; Safran, S. A. *Journal of Applied Physics* **1986**, *60*, ISBN: 0361-5235, 255–260.

(23) Dornel, E.; Barbé, J. C.; De Crécy, F.; Lacolle, G.; Eymery, J. *Physical Review B - Condensed Matter and Materials Physics* **2006**, *73*, 1–10.

(24) Zucker, R. V.; Carter, W. C.; Thompson, C. V. *Scripta Materialia* **2016**, *116*, 143–146.

(25) Hyun Kim, G.; Zucker, R. V.; Ye, J.; Craig Carter, W.; Thompson, C. V. *Journal of Applied Physics* **2013**, *113*, Publisher: American Institute of Physics, 043512.

(26) Zucker, R. V.; Kim, G. H.; Craig Carter, W.; Thompson, C. V. *Comptes Rendus Physique* **2013**, *14*, Publisher: Elsevier Masson, 564–577.

(27) Rayleigh, L. *Proceedings of the London Mathematical Society* **1878**, *s1-10*, Publisher: Oxford University Press (OUP), 4–13.

(28) Rayleigh, L. *Journal of Science* **1892**, *34*, 145–154.

(29) Plateau, M. T. *The London, Edinburgh, and Dublin Philosophical Magazine* **1856**, *12*, 286–297.

(30) Nichols, F. A.; Mullins, W. W. *Transactions of the Metallurgical Society of AIME* **1965**, *233*, 1840–1847.

(31) Nichols, F. A. *Journal of Materials Science* **1976**, *11*, 1077–1082.

(32) Santala, M. K.; Glaeser, A. M. *Surface Science* **2006**, *600*, 782–792.

(33) Balluffi, R. W.; Allen, S. M.; Carter, W. C. In *Kinetics of Materials*, 2005.

(34) Thompson, C. V. *Annual Review of Materials Research* **2012**, *42*, ISBN: 1531-7331 978-0-8243-1742-3, 399–434.

(35) Gadkari, P. R.; Warren, A. P.; Todi, R. M.; Petrova, R. V.; Coffey, K. R. *Journal of Vacuum Science & Technology A: Vacuum, Surfaces, and Films* **2005**, *23*, Publisher: American Vacuum Society, 1152–1161.

(36) Kim, G. H. Study of phenomenologies during templated solid-state dewetting of thin single crystal films, Accepted: 2016-06-22T17:19:26Z, Thesis, Massachusetts Institute of Technology, 2016.

(37) Garisto, F. *Thermodynamic Behaviour of Ruthenium at High Temperatures*; Whiteshell Nuclear Research Establishment, 1988.

(38) Williams, D. B.; Carter, C. B. In *Transmission Electron Microscopy*; Springer US: Boston, MA, 2009, pp 311–322.

(39) L'Etoile, M. A.; Thompson, C. V.; Carter, W. C. A level-set method for simulating dewetting in systems with strong crystalline anisotropy, In preparation, In preparation, 2022.

(40) Mullins, W. W. *Journal of Applied Physics* **1957**, *28*, Publisher: American Institute of Physics, 333–339.

(41) Smereka, P.; Li, X.; Russo, G.; Srolovitz, D. J. *Acta Materialia* **2005**, *53*, Publisher: Pergamon, 1191–1204.

(42) Ye, J.; Zuev, D.; Makarov, S. **2018**, DOI: 10.1080/09506608.2018.1543832.

(43) Leroy, F.; Borowik, Ł.; Cheynis, F.; Almadori, Y.; Curiotto, S.; Trautmann, M.; Barbé, J.; Müller, P. *Surface Science Reports* **2016**, *71*, Publisher: North-Holland, 391–409.

(44) Nichols, F. A.; Mullins, W. W. *Journal of Applied Physics* **1965**, *36*, Publisher: American Institute of Physics, 1826–1835.

(45) McCallum, M. S.; Voorhees, P. W.; Miksis, M. J.; Davis, S. H.; Wong, H. *Journal of Applied Physics* **1996**, *79*, Publisher: American Institute of Physics, 7604–7611.

(46) Carter, W. C.; Glaeser, A. M. *Acta Metallurgica* **1987**, *35*, 237–245.

(47) Leroy, F.; Cheynis, F.; Passanante, T.; Müller, P. *Physical Review B* **2012**, *85*, 195414.

(48) Jiang, W.; Bao, W.; Thompson, C. V.; Srolovitz, D. J. *Acta Materialia* **2012**, *60*, Publisher: Pergamon, 5578–5592.

(49) Roosen, A. R.; Taylor, J. E. *Journal of Computational Physics* **1994**, *114*, 113–128.

(50) Roosen, A. R.; Carter, W. C. *Physica A: Statistical Mechanics and its Applications* **1998**, *261*, 232–247.

(51) Bishop, C. M.; Satet, R. L.; Cannon, R. M.; Carter, W. C.; Roosen, A. R. *Zeitschrift für Metallkunde* **2005**, *96*, 124–134.

(52) Burger, M.; Haußer, F.; Stöcker, C.; Voigt, A. *Journal of Computational Physics* **2007**, *225*, Publisher: Academic Press Inc., 183–205.

(53) Jiang, W.; Zhao, Q.; Qian, T.; Srolovitz, D. J.; Bao, W. *Acta Materialia* **2019**, *163*, Publisher: Pergamon, 154–160.

(54) Jiang, W.; Zhao, Q.; Bao, W. *SIAM Journal on Applied Mathematics* **2020**, *80*, Publisher: Society for Industrial and Applied Mathematics, 1654–1677.

(55) Pierre-Louis, O.; Chame, A.; Saito, Y. **2007**, DOI: `10.1103/PhysRevLett.99.136101`.

(56) Pierre-Louis, O.; Chame, A.; Saito, Y. *Physical Review Letters* **2009**, *103*, Publisher: American Physical Society, 195501.

(57) Pierre-Louis, O.; Chame, A.; Dufay, M. *The European Physical Journal B* **2010**, *77*, 57–63.

(58) Cahn, J. W.; Carter, W. C. *Metallurgical and Materials Transactions A: Physical Metallurgy and Materials Science* **1996**, *27*, 1431–1440.

(59) Willmore, T. J., *Riemannian geometry*; Oxford University Press: 1993.

(60) Angenent, S.; Gurtin, M. E. *Archive for Rational Mechanics and Analysis* **1989**, *108*, 323–391.

(61) Li, B.; Lowengrub, J.; Rätz, A.; Voigt, A. *Commun. Comput. Phys* **2009**, *6*, 433–482.

(62) Hilliard, J. E.; Cahn, J. W. *Acta Metallurgica* **1958**, *6*, 772–774.

(63) Allen, S. M.; Cahn, J. W. *Acta Metallurgica* **1979**, *27*, 1085–1095.

(64) Almgren, F. In *Differential Geometry: Partial Differential Equations on Manifolds*, Greene, R. E., Yau, S.-T., Eds., Google-Books-ID: ulgECAAAQBAJ; American Mathematical Soc.: 1993.

(65) Osher, S.; Sethian, J. A. *Journal of Computational Physics* **1988**, *79*, 12–49.

(66) Zhao, H. K.; Chan, T.; Merriman, B.; Osher, S. *Journal of Computational Physics* **1996**, *127*, Publisher: Academic Press Inc., 179–195.

(67) Adalsteinsson, D.; Sethian, J. A. *Journal of Computational Physics* **1999**, *148*, 2–22.

(68) Sethian, J. A. *Proceedings of the National Academy of Sciences* **1996**, *93*, Publisher: National Academy of Sciences Section: Research Article, 1591–1595.

(69) scikit-fmm: the fast marching method for Python, original-date: 2012-02-06T00:24:57Z, 2021.

(70) Sussman, M.; Fatemi, E.; Sci, S. J. C. *An efficient, interface-preserving level set redistancing algorithm and its application to interfacial incompressible fluid flow*, Volume: 20 Issue: 4; 1999, pp 1165–1191.

(71) Smith, J.; Petrova, G.; Schaefer, S. In *Computers and Graphics (Pergamon)*; Issue: 5 ISSN: 00978493, Elsevier Ltd: 2012; Vol. 36, pp 360–365.

(72) Tran, R.; Xu, Z.; Radhakrishnan, B.; Winston, D.; Sun, W.; Persson, K. A.; Ong, S. P. *Scientific Data* **2016**, *3*, Number: 1 Publisher: Nature Publishing Group, 160080.

(73) Khenner, M.; Averbuch, A.; Israeli, M.; Nathan, M. *Journal of Computational Physics* **2001**, *170*, 764–784.

(74) Wong, H.; Voorhees, P. W.; Miksis, M. J.; Davis, S. H. *Acta Materialia* **2000**, *48*, 1719–1728.

(75) Ye, J.; Thompson, C. V. *Applied Physics Letters* **2010**, *97*, Publisher: American Institute of Physics, 071904.

(76) Ye, J.; Thompson, C. V. *Physical Review B* **2010**, *82*, Publisher: American Physical Society, 193408.

(77) Bonzel, H. P.; Preuss, E. *Surface Science* **1995**, *336*, 209–224.

(78) Jiang, W.; Wang, Y.; Zhao, Q.; Srolovitz, D. J.; Bao, W. *Scripta Materialia* **2016**, *115*, 123–127.

(79) Balluffi, R. W.; Allen, S. M.; Carter, W. C. In *Kinetics of Materials*, 2005.

(80) Bezanson, J.; Edelman, A.; Karpinski, S.; Shah, V. B. *SIAM review* **2017**, *59*, Publisher: SIAM, 65–98.

(81) Shin, Y. A. Templated solid-state dewetting of single crystal Ni thin films, Ph.D. Thesis, Massachusetts Institute of Technology, 2022.

(82) Zucker, R. V. Capillary-Driven Shape Evolution in Solid-State Micro- and Nano-Scale Systems, Ph.D. Thesis, Massachusetts Institute of Technology, 2015.

(83) L'Etoile, M. A.; Wang, B.; Cumston, Q.; Warren, A.; Barmak, K.; Coffey, K. R.; Carter, W. C.; Thompson, C. V. Experimental and computational study of the orientation dependence of single-crystal ruthenium banowire stability, In preparation, In preparation, 2022.

(84) Cahn, J. *Scripta Metallurgica* **1979**, *13*, Publisher: Pergamon, 1069–1071.

(85) Gurski, K. F.; McFadden, G. B. *Proceedings of the Royal Society of London. Series A: Mathematical, Physical and Engineering Sciences* **2003**, *459*, Publisher: Royal Society, 2575–2598.

(86) Ezzat, S. S.; Mani, P. D.; Khaniya, A.; Kaden, W.; Gall, D.; Barmak, K.; Coffey, K. R. *Journal of Vacuum Science & Technology A* **2019**, *37*, Publisher: American Vacuum Society, 031516.

(87) Milosevic, E.; Kerdsongpanya, S.; Zangiabadi, A.; Barmak, K.; Coffey, K. R.; Gall, D. *J. Appl. Phys* **2018**, *124*, 165105.

(88) Barmak, K. et al. *arXiv* **2020**, *38*, Publisher: arXiv, 033406.

(89) Bussmann, E.; Cheynis, F.; Leroy, F.; Müller, P.; Pierre-Louis, O. *New Journal of Physics* **2011**, *13*, 043017.

(90) Bollani, M. et al. *Nature Communications* **2019**, *10*, Publisher: Nature Research, 1–10.

(91) L'Etoile, M. A.; Thompson, C. V.; Carter, W. C. The role of anisotropy in dendritic dewetting and an analogy to solidification, Submitted, Submitted, 2022.

(92) Nuryadi, R.; Ishikawa, Y.; Tabe, M. *Applied Surface Science* **2000**, *159-160*, 121–126.

(93) Burhanudin, Z. A.; Nuryadi, R.; Ishikawa, Y.; Tabe, M.; Ono, Y. *Applied Physics Letters* **2005**, *87*, Publisher: American Institute of Physics, 121905.

(94) Sutter, P.; Ernst, W.; Choi, Y. S.; Sutter, E. *Applied Physics Letters* **2006**, *88*, Publisher: American Institute of Physics, 141924.

(95) Fan, Y.; Nuryadi, R.; Burhanudin, Z. A.; Tabe, M. *Japanese Journal of Applied Physics* **2008**, *47*, Publisher: IOP Publishing, 1461.

(96) Cheynis, F.; Bussmann, E.; Leroy, F.; Passanante, T.; Müller, P. *Physical Review B* **2011**, *84*, Publisher: American Physical Society, 245439.

(97) Rabkin, E.; Amram, D.; Alster, E. *Acta Materialia* **2014**, *74*, Publisher: Pergamon, 30–38.

(98) Chame, A.; Saito, Y.; Pierre-Louis, O. *Physical Review Materials* **2020**, *4*, Publisher: American Physical Society, 094006.

(99) Mullins, W. W.; Sekerka, R. F. *Journal of Applied Physics* **1963**, *34*, Publisher: American Institute of PhysicsAIP, 323–329.

(100) Mullins, W. W.; Sekerka, R. F. *Journal of Applied Physics* **1964**, *35*, Publisher: American Institute of PhysicsAIP, 444–451.

(101) Langer, J. S. *Science* **1989**, Publisher: American Association for the Advancement of Science, DOI: `10.1126/science.243.4895.1150`.

(102) Saffman, P. G.; Taylor, G. I. *Proceedings of the Royal Society of London. Series A. Mathematical and Physical Sciences* **1958**, *245*, Publisher: Royal Society, 312–329.

(103) Ivantsov, G. P. *Dokladi Akademii Nauk SSSR* **1947**, *58*, 857–569.

(104) Horvay, G.; Cahn, J. W. *Acta Metallurgica* **1961**, *9*, 695–705.

(105) Ben-Jacob, E.; Goldenfeld, N.; Langer, J. S.; Schön, G. *Physical Review A* **1984**, *29*, 330–340.

(106) Amar, M. B.; Pomeau, Y. *Europhysics Letters (EPL)* **1986**, *2*, Publisher: IOP Publishing, 307–314.

(107) Kessler, D. A.; Koplik, J.; Levine, H. *Physical Review A* **1986**, *33*, Publisher: American Physical Society, 3352–3357.

(108) Barbieri, A.; Hong, D. C.; Langer, J. S. *Physical Review A* **1987**, *35*, Publisher: American Physical Society, 1802–1808.

(109) Langer, J. S. *Reviews of Modern Physics* **1980**, *52*, Publisher: American Physical Society, 1–28.

(110) Osher, S.; Fedkiw, R. P., *Level set methods and dynamic implicit surfaces*; Springer: 2003; 273 pp.

(111) Sethian, J. A., *Level Set Methods and Fast Marching Methods: Evolving Interfaces in Computational Geometry, Fluid Mechanics, Computer Vision, and Materials Science*, Google-Books-ID: ErpOoynE4dIC; Cambridge University Press: 1999; 404 pp.

(112) Paterson, L. *Journal of Fluid Mechanics* **1981**, *113*, Publisher: Cambridge University Press, 513–529.

(113) Couder, Y.; Cardoso, O.; Dupuy, D.; Tavernier, P.; Thom, W. *Europhysics Letters (EPL)* **1986**, *2*, 437–443.

(114) Barbieri, A.; Langer, J. S. *Physical Review A* **1989**, *39*, 5314–5325.

(115) Taylor, J. E.; Cahn, J. W.; Handwerker, C. A. *Acta Metallurgica et Materialia* **1992**, *40*, 1443–1474.

(116) John, F. In *Partial Differential Equations*, John, F., Ed.; Applied Mathematical Sciences; Springer US: New York, NY, 1978, pp 1–30.

(117) Taylor, J. E. *Acta Metallurgica Et Materialia* **1992**, *40*, Publisher: Pergamon, 1475–1485.

(118) Greene, R. E.; Yau, S.-T., *Differential Geometry: Partial Differential Equations on Manifolds*, Google-Books-ID: ulgECAAAQBAJ; American Mathematical Soc.: 1993; 585 pp.

(119) Einstein, T. L. *arXiv:1501.02213 [cond-mat]* **2015**, 215–264.

(120) Milne, R. B. An adaptive level set method, Ph.D. Thesis, University of California, Berkeley, 1995, 95 pp.

(121) Barth, T. J.; Sethian, J. A. *Journal of Computational Physics* **1998**, *145*, 1–40.